Selective Oxidation of Ethylene to Ethylene Oxide on Silver Catalysts at Industrial Conditions: Reactor Profiles, Kinetics and Chlorine Inhibition

Vom Promotionsausschuss der
Technischen Universität Hamburg
zur Erlangung des akademischen Grades

Doktor-Ingenieur (Dr.-Ing.)

genehmigte Dissertation (Monografie)

von
Viktor Berg

aus
Alexandrowka, Russland

2025

1. Gutachter: Prof. Dr. rer. nat. Raimund Horn
2. Gutachter: Prof. Dr.-Ing. habil. Prof. e.h. Dr. h.c. Stefan Heinrich
3. Gutachterin: Prof. Dr.-Ing. Irina Smirnova
Tag der mündlichen Prüfung: 09. Dezember 2024

https://doi.org/10.15480/882.14136
https://orcid.org/0009-0002-7209-6438

Abstract

Selectivity is the key parameter in industrial ethylene oxide (EO) production by oxidation of ethylene with oxygen on $Ag/\alpha - Al_2O_3$ catalysts. Accurate temperature control in wall-cooled multitubular fixed-bed reactors and chlorination of the silver surface by feeding small chlorinated hydrocarbons such as 1,2-dichloroethane (DCE) are required to fine-tune electrophilicity and surface oxygen coverage for maximum EO selectivity at economic ethylene conversion.

In this work, a kinetic test setup was designed and built to measure initial reaction rates at differential conditions in an isotherm fixed-bed reactor which was located in a heated fluidized sand bath. Temperature and molar flow rate profiles of C_2H_4, O_2, CO_2, H_2O, DCE and the chlorine containing reaction products vinyl chloride (VC) and ethyl chloride (EC) were measured in a Compact Profile Reactor (CPR) and in a Pilot Scale Profile Reactor (PSPR) to explore the spatial interplay between DCE concentration, temperature, inlet flow rate, and O_2 conversion. Chlorine and oxygen compete for the same active silver sites despite four orders of magnitude different concentrations (ppm vs. vol-%). Chlorine coverage increases from inlet to outlet due to the decreasing partial pressure of O_2 along the bed leading to shut down of all reactions if all active Ag sites are blocked by chlorine.

A kinetic model was derived from a dual-site mechanism taken from literature. Kinetic parameters were determined from differential initial rate measurements, Arrhenius plots and by fitting the rate expressions implemented in a plug flow model to the species and temperature profiles in the CPR. Very good agreement was reached.

To validate the measured kinetics a Pilot Scale Profile Reactor (PSPR) with a static capillary sampling technique was desgnied and built. PSPR profiles were modeled by implementing the derived kinetic model into a 2D pseudohomogeneous reactor model. At conversions < 10 % the experimental profiles were well captured, but the model failed to accurately reproduce the point of thermal runaway in the catalyst bed of the PSPR being caused by a too low reactor temperature and resulting insufficient chlorine coverage of the silver surface.

Acknowledgements

I would like to take this opportunity to thank all those who have contributed to this work. First of all I would like to thank my advisor Prof. Dr. Raimund Horn for giving me the opportunity to do this research at the Institute of Chemical Reaction Engineering, thank you for your supervision, your guidance, your help in interpreting the profiles and the evenings and nights you spend on this work.

I would also like to thank Prof. Dr.-Ing. habil. Stefan Heinrich for examining my thesis and Prof. Dr.-Ing. Irina Smirnova for chairing the examination committee.

I would like to thank Dr. Frank Rosowski for funding and collaborating on this work and Dr. Michael Geske for his help in setting up and operating the pilot reactor at BasCat in Berlin.

Many thanks go to the BASF team, Dr. Michael B. Krämer, Dr. Marco Bosch and Dr. Andrey Karpov for their helpful input during the project.

Thanks to Dirk Manning and his team at the TUHH workshop, Petrick Bischoff and his team at the Fritz-Haber-Institute workshop and Georg Heyene and his team at the Fritz-Haber-Institute ELAB. Without all your work and support my vision would not become reality.

I would like to thank all the current and former members of the Institute of Chemical Reaction Engineering, Dr. Oliver Korup for his supervision and the helpful discussions, Klaus Mandel for the help with the electronics and control setup. Prof. Keil for the interesting discussions, Christina Laarmann for the support, Hermine Oppelaar and Eleni Poultourtzidou for the organizational support and Michael Schmidt for the help with the compact profile reactor.

I would also like to thank all the PhD students who went through this time with me together, Dr.-Ing. Ying Dong, Dr.-Ing. Stephan Bendt and Dr.-Ing. Bahne Sosna thank you for the proofreading and all their helpful hints, Dr.-Ing. Andrés Eduardo Aquino thanks for the help with the EDX measurements, Dr.-Ing. Jan Pottbacker, Dr.-Ing. Birte Wollak and Sebastian Sichert.

I thank my students for their support, Kai Jonas Heitmann, Eugenio Jose Gil Quessep, Adnan Abdullah, Sven Wasserberg and the former members of the institute, Adrian Koshors for his design of the fluidized sand bath, Dr. Ludwig Scharfenberg and Dr. Timur Kandemir.

Finally, and most importantly, I would like to thank my parents for always supporting me and believing in me. My family, my wife and my daughter, thank you for your unconditional support, for being my constant motivation and for your patience with me.

Contents

Abstract i

Acknowledgements ii

1 Introduction 1

2 Theoretical Background 4

2.1 Heterogeneous Catalysis 4

2.1.1 Heterogeneous Catalytic Reactions 6

2.1.2 Heat and Mass Transfer in Kinetic Measurements 7

2.1.3 Basic Concepts in Chemical Kinetics 13

2.2 Differentially Operated Fixed-Bed Reactor 15

2.3 Ethylene Epoxidation 17

2.3.1 Industrial Ethylene Epoxidation Process 17

2.3.2 Literature Review 19

2.4 Reactor Modeling 22

2.4.1 Axial and Radial Dispersion 23

2.4.2 1D Pseudohomogeneous Model 23

2.4.3 Parameter Regression from Profile Measurements 25

2.4.4 2D Pseudohomogeneous Model 25

3 Construction 28

3.1 Differential Reactor Design 28

3.2 Pilot Scale Profile Reactor Design 34

3.2.1 Piping and Instruments 34

3.2.2 Gas Supply and Evaporator 36

3.2.3 Reactor Unit 36

3.2.4 Combustion Unit 38

3.2.5 Process Control 39

4 Experimental 41

4.1 Catalyst 41

4.1.1 Catalyst Synthesis 41

4.1.2 Catalyst Activation 41

4.2 Kinetic Measurements 42

4.2.1 Differential Reactor . . . 42
4.2.2 Compact Profile Reactor . . . 43
4.2.3 Analytics . . . 45
4.3 Pilot Scale Profile Reactor . . . 46
4.3.1 Measurement Conditions . . . 46
4.3.2 Analytics . . . 47

5 Results and Discussion 49
5.1 Differential Reactor . . . 49
5.1.1 Heat and Mass Transfer Gradients . . . 49
5.1.2 Reaction Order . . . 51
5.1.3 Activation Energy . . . 54
5.1.4 Rate Law Derivation . . . 56
5.2 Compact Profile Reactor . . . 60
5.2.1 Heat and Mass Transfer Gradients . . . 60
5.2.2 CPR Profiles for Mechanistic Studies . . . 61
5.2.3 Interrupting DCE Feeding . . . 70
5.2.4 Spatially Resolved Kinetic Measurements . . . 76
5.3 Pilot Scale Profile Reactor Simulation . . . 81
5.3.1 Axial and Radial Dispersion . . . 81
5.3.2 2D Pseudohomogeneous Profile Simulation . . . 82

6 Summary and Conclusions 87

A Appendix 90
A.1 GC-Calibration . . . 90
A.2 Correlation Matrix for Fitted Kinetic Parameters . . . 94
A.3 Pilot Scale Profile Reactor Measurements . . . 98
A.3.1 Profile Measurements at T = **180** °C . . . 98
A.3.2 Profile Measurements at T = **190** °C . . . 103
A.3.3 Profile Measurements at T = **200** °C . . . 107

Bibliography 109

Nomenclature 119

List of Figures 123

List of Tables 127

1 Introduction

The majority of chemical reactions in industry take place in heterogeneously catalyzed reactors (fixed-bed reactors), in which a fluid, usually gas, flows through or over the catalytically active solid material, which is arranged in an immobile manner inside the reactor [1]. Due to its simple construction and the absence of any moving parts, the investment and maintenance costs are rather low. Therefore, a wide range of process conditions such as high pressure and temperature can be applied due to the robust construction usually made of steel. For highly exothermic or endothermic reactions, the temperature can be controlled by design modifications of the fixed-bed reactor [2]. The active catalyst can be loose particles, coated walls or structured packings [3, 4]. The main advantage is that the catalyst remains inside the reactor and the separation step of fluid and solid is omitted. On the other hand, complex reactions with several reaction steps, with produced and consumed intermediates as well as temperature and concentration gradients that take place inside the fixed-bed reactor are difficult to understand because of the complex behavior and the few possibilities to gain insight into the reaction. Typically, the "inlet-outlet" approach is used to measure inlet and outlet temperatures, conversions, and selectivities, which are used to draw conclusions about the reaction steps taking place inside the reactor [5]. In such cases, the reactor itself remains a black box. To overcome this obstacle, profile measurement techniques are used to monitor temperature and concentration profiles inside the catalytic fixed-bed reactor [6, 7]. Two different approaches are commonly used: profile reactor with sampling via a moving capillary and with static sampling points (e.g. side sampling ports). The sampling position from side ports sampling is therefore unfortunate because of bypass flow due to the high porosity at the wall. Moving capillaries, typically made of fused silica or stainless steel, have the advantage that the sampling position can be adjusted by a stepper motor during the measurement to achieve high spatial resolution of temperature and concentration in the axial direction, taking samples from the center of the catalyst bed. With such a setup, steep gradients and the formation and consumption of intermediates can be identified even under harsh reaction conditions such as the epoxidation reaction of ethylene to ethylene oxide (EO). The partial oxidation of ethylene to ethylene oxide has a long history and is a good example of the importance of heterogeneously catalyzed reactions in our daily lives. Ethylene oxide is a highly reactive molecule and is used in numerous reactions to produce ethoxylates, ethanolamines, polyesters and ethylene glycol, in which approximately 70 % of the total ethylene oxide produced is converted to [8]. The annual production of ethylene oxide was nearly 30.7 million metric tons in 2021 [9]. The ethylene epoxidation reaction takes place at $10 - 20$ bara and a temperature range of $220 - 275$ °C by partial oxidation of ethylene with oxygen over a supported low surface $Ag/\alpha - Al_2O_3$ catalyst [10]. EO is the desired product, while CO_2 and H_2O are formed by the unselective parallel reaction [11]. The subsequent oxidation of EO leads to further formation of CO_2 and H_2O. Selectivity is the key parameter for the industrial epoxidation reaction because the cost of ethylene determines the cost of production. An unpromoted

catalyst achieves selectivities of 50 %, by cofeeding chlorinated hydrocarbons such as 1,2-dichloroethane (DCE), vinyl chloride (VC) or ethyl chloride (EC) a selectivity increase up to 70 % to 80 % is achieved [12]. Nowadays, industrially applied catalysts are highly promoted with Cs, Re, Li, Mo reaching selectivities toward EO of 90 % [13]. The study of the ethylene epoxidation reaction is challenging due to the highly exothermic unselective parallel and consecutive oxidation reaction, which makes heat removal critical. To avoid thermal runaway, industrial EO production takes place in multitubular fixed-bed reactors, in which many small-diameter reactors are used to control the reaction temperature by removing excess heat [10]. In addition, EO is toxic and carcinogenic and tends to polymerize or decompose detonatively, making this reaction very dangerous [14]. To better understand the epoxidation reaction, especially the moderation by halogenated hydrocarbons, information from inside the reactor is needed.

The aim of this work is to investigate the epoxidation reaction under industrially relevant temperature and pressure conditions using the profile reactor technique based on the development of Horn et al. [15]. Therefore, intrinsic kinetic parameters, reaction orders and activation energies were determined by in-house measurements using a differentially operated fixed-bed reactor heated by a fluidized sand bath to maintain isothermal conditions [16]. The kinetic test reactor was designed, built, and operated to determine kinetic parameters at O_2 conversion below 5 % to maintain differential operation. Initial reaction rates were determined from measured product formation rates [5].

A Compact Profile Reactor (CPR) developed by Reacnostics GmbH, based on the patent of Horn and Korup [17], was used to measure concentration and temperature profiles in a compact manner, minimizing radial temperature and concentration gradients. The CPR uses the moving capillary technique by moving the entire reactor and keeping the capillary in position. The sample is taken through a laser drilled orifice in the capillary. The sample volume can be adjusted either by a micrometer valve for higher reaction pressure or by a vacuum pump for lower reaction pressure. Using the CPR, the influence of DCE on the reactor performance could be tested by measuring concentration profiles in the subppm range inside the catalyst bed. The radial gradient-free profiles were therefore suitable for kinetic parameter regression for O_2 conversion above 5 %, using a 1D pseudohomogeneous model to fit the kinetic parameters to the profiles at different reaction conditions. The catalyst used was an unpromoted supported low surface $Ag/\alpha - Al_2O_3$ catalyst provided by BASF SE. The catalyst used in the differentially operated fixed-bed reactor and CPR was a crushed, split shape catalyst with a sieve fraction of $200 - 400$ µm and a silver loading of 14.5 wt-%.

In addition, a modified Pilot Scale Profile Reactor was designed and built to sample through 10 static capillaries with 400 µm diameter located in the center of the catalyst bed. The capillaries are placed equidistantly in the center of the catalyst to provide a representative sample of the reaction mixture rather than measuring at the wall with side sampling ports. Temperature is measured by 16 thermocouples distributed equidistantly in the axial direction of the reactor, surrounded by a steel liner that holds the thermocouples in position. Safety instrumentation and process control have been implemented for 24/7 unattended operation with automatic sampling by selecting each position with a switching valve and gas composition analysis by two gas chromatographs (GC) used in series to accelerate the profile measurement. With this setup, the partial oxidation reaction was measured at near industrial process conditions with a gas hourly space velocity (GHSV) of 4750 h^{-1} at 17 bara and a temperature range of $180 - 200$ °C. With cofeeding of DCE up to 3 ppm for a catalyst bed length of

up to 0.5 m and a catalyst sieve fraction of $500 - 900$ µm. The profiles measured in the Pilot Scale Profile Reactor (PSPR) were used to validate the kinetic parameters by simulating the profiles using a 2D pseudohomogeneous model with the kinetic rate expression derived from differentially operated fixed-bed reactor and profile regression from CPR measurements using a literature dual site mechanism [18].

Theoretical Background 2

This chapter gives a general introduction to heterogeneous catalysis. The Chapter 2.1 explains how a catalyst affects a chemical reaction and gives examples of catalysts used in the chemical industry. The chemical and physical background that takes place during a heterogeneously catalyzed reaction is discussed, such as mass and heat transfer, and a general concept of kinetics is given. Chapter 2.2 presents the theory of kinetic measurements in differentially operated fixed-bed reactors. Chapter 2.3 provides a brief literature review of the ethylene epoxidation reaction. Lastly, reactor modeling is discussed in Chapter 2.4.

2.1 Heterogeneous Catalysis

The term catalysis was introduced by Berzelius in 1836 [19]. He concluded that a new force, *the catalytic force*, is active in addition to affinity. An appropriate definition in modern terms is:

"A catalyst is a substance that affects the rate or direction of a chemical reaction, but is not significantly consumed in the process." [20]. There are three important aspects to this definition. First, a catalyst can increase or decrease the rate of a reaction. Second, the catalyst can affect the selectivity of a reaction or its direction. Third, the amount of catalyst consumed is negligible compared to the amount of reactants consumed. A catalyst cannot change the equilibrium point set by thermodynamics, but it can accelerate the rate at which the point is approached. Figure 2.1 schematically

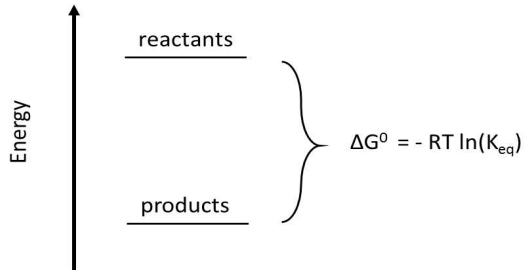

Figure 2.1: Thermodynamic equilibrium.

shows the energy levels of the reactants and the products. The products are at a lower Gibbs free energy, which means that the reaction is favored and can occur spontaneously. The change in Gibbs free energy is related to the equilibrium constant (K_{eq}) of a reaction by [21]:

$$\Delta G^0 = -RT \cdot \ln(K_{eq}) \tag{2.1}$$

K_{eq} represents the equilibrium composition of a reaction by the product of the activity coefficients (a_i) to the power of its corresponding stoichiometric coefficient (ν_i) involved

in the chemical reaction (eq. 2.2).

$$K_{eq} = \prod_i a_i^{\nu_i} \tag{2.2}$$

But if the reactants are not in their thermodynamically favored state, why do they not spontaneously react to form the products? This question can be answered with Figure 2.2, which shows the energy and the reaction coordinate. To convert the reactants to the products, the activation energy (Ea) must be provided to overcome the energy barrier separating the reactants from the products. If the reaction is thermodynamically favorable but kinetically unfavorable, the reaction is either too slow or does not occur simply because of the high energy barrier.

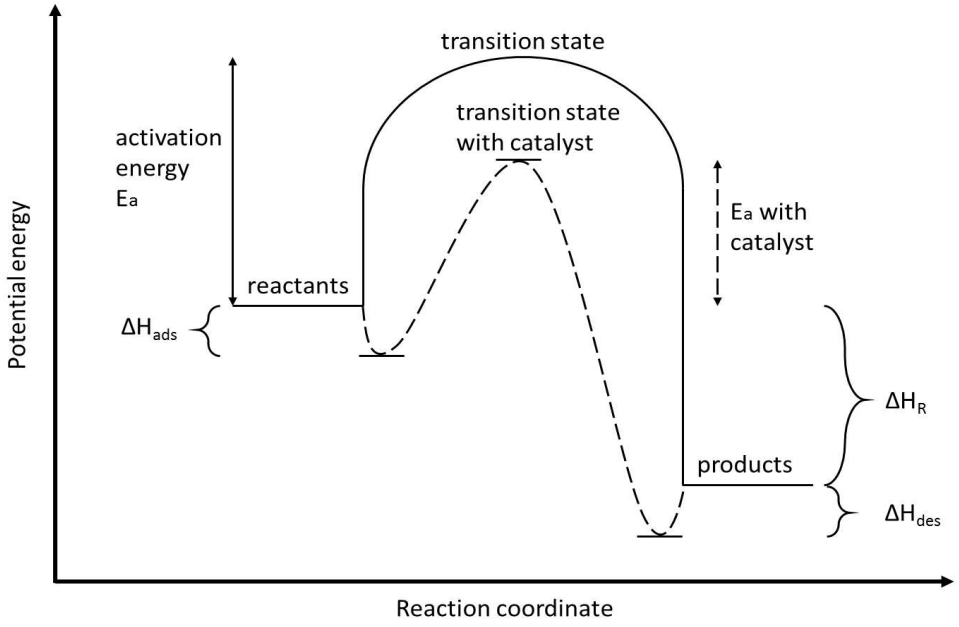

Figure 2.2: Reaction path diagram.

A catalyst lowers this energy barrier by providing a different reaction coordinate at which the required activation energy is lower without affecting the reaction equilibrium [5]. In a heterogeneously catalyzed reaction, the reactants (at least one) must adsorb onto the catalyst surface, releasing heat of adsorption (ΔH_{ads}). Less energy is required to reach the transition state compared to an uncatalyzed reaction. The products formed must desorb from the catalyst, which requires energy (ΔH_{des}). In case of an exothermic reaction heat is released (negative ΔH_R), in case of an endothermic reaction heat is consumed (positive ΔH_R). Catalytic reactions are often divided into homogeneous and heterogeneous reactions. A homogeneously catalyzed reaction occurs when both the catalyst and the reactants are in the same liquid phase. A heterogeneously catalyzed reaction is generally limited to a solid catalyst and reactants in the gas or liquid phase. The majority of industrial catalytic processes involve gaseous reactants and a solid catalyst [20]. The catalysts can be further classified as bulk, coated or supported catalysts and consist of either organic materials such as enzymes (e.g. alcohol dehydrogenase) and ion exchange resins (e.g. carboxylic acid) or inorganic materials such as metals (e.g. Ag), oxides (e.g. TiO_2) or sulfides (e.g. NiMoS) [22]. Bulk catalysts consist only of the catalytic active material, such as platinum gauze for ammonia oxidation and alumina for alkene isomerization [22, 23]. Coated

catalysts are a catalytically active layer applied to an inert structured surface. The most popular application of coated catalysts is the monolithic honeycomb for emission control in automotive applications [24]. Other applications include structured packings, foams, and sponges [4, 25]. Supported catalysts consist of a small catalytically active phase deposited on a support surface [26, 27]. The support provides mechanical stability and a porous structure with increased surface area for catalyst dispersion and can be fabricated in a wide range of shapes, sizes, porosities and surface areas [22]. The catalyst support is not inert in all cases, in some applications catalytic activity is desired, e.g., bifunctional catalysts such as zeolites and alumina [27, 28]. During the lifetime of a catalyst, the performance decreases because the catalyst deactivates. One reason for deactivation is sintering of the dispersed active phase by prolonged exposure to high reaction temperatures, which reduces the surface area available for the reaction. Another reason is coking, which occurs especially in reactions involving hydrocarbons, e.g., dry reforming of methane to synthesis gas [29]. Coking blocks the active sites making them unavailable for further reactions [30]. Another reason for deactivation of catalysts is irreversible chemisorption on an active site, which is called poisoning [31]. Used feed in chemical reactions is always accompanied by impurities such as sulfur, which can lead to poisoning. Selective poisoning applied in multiple reaction systems with parallel and consecutive reactions can lead to improved catalyst performance, increasing activity and selectivity of a catalyst, such poisons are called promoters [32]. Promoters are also used to extend the lifetime of the catalyst by preventing e.g., agglomeration of the active dispersed phase of a catalyst as applied to alumina promoted iron in ammonia synthesis [33]. Additives can act as structural promoters, e.g. cesium in ethylene epoxidation that blocks sites where the strongest (unselective) Ag−O bonds are formed [34]. Promoters can influence the electronic structure as well e.g. cofeeding chlorine in the ethylene epoxidation enhances the electron deficiency of silver making it more selective to ethylene oxide [35]. Most catalytic surfaces are polycrystalline, with each surface having terraces, vacancies, edges, and corners. In addition, solid catalysts have defects of atomic or electronic nature and unknown impurities in the bulk and on the surface. As the catalytic reaction progresses, the atomic structure and composition may change [36]. As mentioned above, the reaction takes place on an active site according to the concept introduced by Taylor in 1925 [37]. Taylor's idea was that there are surfaces with few atoms that are catalytically active (structure sensitive) and surfaces with many atoms that are catalytically active (structure insensitive). Next, Taylor said: *" The amount of catalytically active surface is determined by the reaction catalyzed"*, meaning that the catalyst and the catalyzed reaction adapt to each other. This adaptive behavior can be explained by surface reconstruction. The importance of surface structure, defects and impurities underlines the difficulty of identifying the active site for a catalyzed reaction, although much progress has been made in identifying and quantifying active sites, e.g. with selective chemisorption methods [36, 38].

2.1.1 Heterogeneous Catalytic Reactions

A heterogeneous catalytic reaction takes place following a proper sequence of physical and chemical processes illustrated in Figure 2.3 [39].

1. Mass transfer of reactants from the bulk fluid to the external surface of the catalyst particle.
2. Diffusion of reactants from the particles surface to the internal pore structure.
3. Chemisorption of at least one of the reactants on the active site.

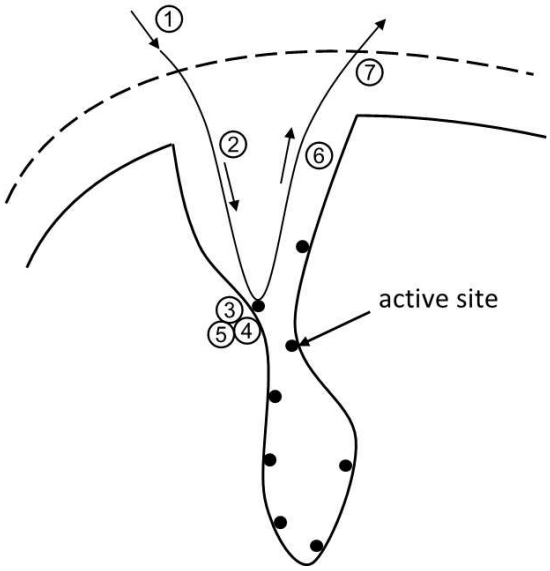

Figure 2.3: Heterogeneous catalyzed reaction and mass transport.

4. Reaction on the active site.
5. Desorption of the adsorbed species from the active site.
6. Diffusion of the products from the catalyst pore to the external surface of the catalyst.
7. Mass transfer of the products from the external surface of the catalyst to the bulk fluid.

If the catalyst is nonporous, steps 2 and 6 are absent. Steps 3 and 5 are basically chemical, while steps 1, 2, 6 and 7 are physical. Steps 1 and 7 are highly dependent on the fluid flow characteristics. If the catalytic reaction is very fast and the mass transfer is slow, the observed rate will depend on the mass transfer. Measures that increase mass transfer will result in an increased observed rate. To overcome the limitations of mass and heat-transfer, several analytical and experimental methods can be used, which are discussed in the following chapter.

2.1.2 Heat and Mass Transfer in Kinetic Measurements

The steps shown in Chapter 2.1.1 make it challenging for an engineer to design a reactor from measured kinetics. The mass and heat transfer processes required to transport reactants to the active site and to provide heat for the reaction can limit the observed rate. To measure intrinsic kinetics, the heat and mass transfer limitations must be small enough to be negligible. According to Mouljin and Kapteijn [40], temperature limitations (T-grad) are more likely to occur than mass transport limitations (c-grad), which can be ranked according to their influence as follows:

$$\text{T-grad}_{bed} > \text{T-grad}_{ext} > \text{c-grad}_{int} > \text{T-grad}_{int} > \text{c-grad}_{ext} \qquad (2.3)$$

Temperature limitations within the catalyst bed have the greatest influence, followed by external temperature and internal mass transfer limitations. Internal temperature and external mass transfer limitations have the least influence. Therefore, avoiding any temperature gradient within the catalyst bed is the first priority for experimental

kinetic measurements. Additionally to the experimental procedure for limitation testing, an analytic approach based on empirical correlations show whether internal or external limitations are present at measurement conditions.

Extraparticle Gradients

At steady state, the rate of energy released (or consumed) by the reaction must be equal to the rate at which heat is transferred to the fluid. The same is true for mass transfer, where the rate of mass supply to the outer surface of the catalyst must be equal to the rate at which it is consumed or transported to the inner pore structure. The heat and mass transfer is analyzed by the so-called film transport model, which defines the heat and mass transfer flux from the bulk fluid to the particle in terms of transfer coefficients for mass (k_f) and heat (h).

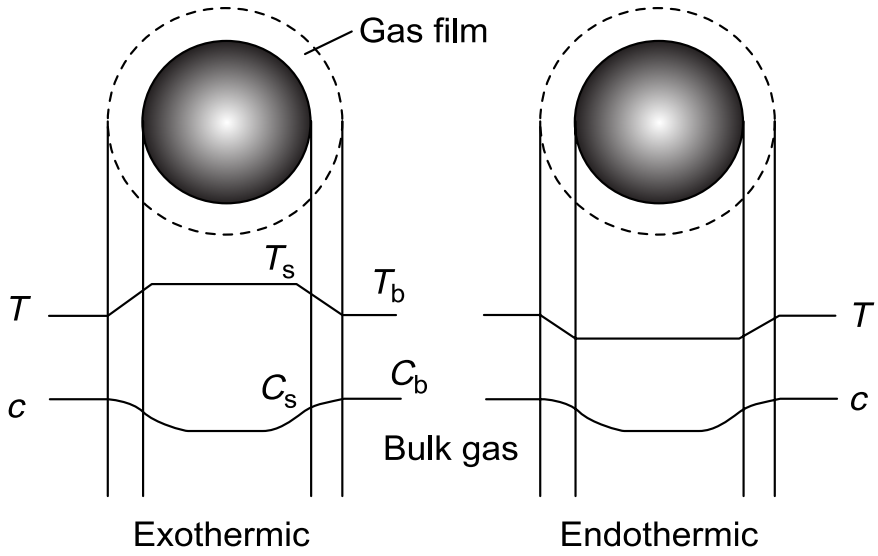

Figure 2.4: Schematic illustration of the film layer around the particle with their corresponding temperature and concentration gradients for an exothermic and endothermic reaction, taken from [40].

The mass transfer rate is proportional to the concentration difference across the film, as can be seen by performing a mass balance across the film:

$$V_p \cdot r_{v,obs} = A_p \cdot k_f \cdot (c_b - c_s) \qquad [mol/s] \tag{2.4}$$

with the volume of the particle (V_p) and the area of the particle (A_p). The measured or observed reaction rate can be expressed as:

$$r_{v,obs} = \frac{A_p}{V_p} \cdot k_f \cdot (c_b - c_s) \qquad [mol/(m^3 \cdot s)] \tag{2.5}$$

When the surface concentration is equal to the bulk concentration, there are no mass transfer limitations. In order to relate the surface concentration to observable variables, the dimensionless Carberry number was introduced [41]. The Carberry number represents the ratio of the observed reaction rate to the maximum possible mass transfer rate, i.e. when the surface concentration is zero, which corresponds to the best possible catalyst [40].

$$Ca = \frac{\frac{A_p}{V_p} \cdot k_f \cdot (c_b - c_s)}{\frac{A_p}{V_p} \cdot k_f \cdot c_b} = \frac{c_b - c_s}{c_b} \tag{2.6}$$

For the absence of external mass transfer limitation a criterion derived from the effectiveness factor, which relates the measured reaction rate to the rate at bulk concentration and temperature conditions, can be applied:

$$\eta_e = \frac{r_{v,obs}(c_s, T_s)}{r_{v,bulk}(c_b, T_b)} = (1 - Ca)^{\alpha} = 1 \pm 0.05 \tag{2.7}$$

Taking into account the order of the overall reaction (α), the deviation from unity should not exceed 5 %. The evaluation of the external heat transfer can be treated analog to the mass transfer limitation. The heat balance over the film results in:

$$r_{v,obs} \cdot (-\Delta H_R) = -\frac{A_p}{V_p} \cdot h \cdot (T_b - T_s) \qquad [W/m^3] \tag{2.8}$$

Combining Equations 2.5 and 2.8 yields:

$$\beta_e \cdot Ca = \frac{k_f \cdot c_b \cdot (-\Delta H_R)}{h \cdot T_b} \cdot \frac{c_b - c_s}{c_b} = \frac{T_s - T_b}{T_b} \tag{2.9}$$

The external Prater number (β_e) represents the ratio between the maximum heat production on the catalyst surface resulting from the chemical reaction and the heat transfer rate from the particle to the fluid, i.e. β_e determines the maximum temperature increase (or decrease in the case of endothermic reactions). Assuming the effectiveness factor is particularly influenced by heat effects for small Ca values, it is dominated by the rate constant ratio:

$$\eta_e \approx \frac{k(T_s)}{k(T_b)} = exp\left[-\frac{Ea}{R \cdot T_b}\left(\frac{T_b}{T_s} - 1\right)\right] = 1 \pm 0.05 \tag{2.10}$$

A series expansion of the exponential function and combination of eq. 2.9 leads to:

$$|\gamma_b \cdot \beta_e \cdot Ca| = \left|\left(\frac{Ea}{RT_b}\right)\left[\frac{(-\Delta H_R)k_f c_b}{hT_b}\right]\left(\frac{r_{v,obs}}{k_f a' c_b}\right)\right| < 0.05 \tag{2.11}$$

Where a' is the ratio of the particle surface area to the particle volume in m^{-1} and the dimensionless activation energy or Arrhenius number (γ_b) is the ratio of the apparent activation energy Ea to the universal gas constant R and the bulk temperature T_b, which gives the sensitivity of the reaction to temperature change.

Mass transfer coefficients can be determined by evaluating the dimensionless Sherwood (eq. 2.12) and Schmidt number (eq. 2.13). For heat transfer coefficients, the Nusselt number (eq. 2.14) and the Prandtl number (eq. 2.15) must be determined for the valid range defined by the Reynolds number (eq. 2.16).

$$Sh = \frac{k_f \cdot L}{D_{1f}} \tag{2.12}$$

$$Sc = \frac{\eta_f}{\rho_f \cdot D_{1f}} \tag{2.13}$$

$$Nu = \frac{h \cdot L}{\lambda_f} \tag{2.14}$$

$$Pr = \frac{\eta_f \cdot c_{p,f}}{\lambda_f} \tag{2.15}$$

$$Re_p = \frac{\rho_f \cdot u_0 \cdot d_p}{\eta_f} \tag{2.16}$$

With L as the characteristic length, the dynamic fluid viscosity η_f, the fluid density ρ_f, the fluid heat conductivity λ_f, the fluid heat capacity $c_{p,f}$, the superficial velocity

Table 2.1: Appropriate Dimensionless Numbers for Gases in Laboratory Reactors. Adapted from [40].

Mass transfer	Heat transfer	Range of validity
$Sh = \frac{0.357}{\varepsilon_{bed}} Re_p^{0.641} Sc^{\frac{1}{3}}$	$Nu = \frac{0.428}{\varepsilon_{bed}} Re_p^{0.641} Pr^{\frac{1}{3}}$	$3 < Re_p < 2000$
$Sh \approx 0.07 Re_p$	$Nu \approx 0.07 Re_p$	$0.1 < Re_p < 10$

u_0, and the molecular diffusion of the species of interest in the fluid D_{1f}. Correlations for the dimensionless numbers in packed-bed reactor applications are given in Table 2.1 [42–45].

In laboratory studies, external gradients in mass and temperature can be made negligible by using a diluted reactant stream to reduce the reaction rate, thereby reducing the energy evolved per unit volume. Next, high mass velocities are used to minimize heat and mass transfer resistances. The thickness of the boundary layer around the catalyst particle is highly dependent on the hydrodynamics present in the chemical reactor. By increasing the velocity around the catalyst particle, thus increasing the Reynolds number, the boundary layer thickness is reduced. An experimental test shows what Reynolds number is required to overcome the outer film transport limitation. This is done by increasing the flow rate while keeping the GHSV constant. If the conversion remains constant with increasing flow rate, the external film transport limitation can be neglected. Figure 2.5 (a) schematically shows the experimental external limitation test.

Intraparticle Gradients

Internal concentration gradients are often caused by diffusion limitations through the catalyst pores. Reactants diffuse through the pores and react, creating a concentration gradient across the particle diameter. Macropores offer the advantage of reduced diffusion resistance. On the other hand, macropores provide less surface area and thus fewer active sites available for the catalytic reaction than micropores. A bimodal pore distribution combines the advantages of micro and macro pores as shown in [46]. If the catalyst has macropores, molecular diffusion occurs, in which molecule-molecule collisions dominate. The molecular diffusion of an ideal gas is described by the binary diffusion coefficient D_{ij} and can be calculated e.g. according to the Chapman-Enskog theory [47]:

$$D_{ij} = \frac{1.8583 \cdot 10^{-3} \cdot T^{3/2} \cdot \sqrt{\frac{1}{M_i} + \frac{1}{M_j}}}{P \cdot \sigma_{ij}^2 \cdot \Omega} \qquad [cm^2/s] \tag{2.17}$$

where M is the molar mass in g$\cdot$ mol^{-1}, P is the total pressure in atm, σ is the mean collision diameter in Å which can be calculated from the Equation 2.18 with tabulated values for the pure components [48, 49] and the collision integral Ω (eq. 2.19) [48, 50, 51].

$$\sigma_{ij} = \frac{1}{2} \cdot (\sigma_i + \sigma_j) \tag{2.18}$$

$$\Omega = [A(T^*)^{-B}] + C \cdot [exp(-D \cdot T^*)] + E \cdot [exp(-F \cdot T^*)] \tag{2.19}$$

$$T^* = \frac{k_B \cdot T}{\epsilon} \tag{2.20}$$

With T^* as the dimensionless temperature related to the characteristic energy ϵ calculated according to the Equation 2.20, where k_B is Boltzmann's constant. Constants

for the calculation of the collision integral can be found in [52]. If only micropores are present ($d_{pore} \leq 2$ nm), i.e. if the mean free path between collisions is larger than the pore diameter, the diffusion is reduced to the so-called Knudsen diffusion, in which molecule-wall collisions dominate [53]. The Knudsen diffusion coefficient is directly proportional to the pore radius $\bar{r}$ and can be calculated with [54]:

$$D_{iK} = 9.7 \cdot 10^3 \cdot \bar{r} \cdot \sqrt{\frac{T}{M_i}} \qquad [cm^2/s] \tag{2.21}$$

In mesopores, both molecular and Knudsen diffusion may be present. In this transition region, the Bosanquet equation, which accounts for both contributions, can be used [55]:

$$\frac{1}{D_{av}} = \frac{1}{D_{ij}} + \frac{1}{D_{i,K}} \tag{2.22}$$

Diffusion in the catalyst pores is described by the effective diffusion coefficient D_{eff}, which takes into account the particle porosity ε_p and the tortuosity τ_p. Due to the solid catalyst material, the volume in which diffusion can take place is reduced to the void volume defined by the particle porosity ε_p. The tortuosity accounts for the increased diffusion length relative to the spatial coordinate. Depending on the diffusion regime, the effective diffusivity can be expressed as [40]:

$$D_{eff} = \frac{\varepsilon_p}{\tau_p} \cdot D_{av} \approx 0.05 - 0.1 D_{av} \tag{2.23}$$

To describe the connection between reaction rate and diffusion limitation, Thiele [56] introduced a dimensionless number called the Thiele modulus. For an n^{th}-order irreversible reaction, the Thiele modulus can be expressed as:

$$\phi = \frac{k}{a' \cdot D_{eff}} \cdot \sqrt{\frac{\alpha+1}{2} c_s^{\alpha-1}} \tag{2.24}$$

The Thiele modulus gives the ratio of the chemical reaction rate (expressed as the rate constant k) to the diffusion rate (expressed as the effective diffusion coefficient D_{eff}). A small Thiele modulus indicates that there is no internal concentration gradient, while a large number indicates that the reaction is influenced by diffusion limitation. The internal effectiveness factor is defined as:

$$\eta_i = \frac{\text{observed reaction rate}}{\text{rate without internal gradients}} = \frac{\int r_v(c,T) dV}{r_{v,s}(c_s, T_s) V_p} \tag{2.25}$$

For a first order reaction and a slab geometry, the internal effectiveness factor can be written as:

$$\eta_i = \frac{tanh(\phi)}{\phi} = 1 \pm 0.05 \tag{2.26}$$

For the absence of internal diffusion limitation, the effectiveness factor should be 1 with a tolerance of 5 %. Since the kinetic measurement measures the observed reaction rate instead of the intrinsic reaction rate, it is not possible to verify whether the criterion is met, so a more convenient criterion is introduced, the Weisz-Prater modulus [57]. The following criterion can be derived for an n^{th}-order reaction from a series expansion [58].

$$\eta_i \phi^2 = \frac{r_{v,obs}}{c_s \cdot D_{eff} \cdot (a')^2} \left(\frac{\alpha+1}{2} \right) \leq \ 0.15 \tag{2.27}$$

The surface concentration can either be approximated by the bulk concentration c_b or calculated with the Equation 2.6. The approximation whether internal heat limitations

are present can be done analog to the evaluation of external gradients. Therefore the internal Prater number β_i, which represents the ratio of the heat production rate and the heat conduction rate in the particle, has to be evaluated (eq. 2.28):

$$\beta_i = \frac{(-\Delta H_R) \cdot D_{eff} \cdot c_s}{\lambda_{p,eff} \cdot T_s} = \frac{\Delta T_{max}}{T_s} \tag{2.28}$$

where $\lambda_{p,eff}$ is the effective thermal conductivity of the particle. Taking the product of the internal Prater number, the Weisz-Prater modulus and the Arrhenius number γ_s based on the surface temperature, the following criterion for the absence of temperature effects on the experimental data is obtained [58, 59].

$$\left|\gamma_s \cdot \beta_i \cdot \eta_i \phi^2\right| = \left|\left(\frac{Ea}{R \cdot T_s}\right) \cdot \left[\frac{(-\Delta H_R) \cdot D_{eff} \cdot c_s}{\lambda_{p,eff} \cdot T_s}\right] \cdot \left(\frac{r_{v,obs}}{(a')^2 \cdot D_{eff} \cdot c_s}\right)\right| < 0.1 \tag{2.29}$$

In laboratory measurements, the internal diffusion resistance can be reduced by reducing the size of the catalyst particles (crushing and sieving), thus increasing the number of exposed active sites. By reducing the size of the catalyst particles, the temperature gradients within the catalyst are also reduced. Internal diffusion limitation can be tested experimentally by operating a reactor at constant GHSV with different particle sizes. If the conversion decreases with increasing particle size, diffusion limitation is present (Figure 2.5 (b)).

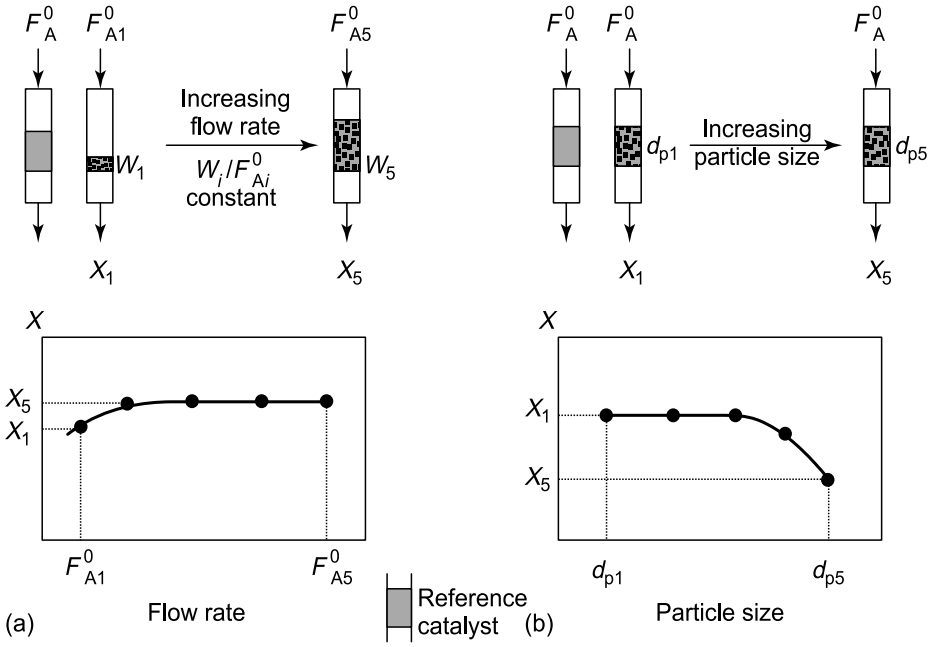

Figure 2.5: Experimental test of external (a) and internal (b) mass transfer limitation. Adapted from [40].

Catalyst Bed Gradients

According to Moulijn and Kapteijn [40], a temperature gradient within the packed-bed (T-grad$_{bed}$) can most likely occur. As the conversion increases, a temperature gradient develops that must be kept as small as possible. In the case of an exothermic reaction, the heat produced must be removed by the fluid phase flowing through the bed and by axial and radial heat conduction of the catalyst particles. In order to

minimize temperature gradients within the bed, radial heat conduction to the wall has the largest effect, while axial heat conduction is generally negligible due to the large length to diameter ratio in packed-bed applications. Thermal conduction occurs primarily through the fluid phase and the particles, which are poor conductors due to their porous structure and the fact that conduction between the particles occurs by their contact points. In addition, heat removal from the particle to the wall is hindered by the higher porosity in the wall region [60]. For a plug-flow reactor MEARS [61] obtained an approximate solution for the maximum temperature in the catalyst bed. For an isothermal rate considering the entire cross section of the reactor to obtain an average reaction rate a criterion with < 5 % deviation can be derived by Taylor series expansion of the rate based on MEARS results [40, 61]:

$$|\gamma_w \cdot \beta_w \cdot B_w| = \left| \left(\frac{Ea}{R \cdot T_w} \right) \cdot \left| \frac{r_{V,obs} \cdot (-\Delta H_R) \cdot d_t^2}{4 \cdot \lambda_{bed,eff} \cdot T_w} \right| \cdot \left(\frac{1}{8} + \frac{d_p}{Bi_{h,w} \cdot d_t} \right) \right| < 0.05 \quad (2.30)$$

Where the reaction rate $r_{V,obs}$ considers the catalyst bed porosity and the volume fraction b of an inert material from bed dilution (eq. 2.31).

$$r_{V,obs} = r_{v,obs} \cdot (1 - \varepsilon_{bed}) \cdot (1 - b) \quad (2.31)$$

Equation 2.30 resembles the criterion for the absence of external (eq. 2.11) and internal (eq. 2.29) gradients. The dimensionless activation energy based on the wall temperature T_w represents the first term. The ratio of the heat production rate to the heat conduction rate in the radial direction is described by the second term with the tube diameter d_t and the effective bed heat conductivity $\lambda_{bed,eff}$. The last term relates the radial conductivity to the heat transfer at the reactor wall with d_p as the particle diameter and $Bi_{h,w}$ as the Biot number for heat transport at the wall (eq. 2.32).

$$Bi_{h,w} = \frac{h_w \cdot d_p}{\lambda_{bed,eff}} \quad (2.32)$$

The heat transfer coefficient h_w and the effective thermal conductivity of the bed $\lambda_{bed,eff}$ can be calculated using the correlations given in [41, 62–64].

To overcome the obstacle of gradients within the catalyst bed in kinetic studies, the catalyst can be diluted in an inert solid with high thermal conductivity such as silicon carbide ($\lambda_{SiC} = 40$ W·m^{-1}·K^{-1}). In addition, small reactor tubes can be used for catalyst testing to reduce reactor diameter, thereby reducing the thermal transport resistance within the bed. For smaller reactor diameters it has to be considered that the particles have to be sufficiently small ($d_t/d_p > 10$) to obey the plug-flow criteria [65].

2.1.3 Basic Concepts in Chemical Kinetics

As explained in Chapter 2.1.1, heterogeneous reactions take place at the interface between two phases. How fast these reactions proceed is expressed by the reaction rate, which describes how many moles of a reactant are consumed or how many moles of a product are produced. To account for the catalyst phase in the rate expression, the mass (W) of the catalyst must be considered.

$$r = \frac{1}{W} \cdot \frac{d\xi}{dt}, \qquad [mol/kg \cdot s] \quad (2.33)$$

With the time derivative dt and ξ_i as the extent of reaction, describing the changes in the number of moles n_i involved in a reaction with the stoichiometric coefficient ν_i, defined as:

$$\xi_i = \frac{n_i - n_{i0}}{\nu_i} \qquad [mol] \quad (2.34)$$

Reaction rate studies aim at a phenomenological description of a system by a limited number of empirical constants. The aim is to measure the intrinsic reaction rate without any superimposed transport effect. Variables that influence reaction rates can be generalized as follows [66]:

1. The investigation of the reaction rate depends on the pressure, composition and temperature of the system.
2. Species that do not appear in the stoichiometric equation for the reaction can largely affect the reaction rate, even when present in trace amounts. These materials are known as catalysts or inhibitors, depending on whether they accelerate or slow down the reaction rate.
3. At constant temperature, the reaction rate decreases monotonically with time.
4. If the reaction is considered to be far from equilibrium, the rate can generally be expressed as:
$$r = k \cdot \Phi(c_i) \tag{2.35}$$
where $\Phi(c_i)$ is a function of the species concentration in the reaction mixture and k is the reaction rate constant. The rate constant is independent of composition and time in an isothermal system.
5. The rate constant depends on the reaction temperature according to the law proposed by Arrhenius:
$$k = A \cdot e^{\left(\frac{-Ea}{R \cdot T}\right)} \tag{2.36}$$
where A is the pre-exponential factor, which is assumed to be temperature independent, Ea is the activation energy and the universal gas constant R.
6. The function $\Phi(c_i)$ can be expressed as the product of the species concentration to the power of the reaction order:
$$\Phi(c_i) = \prod_i c_i^{\alpha_i} \tag{2.37}$$
The α_i are reaction orders with respect to each of the i species and can be small integers or fractions and can take both negative and positive values as well as zero.

The order indicates how the reaction rate varies with changing concentration and is a quantity to be determined experimentally.

In heterogeneous catalysis, the reaction takes place on the surface of the catalyst, so at least one reactant must be adsorbed on the surface. The adsorption must be strong enough to chemisorb the reactant and weak enough not to suppress interactions with the reactant and release the molecule. To account for the adsorption and desorption of a molecule Langmuir [67] introduced the Langmuir equation to express these steps mathematically. According to Langmuir, the rate of adsorption on a surface is proportional to the product of the partial pressure of the reactant in the gas phase and the fraction of empty surface (eq. 2.38).

$$r_{ads} = k_{ads} \cdot P_i \cdot (1 - \theta_i) \tag{2.38}$$

The fraction of the surface covered by the adsorbed species i is denoted as θ_i, the fraction of the empty surface is $1-\theta_i$ if no other species is adsorbed. The rate constant k_{ads} is the pseudo rate constant for the adsorption. The desorption depends only on the number of adsorbed molecules (eq. 2.39).

$$r_{des} = k_{des} \cdot \theta_i \tag{2.39}$$

At equilibrium, the rates of adsorption and desorption are equal, taking the ratio of the pseudo rate constants of adsorption and desorption, the equilibrium constant for adsorption (K_i) is obtained, leading to a fraction of sites occupied by species i, assuming a monolayer adsorption, to:

$$\theta_i = \frac{K_i \cdot P_i}{1 + K_i \cdot P_i} \tag{2.40}$$

A common and general approach of rate equations for solid or liquid catalyzed reactions is the Langmiur-Hinshelwood-Hougen-Watson (LHHW) model [68]. The LHHW model assumes that [20]:

1. At least one chemisorbed species is involved in the reaction.
2. For reactions with two adsorbed species, they must be adsorbed at adjacent sites.
3. The reaction of two adsorbed species is proportional to the product of the fractions of the sites occupied by each species.

The LHHW rate equation consists of three terms, as shown in Equation 2.41 [69].

$$r = \frac{(\text{rate factor}) \cdot (\text{driving force})}{(\text{adsorption term})^n} = \frac{k_{rds} \cdot \Gamma \cdot K_i \cdot P_i}{(1 + \sum_j K_j \cdot P_j)^n} \tag{2.41}$$

In the numerator, the rate factor consists of the apparent rate constant of the limiting step k_{rds}, the active site concentration Γ, and the adsorption equilibrium constant K_i. The driving force is a measure of how far the reaction is from thermodynamic equilibrium. The ethylene epoxidation reaction is known to be kinetically controlled and therefore far from equilibrium [70]. In the denominator, the adsorption term consists of all species adsorbed on the active sites, even if some of them do not participate in the surface reaction. This term always reduces the reaction rate by blocking active sites that cannot be used for the reaction. The exponent n on the adsorption term describes the number of surface species participating in the rate determining step [69].

In general, one of two mutually incompatible boundary cases is chosen for the analysis of a reaction rate expression. The assumptions are:

1. Adsorption equilibrium is maintained at all times and the overall reaction rate is controlled by the surface reaction.
2. The surface reaction is so fast that adsorption equilibrium is not reached. The adsorption or desorption rate is assumed to be much slower than the surface reaction and is therefore the rate controlling step.

Examples of several rate derivations are given in [71].

2.2 Differentially Operated Fixed-Bed Reactor

The "work-horse" and simplest type of a laboratory reactor for gas-solid reactions is the packed-bed tubular reactor, which consists of a reaction tube containing the catalyst between plugs or quartz wool. The reaction conditions dictate the material of the reactor, which is either glass for low temperature and pressure, quartz for high temperature, ceramic for high temperature and pressure, and steel for high pressure applications. Its optimal inner diameter is $4-6$ mm, especially to ensure sufficient heat transport to or from the catalyst [58]. The reactor can have a concentric geometry or, as in this work, a U-shaped tube containing the catalyst diluted with an inert material to reduce the heat generation by the exothermic reaction per unit volume

(thus operating under isothermal conditions) and to satisfy the plug flow criterion, which will be discussed further. Operating the plug flow reactor in differential mode means operating at very low conversions (< 5 %) of the limiting reagent, resulting in almost constant reactant concentrations throughout the reactor and approximately equal to the inlet concentration, as can be seen in Figure 2.6, where the inlet molar flow F_{i0} of species i, the outlet molar flow F_i, and the mass of catalyst ΔW inside the tubular reactor at low conversion of species i are shown. The reaction rate is assumed

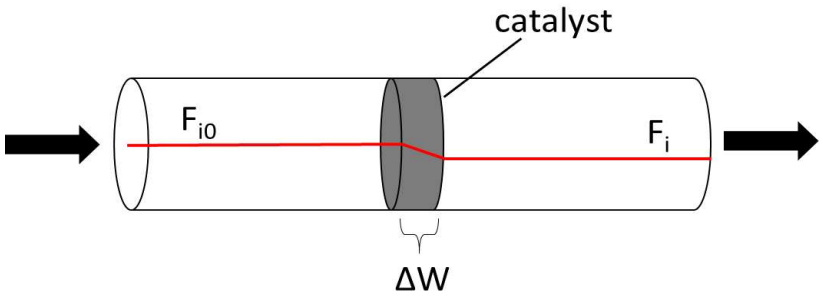

Figure 2.6: Illustration of a differential reactor with low consumption of species i.

to be spatially uniform within the bed and the reactor is assumed to be gradient-free [5]. Thus, the initial reaction rates (r_0) can be measured, since the inlet molar flow and the catalyst mass used are known, by performing a series of rate measurements at different initial reactant concentrations. Due to the differential behavior, the reaction rate can be obtained directly by applying the Equation 2.33, resulting in:

$$r_0 = \frac{F_{i0} - F_i}{\nu_i \cdot \Delta W} \tag{2.42}$$

Equation 2.42 is applicable to simple reactions; in the case of ethylene epoxidation, which is a parallel reaction, it is more convenient to evaluate the formation of products, assuming that the subsequent reaction of EO oxidation plays a minor role and can be neglected for O_2 conversion < 25 % and no EO in the feed stream [72, 73]:

$$r_{selective} = \frac{F_{EO}}{\Delta W} \tag{2.43}$$

$$r_{unselective} = \frac{F_{CO_2}}{2 \cdot \Delta W} \tag{2.44}$$

By varying the initial concentration of each component individually, it is possible to determine the order of reaction with respect to each species by linear or nonlinear regression. In addition, the plug flow criterion must be satisfied to apply the initial reaction rate Equations 2.43 - 2.44. A plug flow reactor can be considered as an infinite number of continuously stirred tank reactors (CSTR), each represented by a certain height of a slice of the catalyst bed, which corresponds to the equivalent height of mixing [40]. By reducing the length of the catalyst, deviations from plug flow towards more axial mixing can occur. This is described by the axial dispersion model, which relates the dimensionless Péclet number (Pe) to the N number of mixers in series [40].

$$2N = Pe = \frac{L_{bed} \cdot u_0}{D_{ax}} = \frac{L_b}{d_p} \cdot Pe_p \tag{2.45}$$

Where L_{bed} represents the catalyst bed length, D_{ax} the dispersion coefficient, d_p the particle diameter, and Pe_p the particle Péclet number, defined as:

$$Pe_p = \frac{u_0 \cdot d_p}{D_{ax}} \tag{2.46}$$

To obtain a sufficiently close approach, the Péclet number should exceed a certain value (for low $Re_p < 20 \rightarrow Pe_p \approx 0.3 - 0.7$) depending on the conversion X and the reaction order, resulting in a criterion for the minimum ratio of bed length to particle size [74].

$$\frac{L_b}{d_p} > \frac{8 \cdot \alpha}{Pe_p} \cdot ln\left(\frac{1}{1-X}\right) \tag{2.47}$$

Values for Pe_p as a function of Re_p can be found in the literature [41]. The reactor diameter also plays an important role in the plug flow behavior of the packed-bed process. Due to the higher porosity in the near wall region, higher local velocities can occur, causing channeling and deviation of the plug flow velocity field. To avoid this phenomenon, the following condition should be satisfied [65]:

$$\frac{d_t}{d_p} > 10 \tag{2.48}$$

where d_t represents the tube diameter. Especially for low conversions, the ratio of tube to particle diameter has a stronger effect than the ratio of bed length to particle diameter [40].

2.3 Ethylene Epoxidation

Ethylene oxide (Figure 2.7) is a colorless gas with a sweet, etheric odor and the simplest cyclic ether [10]. Due to its ring structure it is very active and therefore used for many applications in the chemical industry. Most of the ethylene oxide produced is converted to ethylene glycol, which is essential for the production of antifreeze. In addition, amines, surfactants and polyester are produced from ethylene oxide [10]. Due to its versatile application, ethylene oxide is one of the most important chemicals with an annual production of nearly 30.7 million metric tons in 2021 [9].

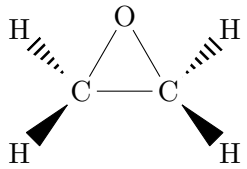

Figure 2.7: Sketch of an ethylene oxide molecule.

2.3.1 Industrial Ethylene Epoxidation Process

Ethylene oxide was first described by Wurtz [10] in 1859 by eliminating hydrochloric acid from ethylene chlorohydrin. The chlorohydrin process started in 1914 and was the first industrial process for ethylene oxide production. The chlorohydrin process was later replaced by the direct catalytic oxidation of ethylene with air (Union Carbide Corporation) or oxygen (Shell), discovered by Lefort [75] in 1931.

Chlorohydrin Process

The chlorohydrin process is a two-step process: In the first step, ethylene is converted with chlorine and water to ethylene chlorohydrin (eq. 2.49). In the second step, ethylene chlorohydrin is reacted with calcium hydroxide to form ethylene oxide (eq. 2.50).

$$C_2H_4 + Cl_2 + H_2O \rightarrow HOCH_2CH_2Cl + HCl \quad (2.49)$$

$$2\,HOCH_2CH_2Cl + Ca(OH)_2 \rightarrow 2\,C_2H_4O + CaCl_2 + 2\,H_2O \quad (2.50)$$

Although this reaction pathway has high selectivities with respect to EO, it was not competitive with the direct oxidation reaction. Due to the large amounts of waste produced, mainly $CaCl_2$, and by-products such as 1,2-dichloroethane that had to be separated, the chlorohydrin process was expensive compared to direct oxidation, whose main by-products are CO_2 and H_2O.

Catalytic Direct Oxidation

Union Carbide Corporation developed the first industrial process for the direct oxidation of ethylene to ethylene oxide with air over a silver catalyst in 1937, which was patented by Lefort [75] in 1935. Because of the high concentration of nitrogen in air, some of the reaction gas must be purged to keep the nitrogen concentration constant. To reduce ethylene losses, high ethylene conversions must be achieved, which in turn leads to lower EO selectivities. The reaction is carried out in two separate reactors. After passing the first reactor, high amounts of ethylene are still present in the reaction mixture. To reduce the ethylene content, a second reactor is used at a higher temperature to convert the remaining ethylene to EO. Industrially, direct oxidation via oxygen (developed by Shell) is the most common process to produce ethylene oxide; in this type of process, it is necessary to keep the C_2H_4 conversion below 10 % to prevent runaway conditions [76]. EO and CO_2 are separated from the product stream and the remaining ethylene is recycled. By recycling the unconverted ethylene, higher selectivities are achieved compared to the air oxidation process. Industrial reactors

Table 2.2: Operating Parameters Used in the Air and Oxygen Based Ethylene Oxide Production [10].

Parameter	Air-based process	Oxygen-based process
C_2H_4 concentration [vol-%]	$2-10$	$15-40$
O_2 concentration [vol-%]	$4-8$	$5-9$
CO_2 concentration [vol-%]	$5-10$	$5-15$
C_2H_6 concentration [vol-%]	$0-1$	$0-2$
Ar concentration [vol-%]	–	$5-15$
CH_4 concentration [vol-%]	–	$1-60$
Temperature [°C]	$220-277$	$220-275$
Pressure [bar]	$10-30$	$10-22$
GHSV [h^{-1}]	$2000-4500$	$2000-4000$
C_2H_4 Conversion [%]	$20-65$	$7-15$
Selectivity [%]	80	$80-90$

consist of several hundred tubular reactors with low d_t/d_p ratio (< 10) in parallel to enhance heat removal. The usual catalyst consists of a hollow cylinder of α-alumina on which promoted silver is supported. The hollow cylinder allows high velocities and a moderate pressure drop over the length of the reactor [22]. Halogenated hydrocarbons are added to the feed gas to suppress side reactions, which has a positive effect

on heat generation and EO selectivity. As can be seen in Table 2.2, the ethylene concentration is too high under industrial reaction conditions. To run the reaction safely, the ethylene concentration must be above the upper explosion limit ($2.6 - 36$ vol-% in air). Due to the higher reaction pressures typical of C_2H_4 production, the explosion limits for O_2 are different. At ambient conditions, an O_2 concentration of 15 vol-% is critical. At 20 bar the critical value shifts to 8 vol-% [77]. Comparing this value with the reaction parameters in Table 2.2, it can be seen that the reaction is already running at the limit, which makes the process very dangerous and difficult to control. Methane is added as an inert gas to the feed mixture because of its high heat capacity to reduce hot spots inside the reactor. In addition, impurities in methane and ethylene such as ethane are necessary to achieve adequate chlorine moderation of the catalyst, as reported by Berty [78]. The direct partial oxidation of ethylene to ethylene oxide

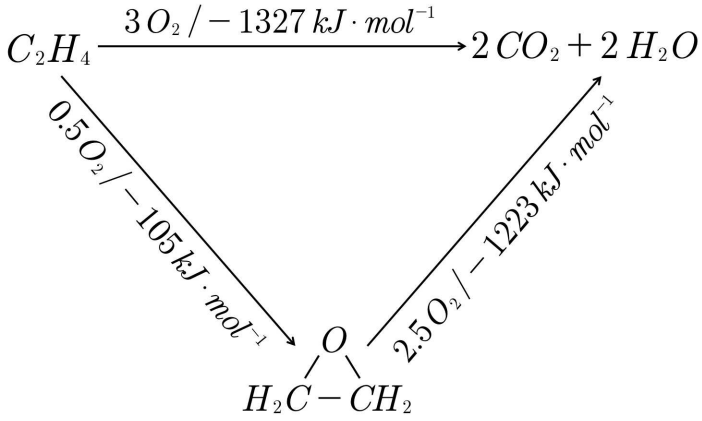

Figure 2.8: Triangular reaction scheme of partial ant total oxidation of ethylene and consecutive oxidation of ethylene oxide.

(Fig. 2.8) is a mildly exothermic reaction with a reaction enthalpy of -105 kJ·mol^{-1}, while the parallel total oxidation of ethylene and the subsequent oxidation of ethylene oxide are highly exothermic with -1327 kJ·mol^{-1} and -1223 kJ·mol^{-1}, respectively. Due to the high energy output of both side reactions, heat removal is a key issue to run the reaction safe and efficiently.

2.3.2 Literature Review

As mentioned above, EO is one of the most important intermediates produced in the chemical industry and the simplest example of a kinetically controlled, selective epoxidation reaction [70]. Many process improvements led to higher selectivities and work rates without changing the silver-based catalyst. Improvements included supporting the silver on α-alumina, on which the silver can be uniformly dispersed to avoid sintering of the silver particles, leading to decreased catalyst activity, or promoting the catalyst by adding ppm amounts of Cs, for example, leading to higher selectivities. By also adding halogenated hydrocarbons to the feed gas, selectivities up to 90 % can be achieved [10]. Silver catalyzes the parallel reactions, while the consecutive reaction is an isomerization of EO to acetaldehyde (AA), which is rapidly oxidized by silver to CO_2 and H_2O. The isomerization reaction is sensitive to the acidity of the catalyst support as found by Bulushev and Bukhtiyarov [79, 80]. Most of the research on EO production has focused on investigating why silver is the most efficient catalyst available. The EO selectivity of an unpromoted silver catalyst is about 40 % [81], but by continuously adding a halogenated hydrocarbon such as 1,2-dichloroethane or vinyl

chloride, the selectivity increases up to 70 % [81]. It has been shown that the addition of alkali metals during catalyst preparation leads to an even higher increase in selectivity to about 80 % [81]. Industrially used catalysts reach selectivities up to 90 % and are highly promoted with rhenium, tungsten, molybdenum and sulfur for example [10]. Although selectivities of 90 % can be considered sufficient, the ethylene epoxidation reaction is still the subject of academic and industrial research because even a slight increase in selectivity can have huge economic benefits. For a better understanding of past research and improvements, a brief overview of research on ethylene epoxidation is given here.

In early mechanistic studies, it was considered that molecular oxygen was the active component for the selective reaction to form EO, whereas atomic oxygen was responsible for the total oxidation. Kilty and Sachtler [72, 82] proposed that chlorine prevents the dissociation of molecular oxygen to atomic oxygen, thereby increasing the selectivity towards EO. According to this proposal, the EO selectivity is limited to 6/7 (85.7 %). Soon after the hypothesis was published, selectivities above 6/7 were reported [83, 84]. The active oxygen species for the selective reaction was found to be atomic oxygen [70, 85–88]. Force and Bell [89–91] postulated that chlorine's site blocking function lessens the quantity of surface atomic oxygen near vacancies, where the C−H activation occurs. Blocking of unoccupied sites adjacent to active atomic oxygen species prevents direct interaction between ethylene and the silver surface, thereby inhibiting the nonselective pathway that follows a Langmuir-Hinshelwood mechanism. Later, Özbek et al. [92] provided additional evidence for this site-blocking effect through investigation of chlorine promotion via DFT simulation.

Rocha et al. [93] and Bukhtiyarov et al. [94] reported the presence of three types of oxygen on the catalyst surface: a more selective oxygen (electrophilic), an unselective oxygen (nucleophilic), and a subsurface oxygen, the latter of which is reported to be required for selective oxidation of ethylene. Subsurface oxygen affects adsorbed atomic surface oxygen charge density, resulting in electrophilic surface oxygen (see Figure 2.9). The electron deficient oxygen interacts with the π-bond of ethylene, forming EO, rather than attacking C_2H_4 nucleophilically and leading to the combustion reaction. The impact of chlorine on the Ag−O bond strength is a frequently

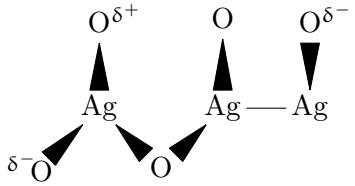

Figure 2.9: Influence of subsurface oxygen.

referenced topic. According to Torres [95], chlorine promotion results in increased EO selectivity by inducing a shift in the electronic structure of the Ag−O bond. The introduction of a compound with higher electronegativity than oxygen leads to electron withdrawal from silver, resulting in a more electrophilic oxygen species on the surface. Studies by Bowker and Waugh [96] indicate that at higher concentrations, chlorine diffuses into the subsurface of the catalyst, which increases the amount of subsurface oxygen (see Figure 2.10) as demonstrated by Campbell [86]. In addition, the combination of surface and subsurface chlorine promotes the desorption of EO and prevents the total oxidation of ethylene oxide as reported by Özbek et al. [92]. As has been recently pointed out by Lockemeyer and Lohr from Shell [97], EO catalysts must be carefully differentiated according to which promotors they contain.

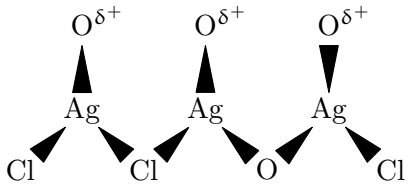

Figure 2.10: Influence of subsurface chlorine.

Apart from the plain 'Silver-Only' catalysts, alkali promoted 'High Activity' catalysts are distinguished from 'High Selectivity' catalysts containing additionally rhenium as a promotor. All the three catalyst classes, 'Silver-Only', 'High Activity' and 'High Selectivity' respond differently to chloride moderation in the feed and each type of catalyst operates at a different chloride optimum. For rhenium-free catalysts the activity decreases with higher chlorine moderation, whereas for rhenium-doped catalysts the activity increases with higher chlorine moderation [97].

The mechanism of chlorine deposition on silver catalysts was also studied by Berty [78], who proposed the following reactions:

$$C_2H_4Cl_2 + Ag + \frac{1}{4}O_2(Ag) \rightarrow C_2H_3Cl + AgCl + \frac{1}{2}H_2O(Ag) \tag{2.51}$$

$$C_2H_3Cl + Ag + \frac{1}{4}O_2(Ag) \rightarrow C_2H_2 + AgCl + \frac{1}{2}H_2O(Ag) \tag{2.52}$$

$$C_2H_6 + AgCl + \frac{1}{4}O_2(Ag) \rightarrow C_2H_5Cl + Ag + \frac{1}{2}H_2O(Ag) \tag{2.53}$$

In his experiments, he promoted a silver catalyst with 1,2-dichloroethane (DCE) and observed that a significant amount of DCE was missing at the outlet of the reactor. Small amounts of vinyl chloride (VC) and ethyl chloride (EC) were detected, as well as traces of methyl chloride (MC). Berty concluded that VC is formed when DCE reacts with the silver surface to form AgCl, while HCl is abstracted to form VC (eq. 2.51). Since VC can also be used to promote the catalyst, it can be further oxidized with surface oxygen (eq. 2.52) to form acetylene, which could not be detected during the measurement. The formation of EC is explained by the reaction of AgCl and surface oxygen with trace amounts of ethane present as an impurity in the C_2H_4 feed via oxychlorination to EC (eq. 2.53) [78, 98]. The oxychlorination reaction removes silver-bound chlorine, forming EC. This moderation of chlorine coverage is facilitated by organic molecules with sufficiently low C−H bond dissociation enthalpy, intermediate deprotonation enthalpy, and surface oxygen as shown by Harris et al. [99].

The kinetics of ethylene epoxidation have been studied in numerous publications. Different authors have proposed different rate expressions. Klugherz and Harriot [100] proposed a model in which ethylene and oxygen adsorb competitively on an oxygen layer adsorbed on the silver surface, with the rate-limiting step being a bimolecular reaction between ethylene and oxygen. Metcalf and Harriot [101] used the results of Klugherz and Harriot by adding a product inhibition term to the rate expression. Rates proceeding on the same catalytic site for both reactions were presented by Petrov et al. [102]. Bimolecular Langmuir-Hinshelwood relations were used by Ghazali et al. [103] and Park [104] to represent their data, where part of the catalytic surface is covered by deposits under reaction conditions. Stoukides and Pavlou [105] proposed an expression in which the selective and unselective reactions take place on the same catalytic site, also taking into account the consecutive oxidation of EO to CO_2 and H_2O. Al-Saleh et al. [106] accounted for the inhibition of CO_2 in their

studies using a Berty reactor. Borman and Westerterp [107] proposed a rate expression based on a Langmuir-Hinshelwood mechanism with a bimolecular reaction of adsorbed ethylene and dissociatively adsorbed oxygen. Lafarga et al. [108] presented a Langmuir-Hinshelwood mechanism in which the influence of oxygen adsorption was neglected. Carucci et al. [109] proposed two different models, considering either the surface reaction as the rate-determining step or the dissociative oxygen adsorption using a Langmuir-Hinshelwood mechanism. Microkinetic models were developed by Linic [110] and Stegelmann et al. [111] to describe the epoxidation reaction by formation of an oxametallacycle (OMC). Stegelmann et al. [111, 112] proposed a microkinetic model in which the reactants adsorb on an adsorbed oxygen layer, with a mechanism through formation of OMC. Linic and Barteau [12, 113–115] showed that the selective and unselective oxidation pathways have an OMC as a common surface intermediate. An OMC (see Figure 2.11) is formed as a result of surface atomic oxygen reacting with adsorbed ethylene through a Langmuir-Hinshelwood mechanism to produce either EO or AA, the latter being further oxidized to CO_2 and H_2O. As a consequence, the EO selectivity depends strongly on the relative barriers of the product formations through decomposition of the OMC intermediate [92]. Harris

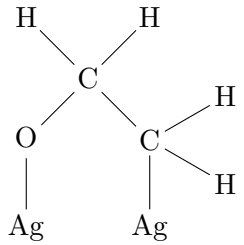

Figure 2.11: Sketch of oxametallacycle.

and Bhan [116] proposed chlorine deposition and removal kinetics by measuring the steady-state formation rates of propyl chloride with propane and EC in the feed stream. More recently, Iyer and Bhan [117] proposed a packed-bed reactor model that incorporates the independent catalytic cycles of ethylene epoxidation, chlorine deposition and removal, and EO degradation reactions, and describes the interdependencies of these reactions. The kinetic model of Iyer and Bhan [117] allows modeling of EO reactors filled with highly promoted $Ag/\alpha - Al_2O_3$ catalysts over a wide range of operation conditions because they managed to measure reaction rates at well defined chlorine coverages of the silver surface and report rate constants and reaction orders depending on θ_{Cl}.

2.4 Reactor Modeling

According to Froment and Bischoff [41], continuum models can be divided into two categories: the pseudohomogeneous and the heterogeneous model. The distinction is based on an analysis of the difference in temperature and concentration from the bulk fluid (b) to the catalyst surface (s):

- pseudohomogeneous models are applied for systems with: $T_b \approx T_s$ and $c_b \approx c_s$
- heterogeneous models are applied for systems with: $T_b \neq T_s$ and $c_b \neq c_s$

The simplest reactor model is the plug flow model, which assumes a radially uniform and constant velocity field. This pseudohomogeneous model considers the catalyst to be completely exposed to the bulk fluid phase without the presence of fluid-particle

heat and mass transfer resistances. The accuracy of this model approach can be improved by introducing a nonuniform velocity field. However, this comes at the cost of increased complexity. The heterogeneous model, on the other hand, describes the bulk fluid and the solid separately.

Pseudohomogeneous models are sufficient and can be used instead of heterogeneous models if both the interfacial mass and heat transfer gradients are small. Whether interfacial mass and heat transfer are negligible, can be verified using the criteria described in Chapter 2.1.2.

2.4.1 Axial and Radial Dispersion

If the inter- and intra-particle resistances can be neglected, the pseudohomogeneous model can be used to model the reactor. To account for a given non-ideal velocity flow field, it must be determined whether axial or radial dispersion should be included in the model. The dispersion coefficients describe the deviation from the ideal plug flow in the catalyst bed. In packed-beds, dispersion results not only from ordinary molecular diffusion and turbulence present in the absence of packing, but also from deflection and mixing due to the presence of catalyst particles [118]. Axial dispersion is negligible at the inlet when [119]:

$$\left| \frac{\alpha \cdot Da_I}{Pe_p} - \frac{\gamma_w \cdot Da_{III}}{Pe_h} \right| < 0.05 \tag{2.54}$$

where Da_I is Damköhler I, giving the ratio between chemical reaction rate and mass flow rate (eq. 2.55), Da_{III} is Damköhler III, giving the ratio between heat release and bulk heat transport (eq. 2.56). Pe_p is the particle Péclet number giving the ratio between bulk and conductive mass transfer, and Pe_h is the heat Péclet number giving the ratio between bulk (convective) and conductive heat transfer with λ_{ax} as the axial thermal conductivity (eq. 2.57):

$$Da_I = \frac{r_{v,obs} \cdot d_p}{u_0 \cdot c_{i0}} \tag{2.55}$$

$$Da_{III} = \frac{(-\Delta H_R) \cdot r_{v,obs} \cdot d_p}{\rho_f \cdot u_0 \cdot T_w \cdot c_{p,f}} \tag{2.56}$$

$$Pe_h = \frac{\rho_f \cdot u_0 \cdot d_p \cdot c_{p,f}}{\lambda_{ax}} \tag{2.57}$$

Equation 2.54 can be applied to both types of models, pseudohomogeneous and pseudo-heterogeneous. If radial dispersion is present, a 2D model must be chosen to account for radial mixing in the packed-bed reactor. Since radial mass transfer effects are negligible compared to radial heat transfer effects [120], it is sufficient to evaluate the criteria for heat transfer limitations in the catalyst bed (eq. 2.30) introduced in Chapter 2.1.2 [119].

2.4.2 1D Pseudohomogeneous Model

Accurate kinetic parameters are essential to correctly reproduce experimental concentration and temperature profiles by simulation. In this work, kinetic parameters were determined by initial reaction rate measurements in a differentially operated fixed-bed reactor and by fitting concentration and temperature profiles measured in the CPR described in Chapter 5.1 and Chapter 5.2.4, respectively. After the evaluation of transfer resistances and dispersion criteria (Chapter 5.2.1 and Chapter 5.2.4), the 1D

pseudohomogeneous plug flow model was chosen to simulate the concentration and temperature profiles, in the axial direction of the bed. At steady state, the molar balance for this particular case takes the following form:

$$u_0 \frac{dc_i}{dx} = \sum_k \nu_{ik} \cdot r_k \cdot \rho_{bed} \qquad [mol \cdot m^{-3} \cdot s^{-1}] \tag{2.58}$$

The mole balance equals the plug flow model with u_0 being the superficial velocity and c_i the concentration of each gas component. The sum includes the stoichiometric coefficient of the component i in the reaction k and the reaction rate of the reaction k multiplied by the bed density. The following heat balance was used for the temperature behavior:

$$\rho_f \cdot c_{p,f} \cdot u_0 \frac{dT}{dx} = \sum_k r_k \cdot (-\Delta H_{r,k}(T)) \cdot \rho_{bed} - 4 \cdot \frac{U}{d_t} \cdot (T - T_w) \qquad [W \cdot m^{-3}] \tag{2.59}$$

The heat production by the exothermic reactions is considered by the product of reaction rate r_k and the heat of the k^{th} reaction $\Delta H_{r,k}(T)$ at the reaction temperature T. The density of the reaction mixture was calculated using the ideal gas law:

$$\rho_f = \frac{M_f \cdot p}{R \cdot T} \qquad [kg \cdot m^{-3}] \tag{2.60}$$

The heat capacity of the mixture was calculated according to the VDI Heat Atlas [121]. The temperature change was taken into account as follows:

$$\frac{c_{p,i}}{J/kg \cdot K} = A_i + B_i \left(\frac{T}{K}\right) + C_i \left(\frac{T}{K}\right)^2 + D_i \left(\frac{T}{K}\right)^3 + \frac{E_i}{(T/K)^2} \tag{2.61}$$

The heat capacity of the reaction mixture was calculated according to Equation 2.62 using the mass fractions w_i of all components i and their heat capacities at constant pressure:

$$c_{p,f} = \sum_i w_i \cdot c_{p,i} \qquad [J \cdot kg^{-1} \cdot K^{-1}] \tag{2.62}$$

The overall heat transfer coefficient U was calculated according to Dixon [122]:

$$\frac{1}{U} = \frac{1}{h_w} + \frac{d_t}{6\lambda_{bed,eff}} \cdot \frac{Bi_{h,w} + 3}{Bi_{h,w} + 4} \qquad [m^2 \cdot K \cdot W^{-1}] \tag{2.63}$$

with $Bi_{h,w}$ being the Biot number at the wall. The momentum balance was solved according to Ergun [123]:

$$-\frac{dp}{dx} = 150 \cdot \frac{(1 - \varepsilon_{bed})^2}{\varepsilon_{bed}^3} \frac{\eta_f \cdot u_0}{d_p^2} + 1.75 \cdot \frac{(1 - \varepsilon_{bed})}{\varepsilon_{bed}^3} \frac{\rho_f \cdot u_0^2}{d_p} \tag{2.64}$$

The set of governing equations is closed by the continuity equation:

$$\rho_f \cdot u_0 = const. \tag{2.65}$$

To solve the set of first-order ordinary differential equations, the following conditions were applied at the inlet of the catalyst bed in the CPR:

$$\text{inlet conditions: } x = 0, \quad c_i = c_{i0}, \quad T = T_{\text{in}}, \quad p = p_{\text{in}} \tag{2.66}$$

2.4.3 Parameter Regression from Profile Measurements

The rate laws were derived by means of a differentially operated fixed-bed reactor and a literature mechanism postulated by the group of SCHLÖGL [18]. Profiles measured in the Compact Profile Reactor were used to fit the pre-exponential factors, activation energies and adsorption enthalpies using Comsol Multiphysics 5.5^{TM} applying the Levenberg-Marquardt solver algorithm. The method of the sum of squares minimization was applied to minimize the error of the measured and the fitted profiles using a plug flow model as described in Chapter 2.4.2. All profiles were fitted simultaneously to obtain parameters valid for all measured conditions.

2.4.4 2D Pseudohomogeneous Model

Profile measurements were performed in a PSPR with static capillaries for kinetic model validation described in Chapter 4.3. Due to the evaluation of eq. 5.42 described in Chapter 5.3.1 of the criteria of axaial and radial dispersion (Chapter 2.4.1), a 2D pseudohomogeneous model was chosen to simulate the molar flow rate and temperature profiles in the PSPR using ComSol Multiphysics 5.5^{TM}. Mass and heat transfer were taken into account, together with the momentum balance considering the radial porosity of the bed by the Brinkman equation including radial porosity profiles and effective viscosity [63, 124]. The profiles were simulated by solving the following equations:

Mole balance:

$$\varepsilon_{bed} \cdot D_{r,i} \left(\frac{\partial^2 c_i}{\partial r^2} + \frac{1}{r} \frac{\partial c_i}{\partial r} \right) = \frac{\partial (u c_i)}{\partial z} - \varepsilon_{bed} \cdot D_{ax,i} \frac{\partial^2 c_i}{\partial z^2} + \sum_k \nu_{ik} \cdot r_k \cdot \rho_{bed} \tag{2.67}$$

Heat balance:

$$\lambda_r \left(\frac{\partial^2 T}{\partial r^2} + \frac{1}{r} \frac{\partial T}{\partial r} \right) = \rho_f \cdot u \cdot c_{p,f} \frac{\partial T}{\partial z} - \lambda_{ax} \frac{\partial^2 T}{\partial z^2} - \sum_k r_k \cdot (-\Delta H_{r,k}(T)) \cdot \rho_{bed} \tag{2.68}$$

The mass and heat transfer parameters were calculated according to TSOTSAS [63] and WINTERBERG et al. [125]. The equations were modified to meet the needs of the simulation in this work, where the reactions take place in an annular gap between the reactor wall and the sampling capillaries. The radial and axial dispersion were calculated according to the following equations:

$$D_{r,i} = 1 - \sqrt[2]{1 - \varepsilon_{bed}(r)} \cdot D_{12} + K_{1,q} \cdot Pe_m \cdot \frac{u(r_0)}{u} \cdot f(R - r)_1 \cdot D_{12} \tag{2.69}$$

with

$$r_0 = \frac{R_o + R_i}{2} \tag{2.70}$$

$$D_{ax,i} = 1 - \sqrt[2]{1 - \varepsilon_{bed}(r)} \cdot D_{12} + \frac{u \cdot d_p}{2} \tag{2.71}$$

with $K_{1,q}$ as the slope parameter for spherical split particles, $K_{2,q}$ as the damping factor close to the reactor wall [63]:

$$K_{1,q} = \frac{1}{5.7} \cdot \left[1 + \frac{3}{\sqrt{Pe_m, c}} \right]^{-1} \tag{2.72}$$

$$K_{2,q} = 0.44 \tag{2.73}$$

$$f(R-r)_1 = \begin{cases} \left[\frac{r-R_i}{K_{2,q}\cdot d_p}\right]^2 & \text{if } R_i < r \leq K_{2,q}\cdot d_p + R_i \\ 1 & \text{if } K_{2,q}\cdot d_p + R_i < r \\ 1 & \text{if } r < R_o - K_{2,q}\cdot d_p \\ \left[\frac{R_o-r}{K_{2,q}\cdot d_p}\right]^2 & \text{if } R_o - K_{2,q}\cdot d_p \leq r < R_o \end{cases} \tag{2.74}$$

and D_{12} as the molecular diffusion coefficient of C_2H_4 in N_2 according to the Chapman-Enskog theory (eq. 2.17) [47]. The remaining species were neglected, since the C_2H_4-N_2 mixture contains more than 90 % of the total gas volume.

$$\lambda_r = \lambda_{bed}(r) + \frac{1}{K_r}\cdot Pe_h \cdot \frac{u(r_0)}{u}\cdot \lambda_f \cdot f(R-r)_2 \tag{2.75}$$

$$\lambda_{ax} = \lambda_{bed}(r) + Pe_h \cdot \frac{\lambda_f}{2} \tag{2.76}$$

$$f(R-r)_2 = \begin{cases} \left[\frac{r-R_i}{K_{2,r}\cdot d_p}\right]^2 & \text{if } R_i < r \leq K_{2,r}\cdot d_p + R_i \\ 1 & \text{if } K_{2,r}\cdot d_p + R_i < r \\ 1 & \text{if } r < R_o - K_{2,r}\cdot d_p \\ \left[\frac{R_o-r}{K_{2,r}\cdot d_p}\right]^2 & \text{if } R_o - K_{2,r}\cdot d_p \leq r < R_o \end{cases} \tag{2.77}$$

$$K_{1,r} = \frac{1}{5.7} \tag{2.78}$$

$$K_{2,r} = 0.44 + 4\cdot exp\left(-\frac{Re}{70}\right) \tag{2.79}$$

The momentum balance corresponds to the extended Brinkman equation, which is a modification of the general Navier-Stokes equation that takes flow through porous media and free flow into account [63, 126]:

$$\frac{dp}{dx} = -f_1\cdot u(r) - f_2\cdot [u(r)]^2 + \frac{\eta_f}{r}\cdot\frac{\partial}{\partial r}\left(r\frac{\partial u(r)}{\partial r}\right) \tag{2.80}$$

Friction loss caused by the packed-bed is calculated using the Ergun resistance parameters:

$$f_1 = 150\cdot\frac{[1-\varepsilon_{bed}(r)]^2}{[\varepsilon_{bed}(r)]^3}\cdot\frac{\eta_f}{d_p^2} \tag{2.81}$$

$$f_2 = 1.75\cdot\frac{[1-\varepsilon_{bed}(r)]}{[\varepsilon_{bed}(r)]^3}\cdot\frac{\rho_f}{d_p} \tag{2.82}$$

with the effective viscosity depending on the Reynolds number and the viscosity of the gas mixture [124]:

$$\eta_f = 2\cdot exp\,(Re\cdot 0.002)\cdot\eta_{mix} \tag{2.83}$$

Continuity equation:

$$\nabla\cdot(\rho_f\mathbf{u}) = 0 \tag{2.84}$$

The extended Brinkman equation is recommended for velocity field calculations due to the consideration of wall effects on the flow in fixed-bed reactors by the introduced radial function of the bed porosity $\varepsilon_{bed}(r)$. The radial porosity distribution for an annular fixed-bed can be written as [127]:

$$\varepsilon_{bed}(r) = \varepsilon_0\cdot\left[1 + C\cdot exp\left(-N\cdot\frac{r-R_i}{d_p}\right)\right] \quad \text{for} \quad R_i \leq r \leq \frac{R_o+R_i}{2} \tag{2.85}$$

$$\varepsilon_{bed}(r) = \varepsilon_0 \cdot \left[1 + C \cdot exp\left(-N \cdot \frac{R_o - r}{d_p}\right)\right] \quad \text{for} \quad \frac{R_o + R_i}{2} \leq r \leq R_o \tag{2.86}$$

where R_i is the inner radius of the annulus, R_o is the outer radius, and $\varepsilon_0 = 0.38$ as the bulk porosity of the bed. The value of $C = 1.63$ was taken to give a porosity of 1 at the wall, and the value of $N = 2$ according to VORTMEYER and SCHUSTER [128].

The boundary conditions in Table 2.3 were used to solve the set of conservation equations.

Table 2.3: Boundary Conditions Applied to the Two Dimensional Reactor Model.

$z = 0, \forall r$:	$c_i = c_{i,0}$	$T = T_0$	$\lvert\vec{u}\rvert = u_0$
$z = L, \forall r$:	$\frac{\partial c_i}{\partial z} = 0$	$\frac{\partial T}{\partial z} = 0$	$p = 1$ [atm]
$r = R_i, \forall z$:	$\frac{\partial c_i}{\partial r} = 0$	$\frac{\partial T}{\partial r} = 0$	$u = 0$
$r = R_o, \forall z$:	$\frac{\partial c_i}{\partial r} = 0$	$T = T_w$	$u = 0$

3 Construction

For kinetic investigations of the ethylene epoxidation reaction, a kinetic test setup was constructed to measure kinetic parameters under differential conditions, which is described in Chapter 3.1. In addition, the design of a Pilot Scale Profile Reactor in which partial oxidation was studied by measuring concentration and temperature profiles under near-industrial conditions, resolving promoter profiles in the subppm range, is described in Chapter 3.2.

3.1 Differential Reactor Design

A kinetic test reactor was designed to measure intrinsic kinetic parameters at industrial pressure and temperature conditions in a differentially operated fixed-bed reactor. The flow diagram of the setup is shown in Figure 3.1. The reactor consisted of a U-shaped stainless steel tube (reaction zone: 1/4 inch (=6.35 mm), upstream and downstream: 1/8 inch (=3175 mm)) located in a fluidized sand bath for optimal temperature control. The sand bath was fluidized and heated by compressed air, which could be adjusted by a rotameter. Typical flow rates of $2-8$ L_N/sec were applied depending on the minimum fluidization velocity, which is a function of temperature, particle density and particle size [129]. A heater consisting of a steel pipe with a glass-wrapped heating wire was used to heat the compressed air. In case of malfunction of the compressed air system in the building, a safety device was implemented in front of the heater, which requires a minimum flow rate of 0.1 L_N/sec. If the compressed air flow is too low, the heater automatically switchs off and can only be reseted manually. The hot air temperature is controlled by a Eurotherm temperature controller (Model No. 2132) which controls the temperature via a type-K thermocouple. It was placed in the bottom of the fluidized bed between the heater and the bubble tray. The heated air passed through the tray into the sand bath where it heated and fluidized the sand. The advantage of the fluidized bed approach is that the heat is distributed evenly throughout the sand bath, creating an isothermal zone [130]. In addition, a heating jacket, which could be heated up to 1100 °C, was wrapped around the fluidized bed to reduce heat loss through the wall. To further minimize heat loss, a steel plate enclosure was built around the fluidized bed with insulation built in (Figure 3.2). With such a setup, temperatures up to 550 °C could be reached.

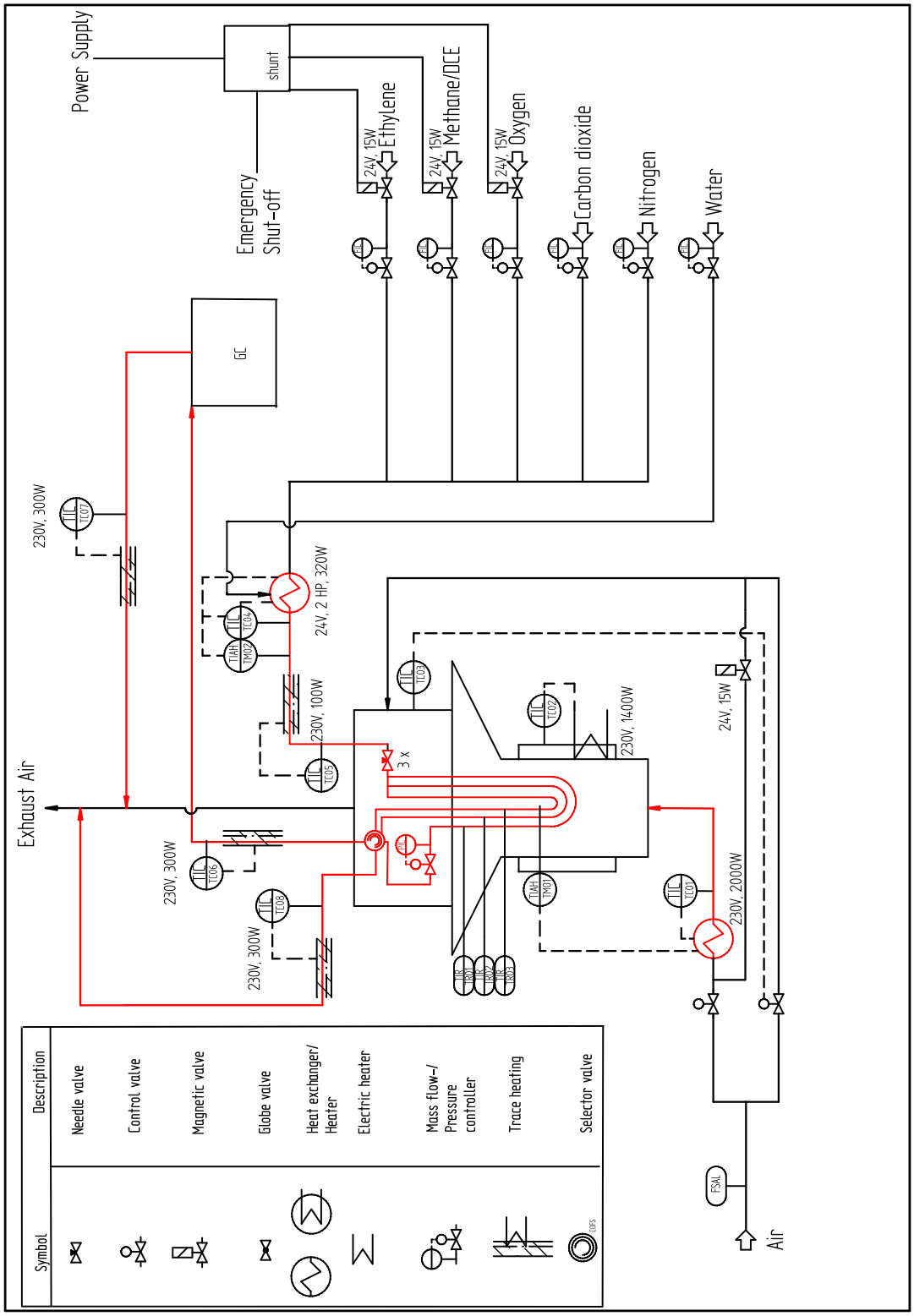

Figure 3.1: Flow diagram of the kinetic test setup.

The kinetic test setup was designed to run reactions in three reactors in parallel, e.g. for catalyst testing. Since the volumetric flow rate inside the reactor is highly dependent on the pressure drop across the fixed bed, needle valves were used to adjust the pressure drop across the fixed bed reactors, thus controlling the volumetric flow rate to each of the reactors. The needle valves were located above the fluidized sand

bath in a heated zone to prevent condensation inside the valves.

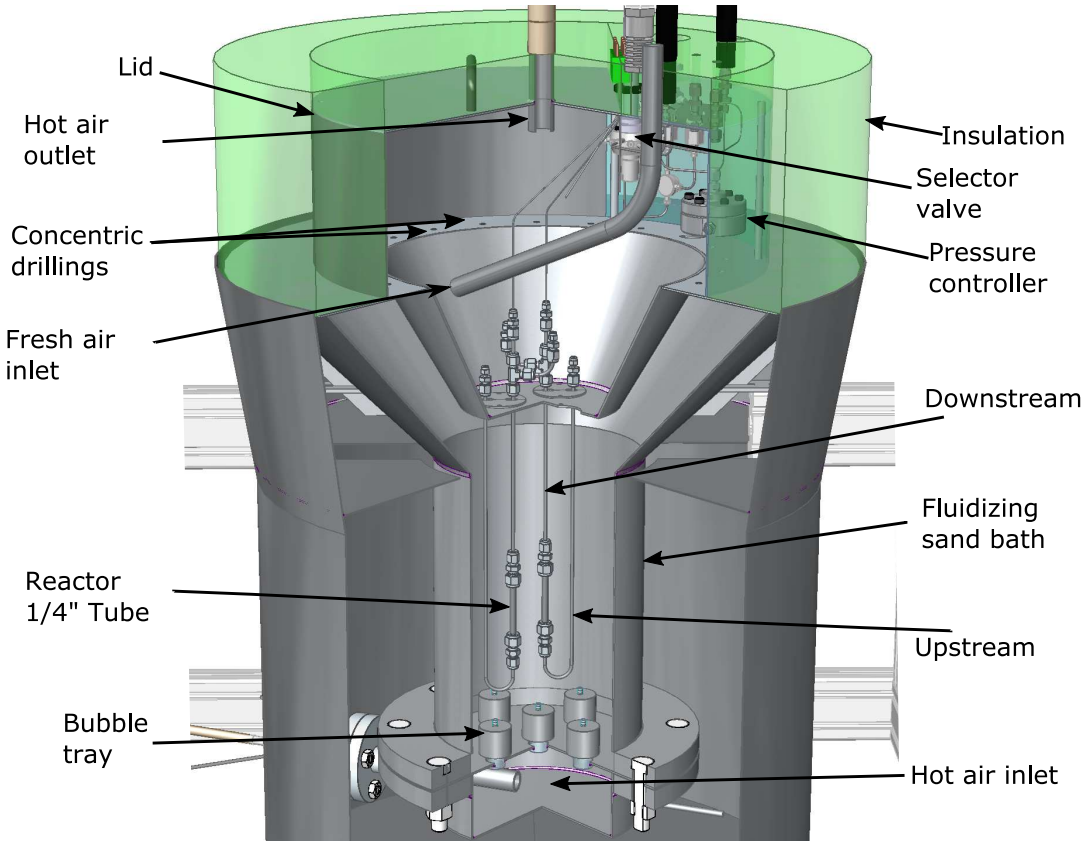

Figure 3.2: Sketch of the differentially operated isothermal fixed-bed reactor inside a heated fluidized sand bath.

In the case of the EO reaction investigated in this work, additional precautions had to be taken: due to the risk of EO condensation and the fact that EO tends to polymerize, all tubes that could contain EO had to be heated to ensure safe operation of the reactor. For this purpose, 6 mm concentric holes were made in the upper part of the fluidized bed to direct the hot air used to heat the sand to the upper part of the fluidized bed where all the tubes to the inlet of the U-shaped reactor and the outlet were located. Since the reaction took place at a higher pressure of 17 bara, the pressure regulator was also located in the upper part, as well as the needle valves used to divide the inlet feed to the three parallel reactors. To maintain the temperature in the section above the fluidized bed, a cover was placed on top of the bed. To reduce heat loss from the cover, it was wrapped in an insulation jacket filled with glass wool. High temperatures are necessary for kinetic measurements to ensure fast reactions. However, these conditions can cause problems with gaskets whose materials are typically only applicable to 260 °C (in the case of PTFE) or lower. Since the setup was designed for temperatures up to 550 °C, there was a risk of damage and leakage of the pressure regulator used, which was designed for a maximum of 200 °C. To prevent damage, a fresh air inlet was installed to control the temperature under the cover. Fresh air could be supplied tangentially, creating a flow field similar to that of a cyclone, which in turn provided a uniform temperature distribution through turbulent mixing of fresh and hot air. The position of the inlet was chosen based on the results of a CFD study by Eugenio Gil Quessepp (project thesis) to obtain a uniform temperature distribution under the lid without creating hot or cold spots

that could cause EO decomposition. The temperature under the cover was measured with a type-K thermocouple covered with a tube. The limit temperature was set at 200 °C. When this temperature was reached, a proportional valve was opened and cold compressed air was injected into the cover until the temperature dropped below 200 °C. The lower the temperature dropped, the less fresh air was supplied by the proportional valve. This was done to avoid large temperature fluctuations under the hood.

Gas composition analysis was performed by gas chromatography (Agilent 7890B). For GC calibration, the reactor was bypassed and the gas flow was directed to a selector valve. The stream selection (reacted gas mixture or bypass flow) was realized by a common outlet selector valve (Vici Valco). One stream was selected for measurement in the GC, while the remaining gas streams were routed to the exhaust in the fume hood.

The feed gas was provided by a modular gas supply designed and built for high flexibility in gas species. Gas modules have the advantage of being "plug and play" type and provide standards for connecting multiple modules together. Everything necessary for a gas supply (except the electronics) is already built into a module. Figure 3.3 shows a gas module for flammable gas, which includes a filter, a pressure reducer, the mass flow controller, the solenoid valve, and electronic connectors for the control box purchased from Bronkhorst to control the mass flow and pressure of the reaction.

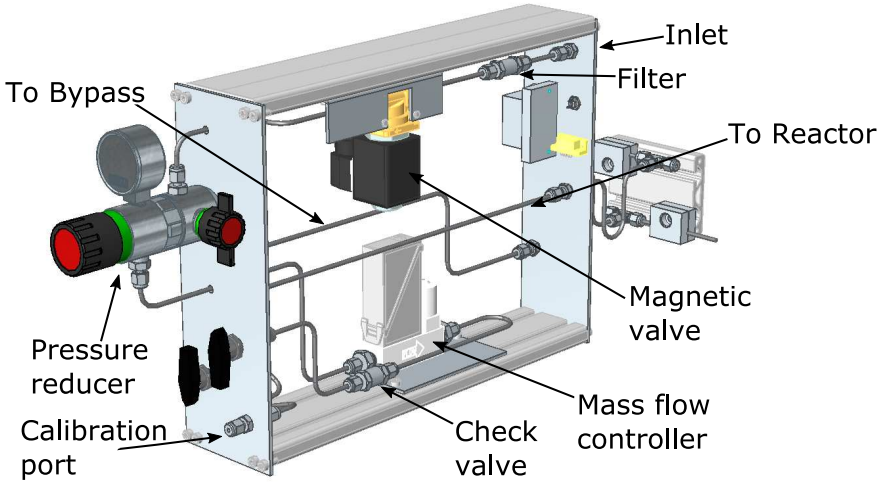

Figure 3.3: Sketch of the gas module designed for the gas supply.

Three-way valves mounted on the front panel provide the option of directing the gas either to a calibration port on the front panel, to the reactor, or to a bypass that establishes a mass flow before directing the gas to the reactor, thus preventing overshooting of the gas dosage. Each gas species was metered with such a module, with only the flammable gas modules equipped with a solenoid valve. Since water vapor was one of the required species in the reaction mixture, liquid water was dosed into an evaporator before being fed into the reactor. For this purpose, water required a special module that allowed pressurizing a water-filled reservoir to provide pressurized water to the Bronkhorst Liqui-Flow. The water module is shown in Figure 3.4.

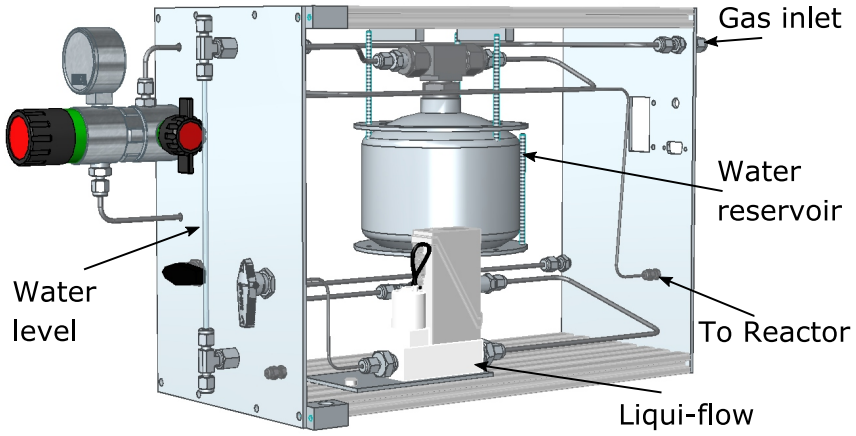

Figure 3.4: Sketch of the water module supply design to supply liquid water to the evaporator.

The water module is similar in design to the gas module. The main difference is the vessel inside the module, which can be pressurized up to 40 bara. Helium was used to pressurize the water-filled vessel because it was one of the gases already used in the setup (carrier gas for the GC) and the solubility in water is lower than that of e.g. nitrogen [131]. The water level inside the vessel could be monitored by the PTFE tube mounted on the front plate. The liquid flow inside the module controlled the water mass flow to the evaporator, which was a 1/2 inch (=12.7 mm) tube filled with steel spheres. The evaporator was heated by two 100 mm long heating cartridges with a total power of 320 W placed in drilled holes of two aluminium shells around the 1/2 inch tube (Figure 3.5).

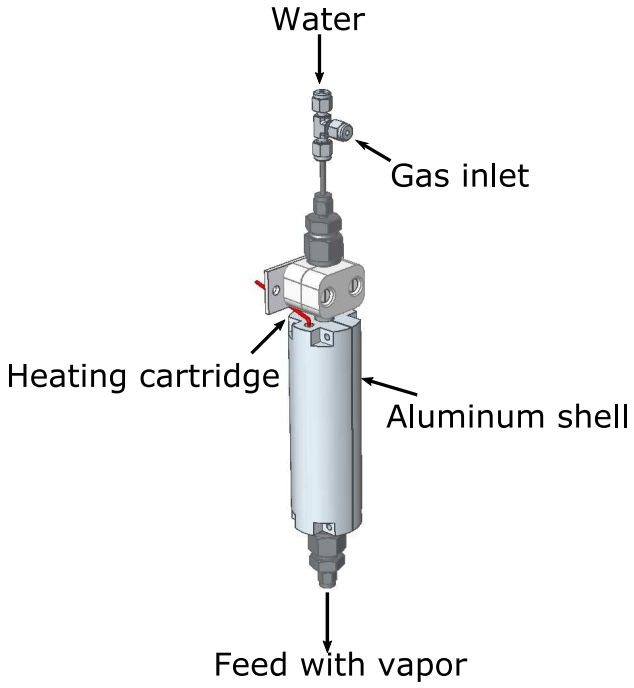

Figure 3.5: Sketch of the water evaporator design to supply vapor feed to the reactor.

The water entered the evaporator through a 1/16 inch (=1.5875 mm) tube with an inner diameter of 400 µm, which was in direct contact with the steel spheres to prevent sudden evaporation. The contact of the water feed tube with the sphere packing was designed to provide uniform wetting of the sphere and avoid droplet formation, resulting in a continuously constant vapor concentration in the feed. The remaining feed gas, flows through the packing and acts as a carrier gas to transport the steam into the reactor.

A heated tube was installed at the outlet of the evaporator to heat the gas feed tube to the reactor, to prevent water condensation at the reaction pressure of 17 bara. In the case of the ethylene epoxidation reaction system, only one of the three parallel reactors was used, since only one pressure regulator was available. The pressure regulator (Equilibar) consists of a steel block with orifices. The desired reaction pressure was set by applying pressure (extra line of nitrogen) to a membrane covering the orifices inside the steel block. This technique allows very precise pressure adjustments, with low oscillations during the reaction.

The electronics housing, which was necessary to operate the reactor, contained all the temperature controllers for heating the fluidized bed, the heating tubes and the evaporator. The power distribution and emergency shutdown were also built into the electronics housing. The whole setup is shown in Figure 3.6.

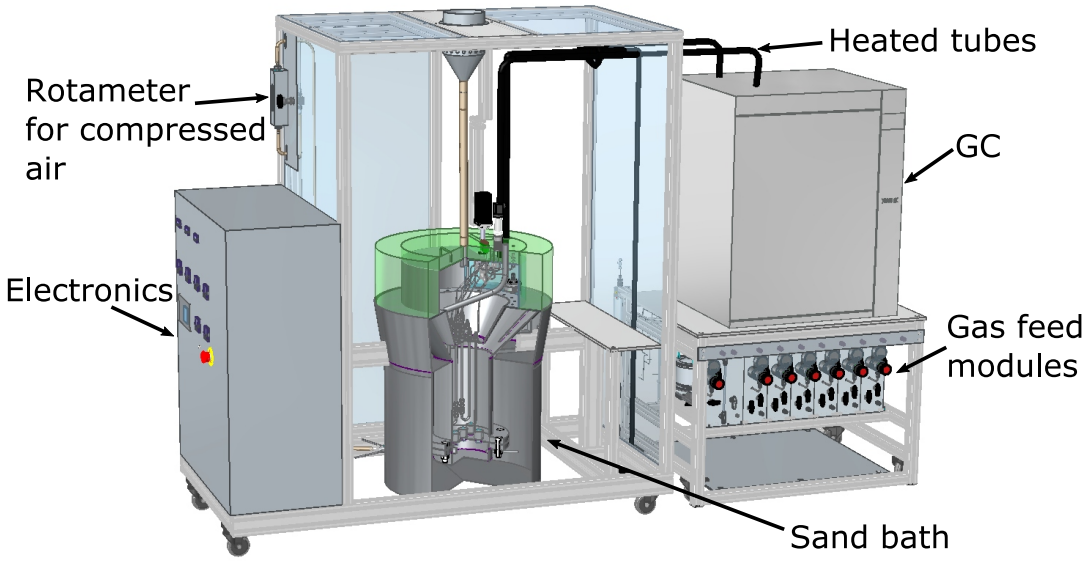

Figure 3.6: Sketch of the kinetic test setup with the fluidized sand-bath, gas feed modules, GC and electronics housing.

Because EO is flammable and carcinogenic, the kinetic reactor was built inside a fume hood connected to the building's exhaust system. The hot air from heating all tubes under the cover was routed through a hose where it entered the exhaust port of the fume hood and the building's exhaust system. In order to ensure that the hot exhaust air would not damage the building's exhaust system and to ensure proper air exchange in the kinetic setup enclosure, an exhaust port was designed to connect the building's exhaust system to the setup. This connection combined the hot air from the fluidized bed and the air inside the enclosure, thus cooling the exhaust prior to entering the building's exhaust system.

3.2 Pilot Scale Profile Reactor Design

This chapter focuses on the spatial reactor design, developed to study the ethylene epoxidation reaction within a Pilot Plant Scale Fixed Bed Reactor. The measurement principle is based on the profile measurement technique developed by HORN et al. [15]. This required a gas supply unit, a reaction unit and an exhaust gas treatment unit. In addition, a fully automated process control system was designed to operate the reactor unattended.

3.2.1 Piping and Instruments

A PSPR was designed to measure concentration and temperature profiles for the epoxidation reaction of ethylene to EO. For proper planning, the flowchart was divided into sections 10 to 40, each consisting of a part of the entire reactor setup, which was created according to DIN EN ISO 10628 [132]. Section 10 defines the gas supply, section 20 the evaporation and dosing of water, section 30 the reaction and analysis zone and section 40 the off-gas treatment.

Symbols for equipment and valves were taken from DIN 28000-5 if a definition existed [133]. If there was no definition for a certain part, a symbol was created. A legend of the symbols used for the P&ID is shown in Figure 3.7. All instruments are numbered for exact identification. The starting number defines the section in which the instrument is located, followed by an abbreviation of the instrument name and a sequential number, e.g. 10GV07 means the instrument is located in section 10, the instrument is a Globe Valve (GV) and its individual number is seven. The P&ID gives a good overview of the setup and allows for detailed engineering.

On the bottom side of the P&ID (Figure 3.7) section 10 is shown with the gas supply and all instruments required to control the gas supply. Water is pressurized with helium in a steel vessel to provide the Liqui-Flow controller (Bronkhorst) with liquid water at the pressure required for the reaction. Due to the hazardous conditions of the ethylene epoxidation reaction, i.e. highly exothermic unselective reaction, all flammable and oxidizing gases are equipped with pneumatic shut-off valves to cut off the gas flow in case of emergency similar as it was done in the differential reactor setup in Chapter 3.1.

A nitrogen line is guided to the reactor outlet to dilute the outlet flow to prevent EO decomposition or polymerization in the pressure regulator. Section 20 is located directly in front of the reactor and shows the gas mixing equipment and the evaporator for the vapor feed. Section 30 shows the packed reactor, sampling equipment and GC's. Section 40 shows the buffer vessel and combustion chamber for exhaust gas treatment.

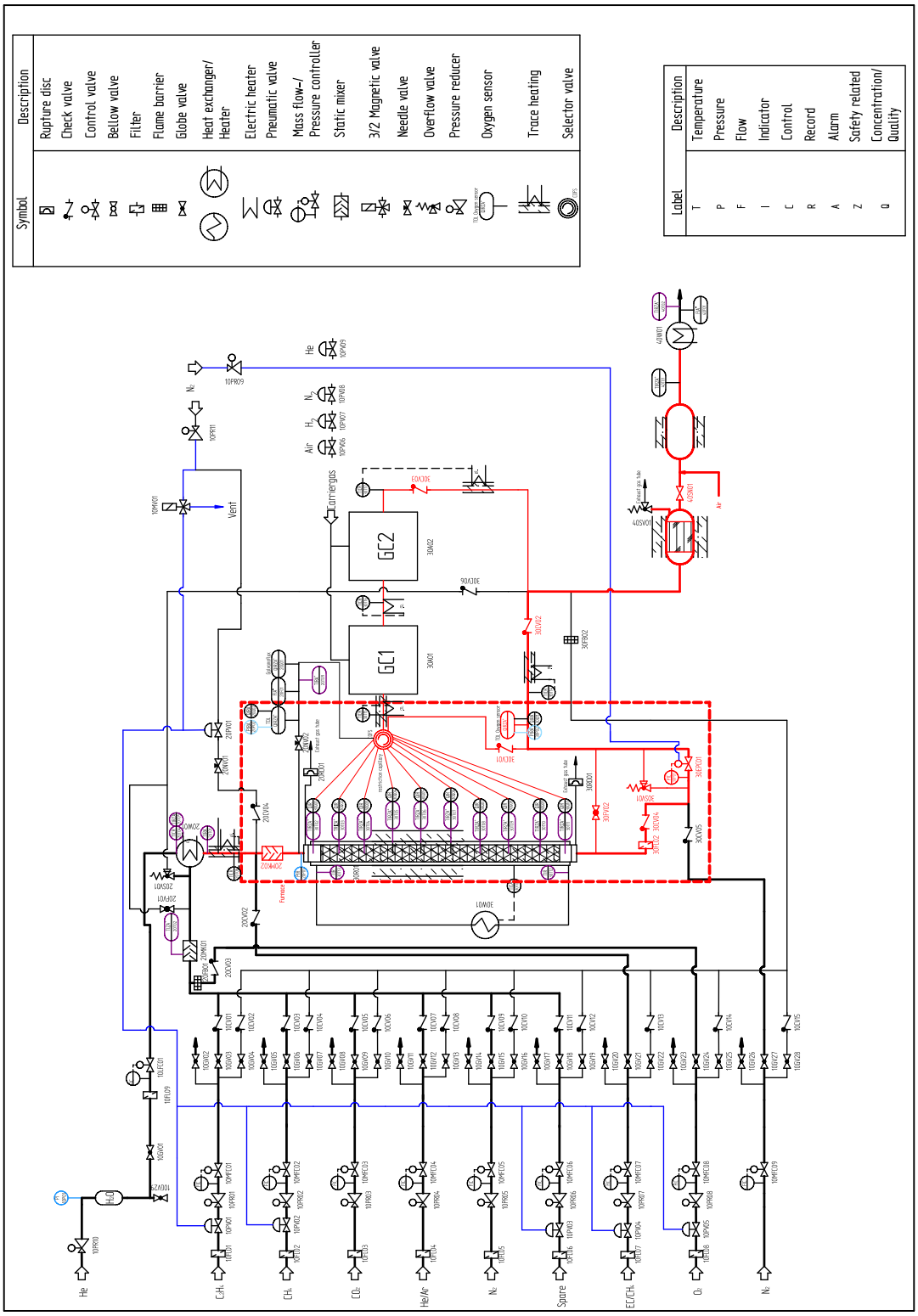

Figure 3.7: Flow diagram of the Pilot Scale Profile Reactor (PSPR) setup.

3.2.2 Gas Supply and Evaporator

The gas supply has been designed as "gas trains" for each species. A three-way outlet gas supply was chosen for ease of calibration and gas flow adjustment. Globe valves are used to direct the gas in the desired direction. It is possible to direct the gas to the reactor, to the bypass, or to the calibration line for flow rate calibration. Each gas type has its own pressure reducer to achieve a very precise pressure setting for the mass flow controller (MFC: Bronkhorst Prestige line). The species used were C_2H_4

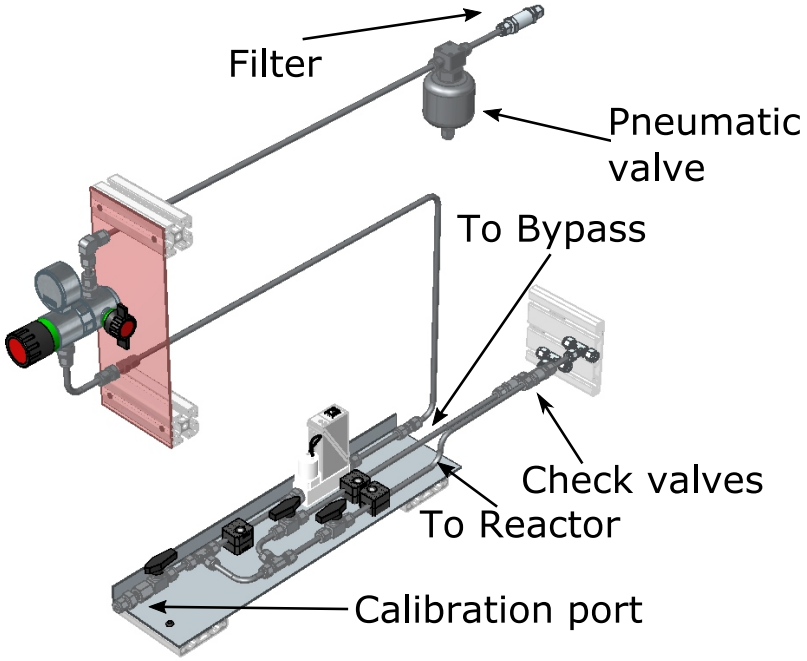

Figure 3.8: Sketch of the gas feed supply module design.

and O_2 as feed with N_2 as inert gas. Helium was used to pressurize the water and as a carrier gas for the GC. Also CO_2 to simulate industrial conditions and DCE mixed in N_2 as promoter gas. C_2H_6 and CH_4 could also be added to achieve precise industrial gas phase conditions.

To limit the local oxygen concentration for safety reasons, all gases were routed to the vaporizer, which consisted of a heated 1/2 inch tube filled with a packing of glass beads. Oxygen was added just before the evaporator inlet and mixed by the packing as it flowed through the evaporator. Water was dosed through a 1/16 inch tube that was in direct contact with the packing of the evaporator, similar to what was described in Chapter 3.1. After mixing the gas and evaporating the water, the gas feed was guided to the reactor through a heated tube to prevent condensation. Just before entering the reactor, the gas mixture passed through a T-piece where the promoter was added to the total gas flow. The gas feed was then mixed in a static filter consisiting of a sintered metal inlay, before entering the reactor.

3.2.3 Reactor Unit

The reactor tube is placed in an oven to keep all connections to and from the reactor heated to prevent e.g. EO from condensing or polymerizing. For the ethylene epoxidation it has to be taken into account that EO is a carcinogen and the lower explosive

limit starts at 2.6 vol-% in air at ambient conditions [10]. During the reaction there is always a risk of exceeding the lower explosive limit. Pre-experiments conducted by our project partner showed that in case of an explosion, the pressure of the reaction mixture would increase to 2.5 times the initial pressure. The upper pressure for the ethylene epoxidation reaction is approximately 17 bara, which means that the reactor must resist a maximum pressure of 51 bara in the worst case. To ensure this, even at higher temperatures, a reactor was designed using the AD-Regelwerk 2000 [134]. Flanges were taken as DN50 PN100. The nominal diameter of 50 was chosen for a better handling when filling the reactor with particles. A nominal pressure of 100 means that the reactor can be operated at 100 bar at ambient temperature. At higher temperatures (300 °C) the reaction pressure decreases to about 83 bar according to DIN EN 1092-1 [135]. The total length of the reactor was one meter with an inner diameter of 15 mm. Stainless steel (1.4571) was selected for the reactor tube and flange material. This steel material is already used in the industry for the epoxidation process. In addition, 1.4571 offers higher stress tolerance even at elevated temperatures. To provide the heat required for the reaction, a tube-in-tube design was chosen, with the inner tube where the reaction takes place, while the heat transfer medium flows through the outer tube. The heat was provided by a thermostat (Julabo HT-30-M1) with a silicone based heating oil. In case of an uncontrolled pressure increase in the reactor, two redundant safety devices were implemented. First, an overflow valve was installed in front of and behind the reactor. The overflow valve can release pressure until the adjusted pressure is reached before the valve closes again. This installation provides good safety for small pressure increases and allows the reactor to continue operating when the pressure is readjusted. The second installation, the rupture disc, is irreversible and focuses on rapid pressure relief. The rupture disc ensures a complete release of the reactor gas content to return the reactor to a safe condition. Two rupture discs (one in front and one behind the packing) have also been implemented in the event of a blockage in the reactor due to a polymerization reaction.

The reactor has been designed for use with either a static or a moving capillary. For the moving capillary, it is very important that the capillary is perpendicular to the reactor flange. This ensures that the capillary moves in the reactor in an axial position in the center of the bed. For this purpose, a tripod has been designed, which provides the possibility of a safe reactor attachment with simultaneously high flexibility of angle adjustment to keep the capillary perpendicular to the reactor flange, as can be seen in the overview of the designed setup in Figure 3.11. As a first step, static sampling was implemented using 10 stainless steel capillaries of 400 µm outer diameter, mounted at different heights in the center of the packed bed (Figure 3.9). All sampling lines must be continuously purged to avoid EO decomposition or polymerization. Each position could be addressed separately by a selector valve, which directed the sample to the GC while all other gas samples were guided to the combustion unit. In the center of the reactor was a 1/8 inch tube liner, which was also used to mount the capillaries. The capillaries were arranged in the circumference of the liner to hold them in place. Inside the liner 16 type-K thermocouples with a diameter of 250 µm were placed. To obtain a spatial temperature profile, the thermocouples were placed equidistantly inside the liner in axial direction.

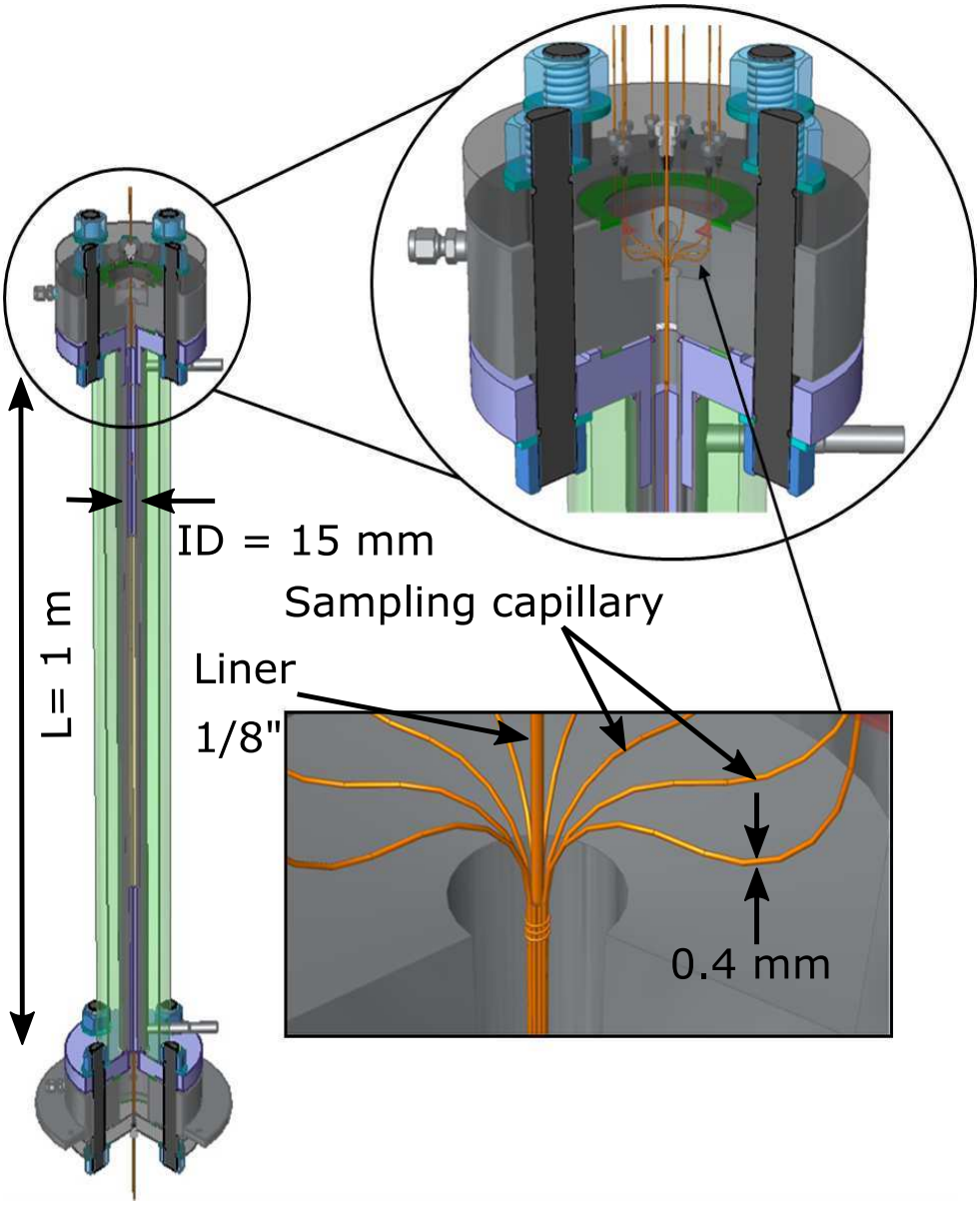

Figure 3.9: Sketch of the PSPR with arranged capillaries to measure spatial species profiles.

Sample volumetric flow rates were adjusted by needle valves located inside the furnace. The steel capillaries were connected to the needle valves through the top flange, which contained 10 threaded holes. Valco screws with polyimide graphite liners and 1/16 inch sealing cones were used to seal the holes from the outside atmosphere.

3.2.4 Combustion Unit

Before the product gas enters the building's exhaust system, it is burned in a combustion unit (Figure 3.10). In this unit, the product gas first enters a buffer vessel to prevent too much gas from entering the combustor in the event of an emergency shutdown. During a critical emergency, the reactor is depressurized and the entire reactor content enters the combustion unit.

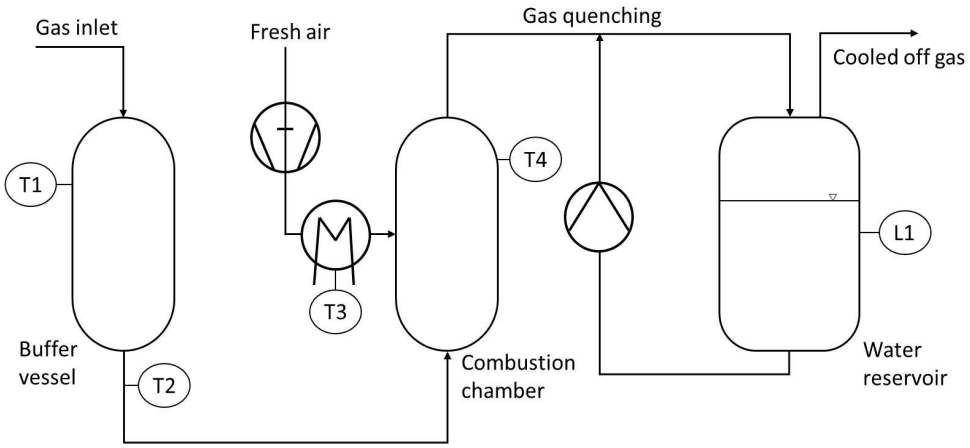

Figure 3.10: Schematic drawing of the combustion unit.

After the buffer tank, the product gas enters the combustion chamber where 850 °C hot air is injected to homogeneously oxidize all organic matter. The hot flue gas is then cooled by quenching with finely dispersed water before being sent to the in-house air treatment. The combustion unit has been purchased from the company I-TPT e.K.

3.2.5 Process Control

Since the ethylene epoxidation reaction was planned to run 24 hours a day, 7 days a week, an automated process control system was designed. The process control allows unattended measurement of the reaction. In the event of an emergency, the reactor process control system takes over and puts the setup in a safe state. Five different system levels were introduced:

1. Green level: everything is working without any malfunction, process is save.
2. Blue level: non-critical malfunction e.g. open doors of the fume hood or a by-passed process control.
3. Orange level: critical malfunction which releases the reactor pressure, cuts off the gas supply and purges the reactor with nitrogen. This level can be triggered by several relays implemented in the process control system, e.g. temperature overshoot, fume hood gas detector alarm, and too high or too low inlet oxygen concentration, which are continuously monitored by the TDL GPro 500 purchased from Mettler Toledo. This instrument spectroscopically measures the oxygen concentration in the gas mixture with one second resolution. If the inlet oxygen concentration exceeds 8 vol-% or the outlet oxygen concentration drops below 3 vol-%, the process control would activate the orange alarm.
4. Red level: electricity failure, this alert cuts off the power to the setup which means all heaters stop heating and the reactor is purged by nitrogen with a normally opened magnetic valve.
5. Red level + acustic signal: fire, same procedure as for the red level.

An orange alert or higher can only be reseted manually, which ensures that the reaction can only be restarted by a person intentionally. The process was controlled by a programmable logic controller (PLC) based on LabVIEW™.

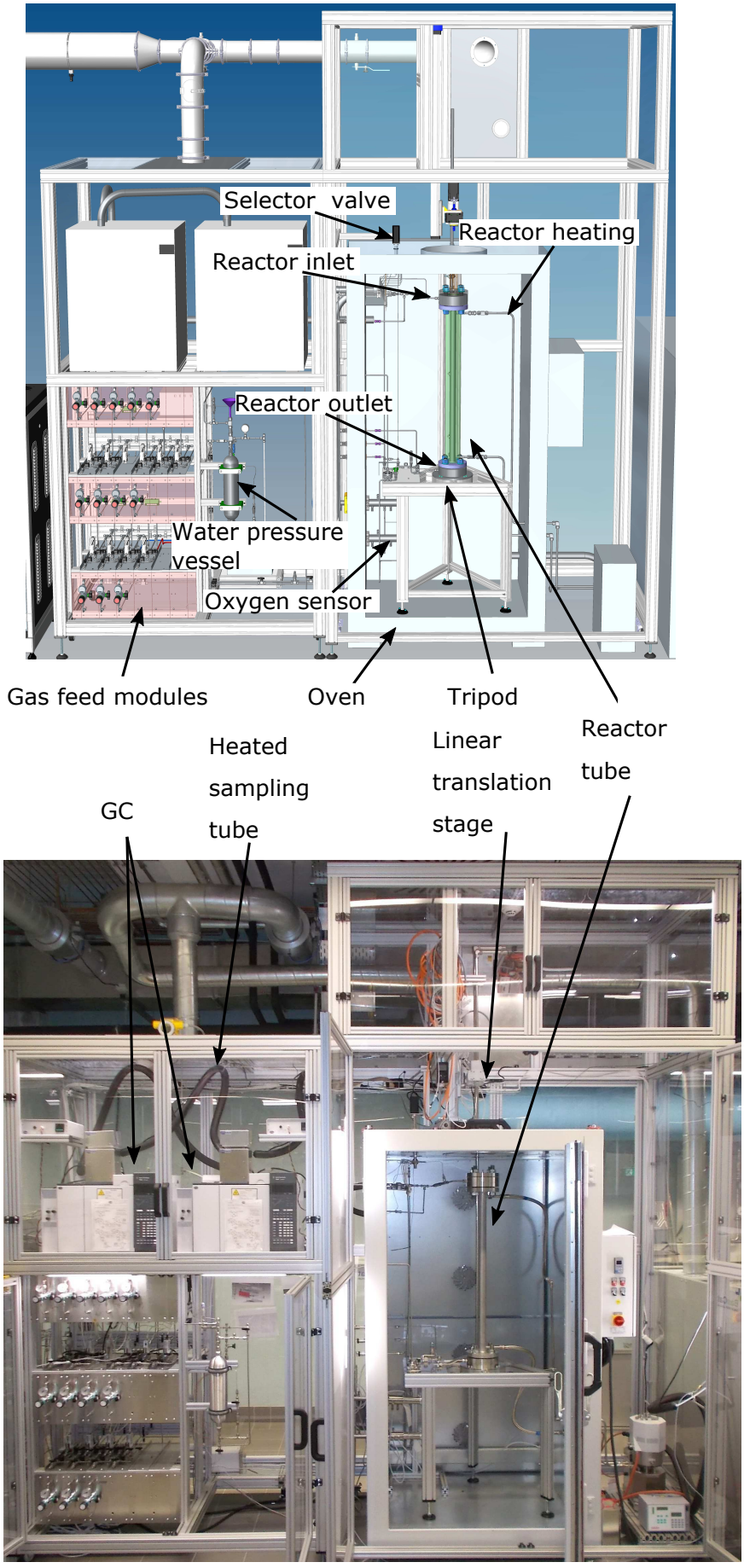

Figure 3.11: Pilot Scale Profile Reactor setup designed (top) and build (bottom).

Experimental 4

This chapter describes the experimental conditions for the measurements performed. The synthesis of the used catalyst is described in Chapter 4.1. The kinetic measurements with the differentially operated fixed-bed reactor and the Compact Profile Reactor are described in Chapter 4.2. Experimental conditions for profile measurements in the Pilot Scale Profile Reactor are presented in Chapter 4.3.

4.1 Catalyst

4.1.1 Catalyst Synthesis

The employed catalyst was provided by BASF SE and manufactured according to the patent WO2019/154832 [136]. Silver oxalate ethylenediamine complex solution was prepared according to example 3.1 of patent WO2019/154832. Amount of KOH solution was adjusted to yield a target K-concentration of 160 ppm. Complex solution had an Ag-content of 29.4 wt-% and density of 1.532 g/mL. A commercially available $\alpha-Al_2O_3$ support with BET-surface area of 0.8 m^2/g and a water uptake of 0.44 mL/g was obtained from EXACER s.r.l. The supported $Ag/\alpha-Al_2O_3$ catalyst was prepared according to example 3.2 of WO2019/154832. An amount of Ag complex solution was adjusted to yield an Ag-content of 14.5 wt-% in the calcined catalyst. The impregnated support was thermally treated for 12 min at 290 °C under 23 m^3/h nitrogen flow in an calcination oven. The typical shape of such catalysts are hollow cylinders, for the use in this work the cylinders were crushed and sieved to obtain split particles to be utilized in the applied reactors.

4.1.2 Catalyst Activation

Before starting a measurement, the catalyst was deaminated under a nitrogen flow with a GHSV of 4200 h^{-1} and a heating ramp of 10 K per hour from room temperature to 210 °C at atmospheric pressure. The experimental steps are as follows: after purging overnight with nitrogen, the reaction was started by pressurizing to 17 bara with no O_2 in the gas phase. Once the reaction pressure was reached, oxygen was added to the reaction mixture, and the reaction was run at a GHSV of 4900 h^{-1} and 240 °C for 100 h on stream with 25 vol-% of C_2H_4 and 4 vol-% of O_2. The other species were kept at standard concentrations according to Table 4.2. This catalyst startup procedure was applied in all experiments. After the equilibration time of 100 h on stream, the first profile measurement was started which took 56 h in total. When this first profile measurement was completed, a second profile measurement was started immediately, which took another 56 h. Both profile measurements were compared. If the difference of the profiles was within error bars, we concluded that steady state was reached.

4.2 Kinetic Measurements

4.2.1 Differential Reactor

Initial reaction rate measurements in a differentially operated fixed-bed reactor were made in the kinetic test reactor described in Chapter 3.1. Therefore, 150 mg of the $Ag/\alpha - Al_2O_3$ sieve fraction of $200 - 400$ µm was mixed with 850 mg of Al_2O_3 support of the same sieve fraction and packed into a 1/4" tube. A pre-pack of carrier material filled the tube. The pre-packing is designed to establish the velocity field before the reaction mixture enters the catalyst bed. The sieve fraction ensures that even in the worst case, i.e. when the coarse particles are the largest fraction, the plug flow criterion is met ($d_t/d_p = 4.57$ mm/0.4 mm > 10) [65]. Temperature was measured with a K-type thermocouple in direct contact with the packing. The GHSV of 66.000 h^{-1} was set to ensure measurements free of film transport limitations due to the reduced boundary layer (see Chapter 2.1.2). In order to quantify the reaction orders of the various species in the feed, initial rate measurements were conducted by limiting the conversion of oxygen to less than 5 % [5]. Table 4.1 lists the feed species and the ranges in which their concentrations were varied to determine their impact on the initial reaction rates. Additionally, measurements at a set of standard concentrations (Table 4.2) were performed in between the concentration variations of each single species to account for activity losses. In each concentration variation, the total volumetric flow rate was kept constant. After the catalyst activation, as described

Table 4.1: Operating Parameters Used for the Kinetic Measurements.

Parameter	Value/Range	Unit
C_2H_4	25 – 40	vol-%
O_2	3 – 8	vol-%
H_2O	0.15 – 1.5	vol-%
CO_2	1 – 3	vol-%
N_2	balance	vol-%
DCE	1.25 – 2.5	ppm
Temperature	220	°C
Pressure	17	bara
GHSV	66000	h^{-1}
O_2 Conversion	< 5	%

in Chapter 4.1.2, the kinetic measurements were started with standard concentration conditions at 220 °C and a GHSV of 66000 h^{-1}. Each species was varied separately while all other species were held constant at their standard value. The concentrations of CO_2 and H_2O were chosen to mimic the industrial application of the measurements. In industry, residues of H_2O are present in the feed as a result of the gas scrubbing process to extract EO from the product gas and the recycling of C_2H_4. The activation energies for both reactions were determined by measuring the formation of EO and CO_2 under standard conditions while varying the reaction temperature. By evaluating the Arrhenius plot, i.e. the slope of the natural logarithm of the reaction rate versus the reciprocal of the temperature, the activation energy can be determined. Two experiments were performed, each with a different DCE concentration. The first run was at the standard concentration listed in Table 4.2, for the second run the DCE

Table 4.2: Standard Species Concentrations for the investigation of the epoxidation reaction.

Parameter	Value	Unit
C_2H_4	35	vol-%
O_2	7	vol-%
H_2O	0.15	vol-%
CO_2	1	vol-%
N_2	balance	vol-%
DCE	1.25	ppm
Impurity (hydrocarbons, e. g. C_2H_6)	500	ppm

concentration was doubled to 2.5 ppm.

To automate the measurements, a 24/7 measurement was implemented with automatic sampling that could adjust the gas flow, switch the selector valve between measurements, and trigger the GC to analyze the product stream. To account for activity loss, standard gas composition measurements were performed between each measurement. Each condition was measured at least three times to increase the accuracy of the measurements by averaging the measured values.

4.2.2 Compact Profile Reactor

Setup

The CPR was developed by Reacnostics GmbH to measure spatial profiles in a compact reactor setup that fits under a Raman microscope. The CPR can be used to measure in-situ, concentration and temperature profiles as well as under operando conditions, e.g. by measuring Raman profiles simultaneously. In this work, the CPR was used to measure concentration and temperature profiles on a laboratory scale. The CPR offers a new approach compared to conventional reactor types such as "normal" fixed-bed reactors. Reactions can be studied in small reactors (6 mm diameter) and still obtain concentration and temperature profiles that can be measured over a length of 60 mm, thus identifying intermediates or gradients that are normally not visible. The reactor tube can be either a glass or stainless steel tube placed in a brass block which is heated up to 550 °C by heating cartridges. The brass block is mounted on a movable carriage with micrometer step resolution, whose speed and direction of movement can be programmed. Moving the carriage moves the entire reactor tube. Inside the reactor, in the center of the bed, a capillary can be mounted with an orifice from 50 to 400 µm, depending on the reaction pressure. This capillary is mounted statically. By moving the reactor and keeping the capillary static, spatial concentrations can be measured. By placing a thermocouple inside the capillary, temperature measurements can be made simultaneously. Figure 4.1 shows the CPR used with the reactor tube mounted and the sampling capillary inside the reactor. More information about the CPR setup can be found elsewhere [17].

Due to the unique configuration of the small reactor, even when using a glass tube reactor (1 mm wall thickness), the reaction pressure can be adjusted up to 20 barg. To keep the room around the reactor hot to avoid condensation of e.g. water, brass heating blocks can be heated by heating cartridges and the heat is distributed by

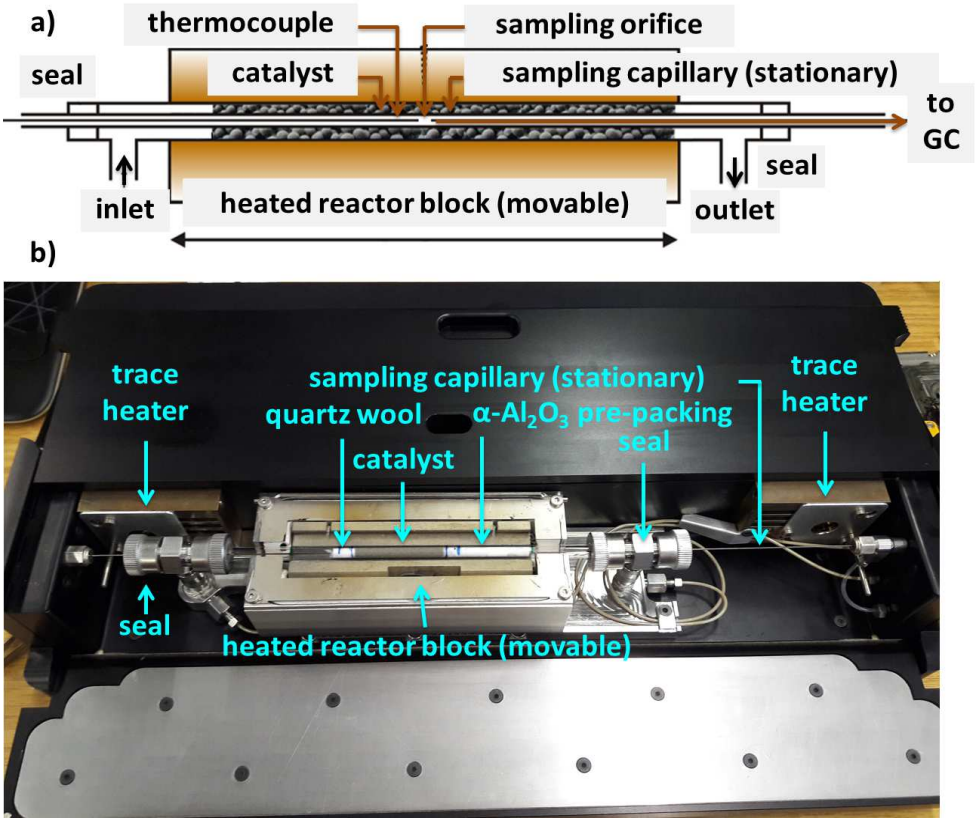

Figure 4.1: Compact Profile Reactor (CPR) used to investigate the reaction network of ethylene oxide synthesis on a Ag-catalyst and the mechanism of chlorine inhibition. a) Working principle. b) Annotated photograph of the open reactor.

two propellers mounted in the brass blocks. The temperature in the space around the reactor is measured by PT-100 elements and controlled to the measured value. Depending on the reaction conditions, spatial profiles can be obtained either by using a vacuum system, e.g. a mass spectrometer, or by gas chromatography. When measuring at a reaction pressure higher than ambient, samples are taken by the pressure gradient from the reactor to the analyzer. By controlling the pressure drop, e.g. via a needle valve, the amount of sample gas can be adjusted to ensure that less than 5 % of the total volumetric flow is used for sampling, thus minimizing perturbation of the flow field.

Due to the small size of the CPR, reaction conditions can be controlled very precisely, e.g. isothermal measurements. This allows not only profile measurements of reaction conditions but also kinetic measurements. By measuring the profiles and obtaining concentration and temperature data, all the information for a kinetic data regression is obtained by fitting the measured profile over the entire reactor length.

Profile measurements

For the profile measurements in the CPR, the standard reaction conditions tabulated in Table 4.2 in Chapter 4.2.1 were used, unless a different value is explicitly mentioned. The reactor tube (18 mm length and 6 mm outer diameter) was filled with a sieve fraction of $200-400$ µm of Ag/$\alpha-$alumina catalyst. The length of the active catalyst bed was always less than 60 mm, which represents the maximum movement range of

the reactor slider. The reactor tube was filled with catalyst in such a way that the capillary was completely surrounded by catalyst particles to avoid bypassing the feed stream and to obtain reliable concentrations at the sampling point. In front of the catalyst bed, an inert packing was filled into the reactor to heat the gas stream prior to starting the reaction and to establish a flow profile and good mixing of all reactants. Behind the catalyst packing, a plug of fused silica was formed to hold the catalyst in place during the measurement. Prior to the start of the measurement, the capillary sample volume was measured with a flow meter to accurately adjust the sample volume to keep the total sample volume below 5 % of the total volumetric flow. After the same start-up procedure as described in Chapter 4.2.1, the profile measurement was started.

Each sampling position was measured at least three times before the next sampling position was set. The measurement was equidistant between the sampling positions with a distance of 2000 µm. Concentrations were evaluated quantitatively by gas chromatography. To ensure that all probed species were measured in the GC, all tubes to the GC and the sampling valves were heated. Since the reaction pressure was 17 bara, the sample volume was controlled by a micrometer needle valve, which is commonly used in GCs to control the volumetric flow of carrier gases. To avoid condensation inside the micrometer needle valve, the valve was placed in a heated box. Profile measurements were performed at two different space times, the standard GHSV of 4750 h^{-1} and 9500 h^{-1}. In addition, the effect of DCE on the profiles was tested by applying different concentrations including no DCE cofeeding. The process conditions for the profile measurements are summarized in Table 4.3.

Table 4.3: Operating Parameters Used for the Profile Measurements with the CPR.

GHSV [h^{-1}]	Temperature [°C]	DCE [ppm]
9500	225	2.5
9500	225	1.25
4750	200	1.25
4750	210	1.25
4750	225	1.25
4750	225	0

4.2.3 Analytics

The sample gas from the differential reactor and the CPR measurements was analyzed on an Agilent 7890B gas chromatograph. The sample inlet was heated to 150 °C by the sampling valve located in a valve box on top of the GC housing. To avoid condensation or polymerization reactions due to static gas volume, the sample loop was always purged with the reaction gas mixture. The analysis was started by loop volume injection and the gas mixture was first passed through the HaysepQ column, which retains long chain hydrocarbons as shown in Figure 4.2. After 2 minutes of flow time, the HaysepQ was backflushed by switching the changeover valve. The next steps have to be explained separately because the measurement was done with two different detectors. The loop volume of 250 µL was passed through the PlotQ column to the molsieve and finally to the thermal conductivity detector (TCD). Permanent gases such as argon, nitrogen and oxygen cannot be separated in the PlotQ, but they leave

the column as the first species. Therefore, the molsieve was in line at the beginning of the measurement, and after about 4 minutes the molsieve was switched to a dead-end position to prevent CO_2 or H_2O from being deposited on the molsieve. The PlotQ was used to separate carbon dioxide, ethylene and water. When the water peak was detected on the TCD, the molsieve was switched to the TCD to analyze the separated peaks of oxygen, nitrogen, and methane. The 1000 µL loop was diluted to 10:1 by the split before the sample gas was passed to the PlotU column where methane, ethylene, and ethylene oxide were retained. After passing through the PlotU column, the gas mixture was passed directly to the flame ionization detector (FID). The Rtx Wax column was not required for this analysis and was bypassed.

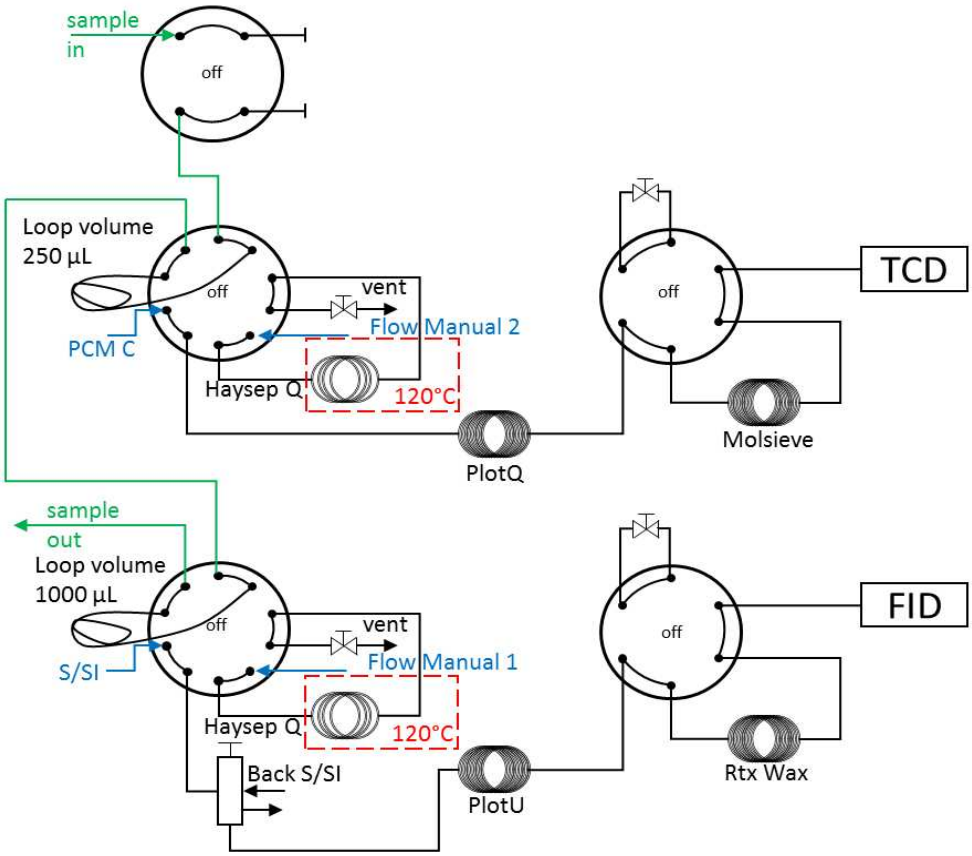

Figure 4.2: GC switching valves and columns arrangement to analyze the gas sample composition for the profile measurements.

4.3 Pilot Scale Profile Reactor

4.3.1 Measurement Conditions

Prior to the experiments, the reactor was filled with the crushed $Ag/\alpha-Al_2O_3$ catalyst of a sieve fraction of $500-900\mu m$. Therefore, the liner containing the thermocouples was placed in the center of the reaction tube. Sampling capillaries were placed around the liner for later sampling and catalyst was added around the liner to fill the reactor tube. After filling the catalyst and checking for leaks, the start-up procedure described in Chapter 4.2.1 was started.

Due to the highly exothermic reaction and the higher amount of catalyst, the

reaction temperature was lowered compared to the profile measurements with the CPR (Chapter 4.2.2). The set of measured profiles is given in Table 4.4. Tabulated are the parameters that were varied, the remaining parameters were kept at standard conditions tabulated in Table 4.2 in Chapter 4.2.1.

Table 4.4: Conditions for Spatial Profile Measurements.

Experiment No.	Temperature [°C]	DCE [ppm]	CO_2 [vol-%]
1	180	1.5	1
2	180	0.75	1
3	180	0	1
4	190	1.5	1
5	190	1.5	0
6	194	1.5	1
7	194	3	1
8	200	3	1

The experiments were started with 180 °C to avoid runaway conditions while the catalyst is still very active. DCE was adjusted at 1.5 ppm and dosed continuously to the feed.

The capillaries were evenly distributed in the axial direction so that the first sample was taken in front of the active catalyst bed, eight probe positions were taken inside the catalyst bed, and the last sample was taken behind the bed, as shown in Figure 4.3. For temperature measurement, the 16 thermocouples were distributed such that the first measurement position was in front of the bed and the last one was behind the bed, while the remaining 14 positions were distributed equidistantly in the axial direction within the active catalyst packing of 500 mm length.

4.3.2 Analytics

To speed up the profile measurements, two GCs were used in parallel, connected in such manner that the selected sample flow passes through both GCs. Since the sampling position was controlled by a selector valve, the profile measurement was automated. The measurement algorithm was as follows: the desired sampling position was selected, then the GC measurement was started by an external trigger. The second GC was also triggered if a measurement at the same position with the second GC was also desired. Another option was to change the sample position and measure with the second GC at a different position to speed up the profile measurement. This measurement algorithm was performed in a loop to obtain multiple profiles under the same conditions to reduce measurement errors. For quantitative analysis of the gas samples, each GC was equipped with two detectors, a thermal conductivity detector (TCD) and a flame ionization detector (FID). Multiple columns with a complex switching procedure were required to separate and analyze the sample gas. The GC analysis was performed with the same procedure as described in Chapter 4.2.3.

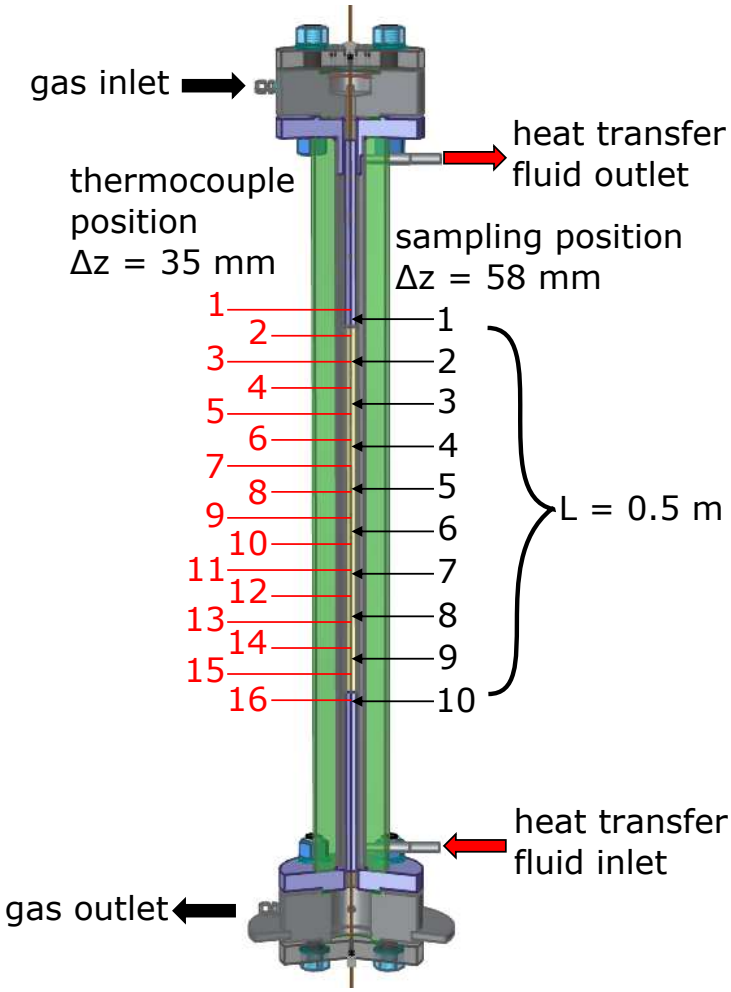

Figure 4.3: Pilot Scale Profile Reactor (PSPR) for spatially resolved temperature measurements and species sampling. Temperature measurement points (16) are indicated in red, the species sampling points (10) in black.

Results and Discussion 5

This chapter presents the results of the kinetic and profile measurements performed. The results for the differential fixed-bed measurements are described in Chapter 5.1. The results for the profile measurements and parameter regression using the profiles measured in the Compact Profile Reactor are given in Chapter 5.2. The kinetic validation was performed using the profiles measured in the Pilot Scale Profile Reactor described in Chapter 5.3.2.

5.1 Differential Reactor

5.1.1 Heat and Mass Transfer Gradients

In order to perform limitation-free kinetic measurements, external, internal, and bed gradients should be small enough to be negligible. Therefore, the analytical methods introduced in Chapter 2.1.2 were applied.

External Gradients

Equation 2.11 was evaluated to determine if external gradients were present. Therefore, the observable variables were determined experimentally at the standard concentration conditions listed in Table 4.2. The result of the criterion for the absence of extraparticle gradients is given by eq. 5.1 using the parameters listed in Table 5.1. The Arrhenius number based on the bulk fluid temperature was calculated using the apparent activation energy for the selective reaction listed in Table 5.4. The temperature and pressure as well as the GHSV used are listed in Table 4.1. The mass and heat-transfer coefficients k_f were calculated using the Sherwood and Nusselt numbers listed in Table 2.1 for a $Re_p = 1.8$. For the molecular diffusion coefficient, the binary diffusion coefficient was calculated according to eq. 2.17 for ethylene in nitrogen, since its amount exceeds 90 % of the total gas volume. The conductivity of the fluid mixture was determined according to the mixing rule proposed by Wassiljewa [137] with the modification of Mason and Saxena [138]. The bulk concentration was determined via the ideal gas law and for the surface to volume ratio of the particle, the largest possible particle was taken, i. e. 400 µm, to test for the worst case and it was assumed that the particles are spherical. The analytical test shows that the external limitation can be neglected in the kinetic measurements.

$$|\gamma_b \cdot \beta_e \cdot Ca| = |20.177 \cdot 0.294 \cdot 0.003| = 0.018 < 0.05 \tag{5.1}$$

Part of this work was published in: Berg, V., Geske, M., Korup, O., Schmidt, M., Rosowski, F., Karpov, A., Kraemer, M. and Horn, R., Selective Oxidation of Ethylene to Ethylene Oxide on Silver Catalysts at Industrial Conditions: Reactor Profiles, Kinetics and Chlorine Inhibition. Industrial & Engineering Chemistry Research 63 (9) (2024) 3891-3909 https://doi.org/10.1021/acs.iecr.3c04345

Table 5.1: Parameter for External Limitation Criteria.

Parameter	Value	Unit
ΔH_R	-105000	$J \cdot mol^{-1}$
k_f	$7.2 \cdot 10^{-4}$	$m \cdot s^{-1}$
h	15.3	$W \cdot m^{-2} \cdot K^{-1}$
c_b	29.03	$mol \cdot m^{-3}$
$r_{v,obs}$	0.93	$mol \cdot m^{-3} \cdot s^{-1}$
a'	15000	m^{-1}
$D_{C_2H_4-N_2}$	$2.29 \cdot 10^{-6}$	$m^2 \cdot s^{-1}$
λ_f	0.05	$W \cdot m^{-1} \cdot K^{-1}$

Internal Gradients

The catalyst used, described in Chapter 4.1, is supported on a low surface area alumina, indicating only large pores. Large pores are required for the ethylene epoxidation reaction to transport EO out of the catalyst and avoid subsequent oxidation. To test whether internal limitation might be present, eq. 2.29 was evaluated using additional parameters listed in Table 5.2: The value for the effective thermal conductivity of the

Table 5.2: Parameter for Internal Limitation Criteria.

Parameter	Value	Unit
T_s	493.43	K
D_{eff}	$1.20 \cdot 10^{-7}$	$m^2 \cdot s^{-1}$
$\lambda_{p,eff}$	0.1	$W \cdot m^{-1} \cdot K^{-1}$
c_s	28.94	$mol \cdot m^{-3}$

particle has been estimated. For porous materials in gaseous atmospheres, $\lambda_{p,eff}$ is in the range of 0.1 to 0.5 W/(m·K) [54]. To consider the worst case, the lower value was taken. The surface concentration c_s was calculated with eq. 2.6 and the surface temperature with eq. 2.9. Since the catalyst had only large pores, the effective diffusion coefficient was calculated using the binary diffusion coefficient from Table 5.1. Particle porosity and tortuosity values were not available, so the effective diffusion coefficient was calculated according to eq. 2.23 considering the worst case with the lower value. The evaluation of eq. 2.29 gave the following result:

$$\left|\gamma_s \cdot \beta_i \cdot \eta_i \phi^2\right| = \left|20.159 \cdot 0.739 \cdot 10^{-2} \cdot 0.119 \cdot 10^{-2}\right| = 0.178 \cdot 10^{-3} < 0.1 \qquad (5.2)$$

The result of eq. 5.2 shows that the kinetic measurements were free of internal limitations.

Catalyst Bed Gradients

As mentioned above, the most likely limitation to kinetic measurements is the temperature limitation within the catalyst bed. To overcome this limitation, the catalyst was diluted with its support (15 wt-% catalyst with 85 wt-% support) and the ratio of particle size to tube size was smaller than 10. To ensure limitation free measurements,

Table 5.3: Parameter for the Catalyst Bed Limitation Criteria.

Parameter	Value	Unit
T_w	493	K
$\lambda_{bed,eff}$	0.08	$W \cdot m^{-1} \cdot K^{-1}$
d_t	4.57	mm
$r_{V,obs}$	$8.4{\cdot}10^{-2}$	$mol \cdot m^{-3}{\cdot}s$
$Bi_{h,w}$	1.52	-

the eq. 2.30 was checked with the parameters in Table 5.3: The Biot number was calculated according to the eq. 2.32 with the wall heat-transfer coefficient determined by the wall Nusselt number from the correlation of Tsotsas [63]. The effective bed heat conductivity was calculated from the correlation of Neubronner et al. [64].

$$|\gamma_w \cdot \beta_w \cdot B_w| = \left|20.177 \cdot 0.120 \cdot 10^{-2} \cdot 0.183\right| = 0.44 \cdot 10^{-2} < 0.05 \qquad (5.3)$$

From the result of eq. 5.3 it can be concluded that temperature gradients within the catalyst bed can be neglected for kinetic measurements, thus the kinetic measurements were free of limitations.

5.1.2 Reaction Order

The results of the initial rate measurements at C_2H_4 partial pressure variation are shown in Figure 5.1. C_2H_4 had a negligible effect on the rates of the selective and unselective reaction in the tested concentration range, which is not surprising, taking the large excess of ethylene into account ($C_2H_4/O_2 = 5$). C_2H_4 was considered in the derived rate law, but due to the large excess of ethylene in the reaction mixture, a variation of up to 50 % of the initial concentration had only a small effect on the reaction rate. Similar results for C_2H_4 were reported by Cant and Hall [73]. The dependence of O_2 on the reaction rate is shown in Figure 5.2. O_2 is the limiting species for the investigated reaction conditions with a standard O_2 concentration of 7 vol-%. The reaction rate increases with increasing O_2 partial pressure for both the selective EO formation and the unselective CO_2 formation. For both reactions, the reaction order is about 1. The kinetic dependence of the O_2 partial pressure implies that a species derived from molecular oxygen is involved in the kinetically relevant step. These results are in agreement with the literature published by Chen et al. [13]. In addition, Chen et al. reported an increase in oxygen reaction order with increasing chlorine cofeeding, indicating that chlorine reduces oxygen coverage on the catalyst surface and enhances oxygen desorption, respectively. The CO_2 partial pressure dependence of both rates is shown in Figure 5.3. With increasing CO_2 partial pressure, both rates decrease slightly, resulting in a slightly negative reaction order. This finding indicates that the active sites responsible for both the selective and the unselective reactions are occupied by CO_2. For variations of the H_2O partial pressure, reaction orders of -0.08 and -0.06 were found for the selective and the unselective reaction respectively. H_2O had almost no effect on the reaction rate and was therefore neglected in the rate law. Similar results were reported by Metcalf and Harriott [101] who also measured reaction orders in a differential reactor. In contrast to CO_2 and H_2O, DCE had a strong impact on the reaction rates as can be seen in Figure 5.5. Even a slight increase in DCE concentration resulted in strongly decreasing the reaction rates of both the selective and unselective reactions with a negative reaction order of (-0.97) for EO

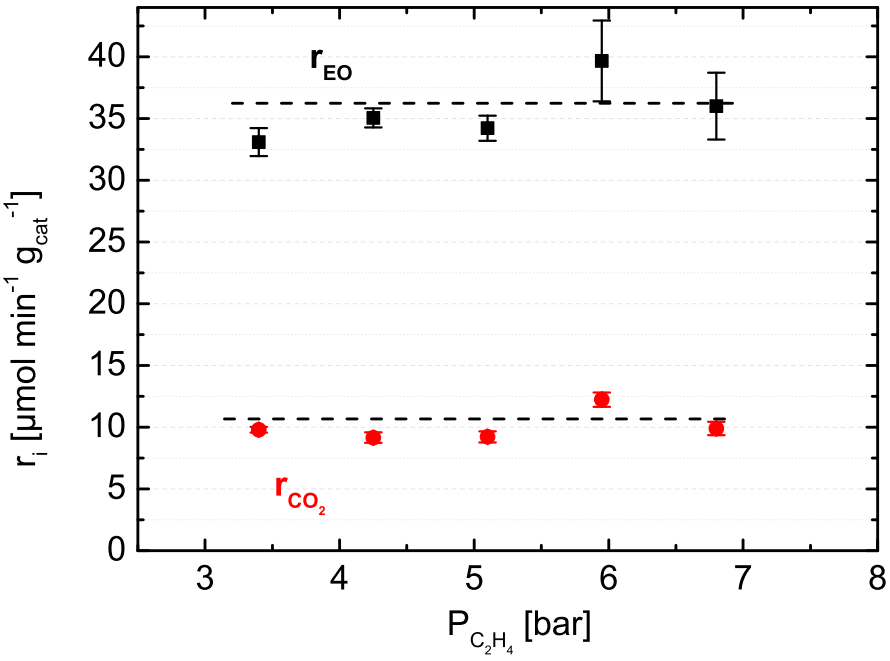

Figure 5.1: Reaction rate for selective (r_{EO}) and unselective oxidation (r_{CO_2}) vs. C_2H_4 partial pressure at 225 °C and 17 bara with 1.25 ppm DCE.

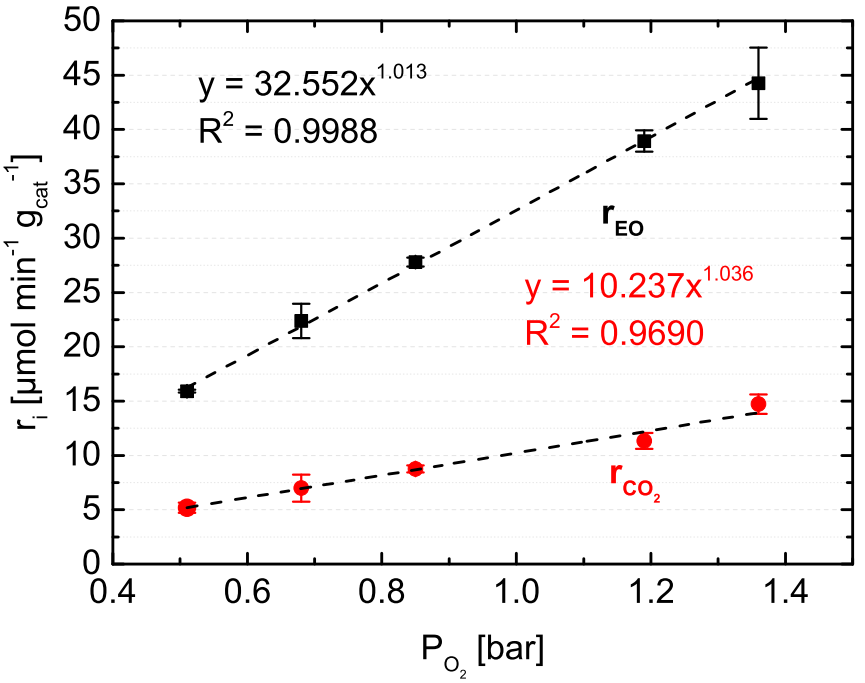

Figure 5.2: Reaction rate for selective (r_{EO}) and unselective oxidation (r_{CO_2}) vs. O_2 partial pressure at 225 °C and 17 bara with 1.25 ppm DCE.

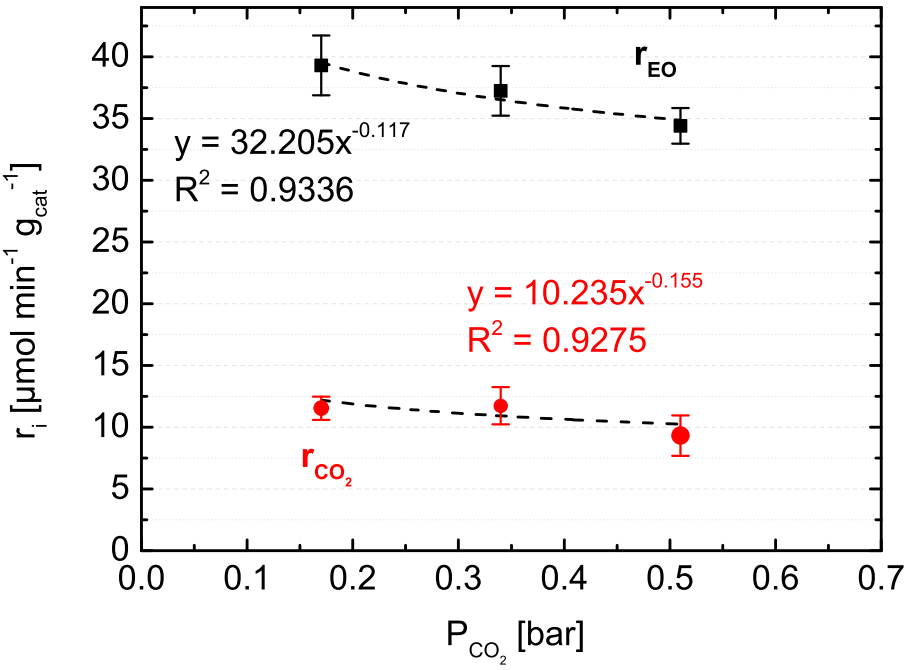

Figure 5.3: Reaction rate for selective (r_{EO}) and unselective oxidation (r_{CO_2}) vs. CO_2 partial pressure at 225 °C and 17 bara with 1.25 ppm DCE.

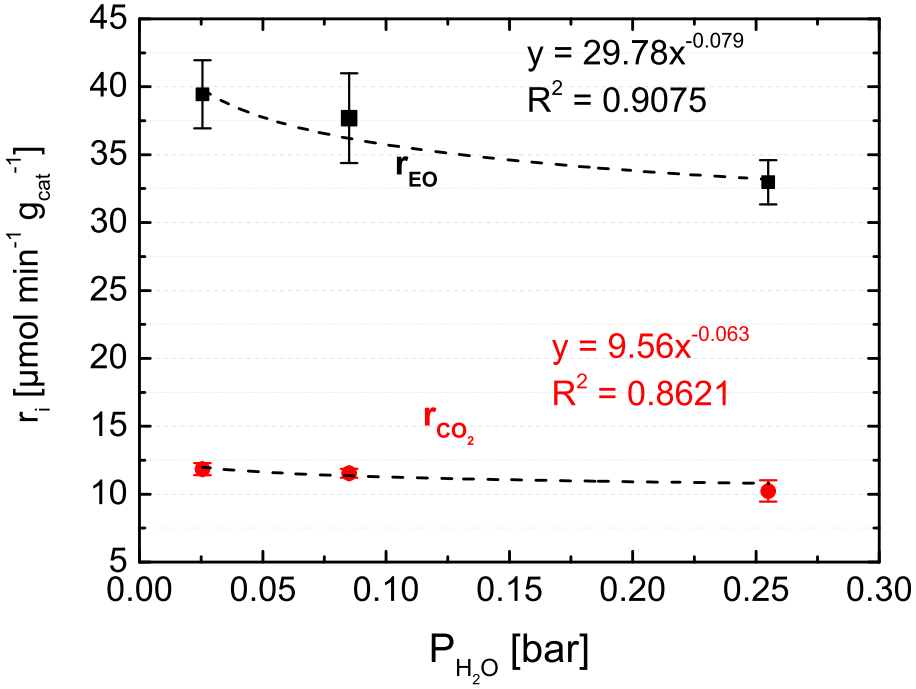

Figure 5.4: Reaction rate for selective (r_{EO}) and unselective oxidation (r_{CO_2}) vs. H_2O partial pressure at 225 °C and 17 bara with 1.25 ppm DCE.

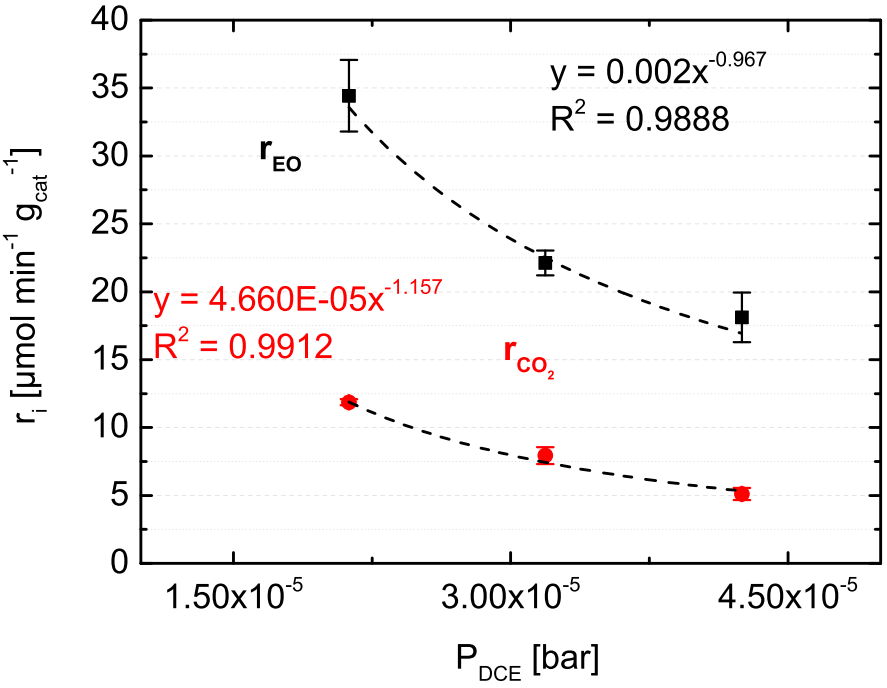

Figure 5.5: Reaction rate for selective (r_{EO}) and unselective oxidation (r_{CO_2}) vs. $C_2H_4Cl_2$ partial pressure at 225 °C and 17 bara.

formation and (−1.16) for CO_2 formation. With increasing DCE partial pressure, the catalyst activity decreases due to site blocking by chlorine [139]. In accordance with increasing selectivity to EO upon increasing DCE concentration, the rate decreases stronger for the unselective reaction, expressed by a more negative reaction order.

5.1.3 Activation Energy

To determine the activation energies for the selective epoxidation to EO and the unselective total combustion to CO_2 were derived from Arrhenius plots. Initial rate measurements were evaluated by plotting of the logarithmic selective and unselective reaction rate versus the reciprocal temperature.

Figure 5.6 shows the result for the standard DCE concentration of 1.25 ppm. The selective reaction shows an apparent activation energy of 82.7 kJ/mol compared to 88.2 kJ/mol for the unselective CO_2 formation. The activation energy for the selective reaction is lower than for the unselective reaction, which corresponds to results published by other authors [13, 140, 141]. The lower activation energy for the selective reaction leads to a high initial EO selectivity which was around 75 % in these measurements. The activation energy measurement results for a DCE concentration of 2.5 ppm are shown in Figure 5.7. With increasing DCE partial pressure, the apparent activation energy for EO formation (Ea_{EO}) increases slightly to 94.6 kJ/mol, whereas Ea_{CO_2} almost doubles to 160.5 kJ/mol. This relatively small increase of Ea_{EO} compared to Ea_{CO_2} indicates that chlorine promotion inhibits the unselective reaction much more than the selective reaction by increasing the energy barrier of CO_2 formation more than that of EO formation. An increase in activation energy with increasing partial pressure of the chlorine containing compound was already reported by Chen et al. [13], who performed measurements on a commercially promoted and supported

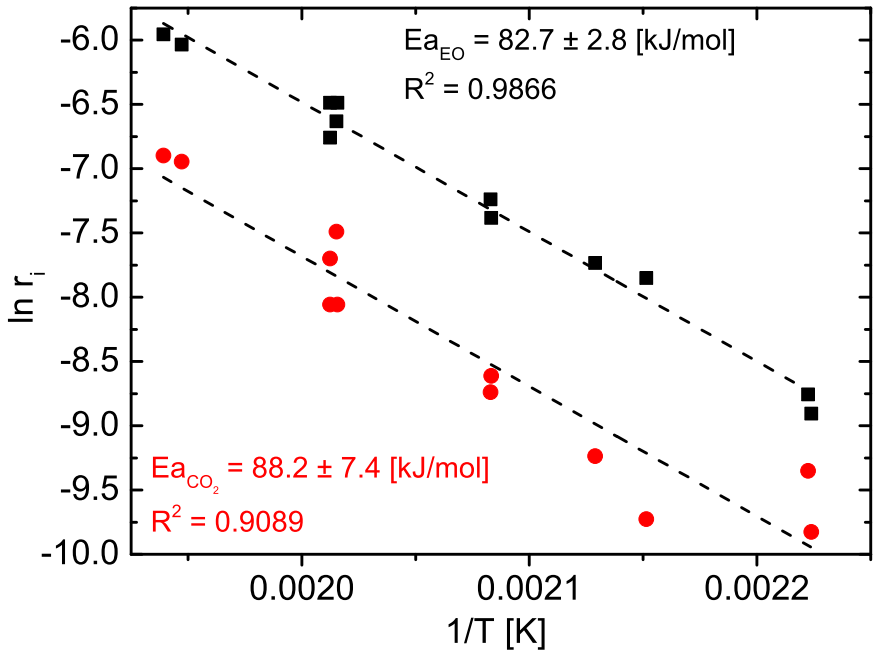

Figure 5.6: Arrhenius plot for initial reaction rates measured at GHSV = 66,000 h^{-1}, 17 bara pressure, and DCE concentration of 1.25 ppm under differential conditions.

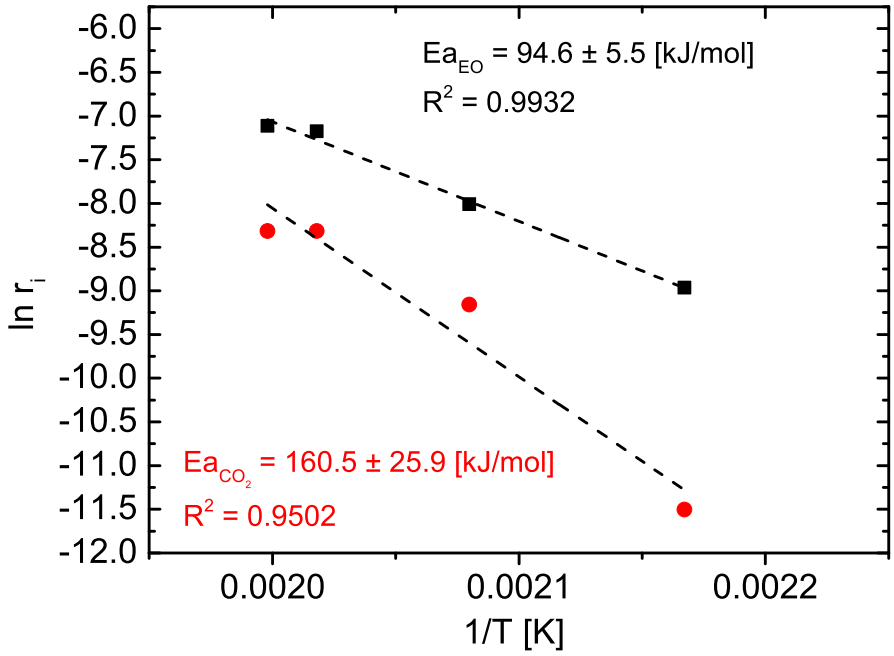

Figure 5.7: Arrhenius plot for initial reaction rates measured at GHSV = 66,000 h^{-1}, 17 bara pressure, and DCE concentration of 2.5 ppm under differential conditions.

silver catalyst. They obtained activation energies for both reactions of 212 kJ/mol resulting from high chlorine dosing. This high value indicated an overinhibition of the catalyst suppressing both reaction paths. Industrially, a compromise must be made between achieving an economically attractive conversion at a yet acceptable EO selectivity. This requires an extremely accurate control of the DCE inlet concentration at the ppm level and of the reactor temperature due to the sensitive dependence of ethylene conversion and EO selectivity on both parameters.

Table 5.4: Experimentally Determined Apparent Activation Energies for the Epoxidation and Total Combustion Reaction.

Temperature range [K]	Ea_{EO} [kJ/mol]	Ea_{CO_2} [kJ/mol]	DCE [ppm]
450 – 515	82.7 ± 2.8	88.2 ± 7.4	1.25
460 – 500	94.6 ± 5.5	160.5 ± 25.9	2.5

5.1.4 Rate Law Derivation

The rate laws were derived using a differentially operated fixed-bed reactor and a literature mechanism postulated by the group of Schlögl [18]. According to the extensive research published on the mechanism of ethylene epoxidation by Schlögl et al. [18, 142, 143], the catalyst shows a distinct dynamic behavior of defect formation by adsorbed oxygen, leading to metal reconstruction at mild temperature, which in turn affects the oxygen adsorbates. Depending on the state of the adsorbed oxygen, the ethylene oxidation is either selective or unselective, with electrophilic oxygen leading to ethylene oxide and nucleophilic oxygen to carbon dioxide [142]. Depending on the active site, the reaction produces EO either selectively on an Ag−O site with subsurface oxygen (AgO_{sub}) or unselectively CO_2 and H_2O on a nucleophilic oxygen atom adsorbed on an Ag step site (Ag_{step}). The relevant reaction steps are as follows [18]:

$$\mathrm{O_2} + Ag \rightleftharpoons Ag\mathrm{O_2}^* \tag{5.4a}$$

$$Ag\mathrm{O_2}^* + 2\ Ag_{step} \longrightarrow 2\ AgO^*_{nu} + Ag \tag{5.4b}$$

$$AgO^*_{nu} + Ag_{sub} \rightleftharpoons AgO_{sub} + Ag_{step} \tag{5.4c}$$

$$AgO^*_{nu} + AgO_{sub} \longrightarrow (AgO_{sub})O_{el} + Ag_{step} \tag{5.4d}$$

$$AgO_{sub} + \mathrm{C_2H_4} \rightleftharpoons (AgO_{sub})\mathrm{C_2H_4}^* \tag{5.4e}$$

$$(AgO_{sub})\mathrm{C_2H_4}^* + (AgO_{sub})O_{el} \xrightarrow{rds_{EO}} \tag{5.4f}$$
$$\mathrm{C_2H_4O}_{EO} + 2\ AgO_{sub}$$

$$(AgO_{sub})\mathrm{C_2H_4}^* + AgO^*_{nu} \xrightarrow{rds_{\mathrm{CO_2}}} \tag{5.4g}$$
$$\mathrm{C_2H_4O}_{AA} + AgO_{sub} + Ag$$

$$\mathrm{C_2H_4O}_{AA} + Ag \rightleftharpoons Ag\mathrm{C_2H_4O}^*_{AA} \tag{5.4h}$$

$$Ag\mathrm{C_2H_4O}^*_{AA} + 4\ AgO^*_{nu} + (AgO_{sub})O_{el} \longrightarrow \tag{5.4i}$$
$$2\,\mathrm{CO_2} + 2\mathrm{H_2O} + 5\ Ag + AgO_{sub}$$

First, gas-phase oxygen adsorbs on the metallic silver surface. Subsequently, the adsorbed oxygen then dissociates on a step to form nucleophilic oxygen species and metallic silver [144]. The nucleophilic oxygen diffuses into the subsurface to form subsurface oxygen which is required for the formation of EO [93, 94]. On this subsurface oxygen, the electrophilic oxygen is formed. Ethylene adsorbs on the subsurface oxygen site and reacts with either electrophilic or nucleophilic oxygen to form EO or AA, respectively. After formation, EO is desorbing, while AA adsorbs to a metallic silver site and is totally oxidized to $\mathrm{CO_2}$. The epoxidation mechanism of Schlögl [18] shows a complex formation and loss of active sites, which can only be captured by micro kinetic modeling. In macro kinetics, the rate determining step dictates the reaction rate. Therefore, the LHHW mechanism was chosen to derive the rate law for a selective and unselective site, assuming that the surface reaction is the rate determining step. This assumption requires that all adsorptions are in equilibrium. The nonselective site is represented by Ag_{step} where the nucleophilic oxygen is adsorbed while the electrophilic oxygen is adsorbed on a pre-adsorbed subsurface oxygen AgO_{sub}. The creation and loss of active sites is neglected. Assuming that the surface reaction is the rate determining step for both reactions, the rate law for the selective site can be derived in the following steps. First, the adsorption equilibrium for $\mathrm{CO_2}$ and DCE leads to the following equations:

$$m = \mathrm{CO_2}, \mathrm{DCE} \tag{5.5}$$

$$k_{\mathrm{m},ads}\ P_{\mathrm{m}}\ \theta_{AgO_{sub}} \rightleftharpoons k_{\mathrm{m},des}\ \theta_{\mathrm{m},AgO_{sub}} \tag{5.6}$$
$$\theta_{\mathrm{m},AgO_{sub}} = K_{\mathrm{m},AgO_{sub}}\ P_{\mathrm{m}}\ \theta_{AgO_{sub}} \tag{5.7}$$

$$k_{\mathrm{m},ads}\ P_{\mathrm{m}}\ \theta_{Ag_{step}} \rightleftharpoons k_{\mathrm{m},des}\ \theta_{\mathrm{m},Ag_{step}} \tag{5.8}$$
$$\theta_{\mathrm{m},Ag_{step}} = K_{\mathrm{m},Ag_{step}}\ P_{\mathrm{m}}\ \theta_{Ag_{step}} \tag{5.9}$$
$$\tag{5.10}$$

Ethylene is assumed to adsorb only on the selective site [18].

$$k_{\mathrm{C_2H_4},ads}\ P_{\mathrm{C_2H_4}}\ \theta_{AgO_{sub}} \rightleftharpoons k_{\mathrm{C_2H_4},des}\ \theta_{\mathrm{C_2H_4},AgO_{sub}} \tag{5.11}$$

$$\theta_{\mathrm{C_2H_4},AgO_{sub}} = K_{\mathrm{C_2H_4},AgO_{sub}}\ P_{\mathrm{C_2H_4}}\ \theta_{AgO_{sub}} \tag{5.12}$$

Since for the selective site subsurface oxygen is already present, two sites are required to form the electrophilic oxygen:

$$k_{\mathrm{O_2},ads}\ P_{\mathrm{O_2}}\ \theta^2_{AgO_{sub}} \rightleftharpoons k_{\mathrm{O_2},des}\ \theta^2_{\mathrm{O_{el}},AgO_{sub}} \tag{5.13}$$

$$\theta_{\mathrm{O_{el}},AgO_{sub}} = \sqrt{K_{\mathrm{O_2},AgO_{sub}}\ P_{\mathrm{O_2}}}\ \theta_{AgO_{sub}} \tag{5.14}$$

Analogically to the formation of electrophilic oxygen, two unselective sites are required to form nucleophilic oxygen:

$$k_{\mathrm{O_2},ads}\ P_{\mathrm{O_2}}\ \theta^2_{Ag_{step}} \rightleftharpoons k_{\mathrm{O_2},des}\ \theta^2_{O^*_{nu}} \tag{5.15}$$

$$\theta_{O^*_{nu}} = \sqrt{K_{\mathrm{O_2},Ag_{step}}\ P_{\mathrm{O_2}}}\ \theta_{Ag_{step}} \tag{5.16}$$

The sum of fraction of each active site results in 1, giving following equations:

$$\theta_{AgO_{sub}} = 1 - \theta_{\mathrm{O_{el}},AgO_{sub}} - \theta_{\mathrm{C_2H_4},AgO_{sub}} - \theta_{\mathrm{CO_2},AgO_{sub}} - \theta_{\mathrm{DCE},AgO_{sub}} \tag{5.17}$$

$$\theta_{AgO_{sub}} = \left(1 + \sqrt{K_{\mathrm{O_2},AgO_{sub}}\ P_{\mathrm{O_2}}} + K_{\mathrm{C_2H_4},AgO_{sub}}\ P_{\mathrm{C_2H_4}} + K_{\mathrm{CO_2},AgO_{sub}}\ P_{\mathrm{CO_2}} + K_{\mathrm{DCE},AgO_{sub}}\ P_{\mathrm{DCE}}\right)^{-1} \tag{5.18}$$

$$\theta_{Ag_{step}} = 1 - \theta_{O^*_{nu}} - \theta_{\mathrm{CO_2},Ag_{step}} - \theta_{\mathrm{DCE},Ag_{step}} \tag{5.19}$$

$$\theta_{Ag_{step}} = \frac{1}{1 + \sqrt{K_{\mathrm{O_2},Ag_{step}}\ P_{\mathrm{O_2}}} + K_{\mathrm{CO_2},Ag_{step}}\ P_{\mathrm{CO_2}} + K_{\mathrm{DCE},Ag_{step}}\ P_{\mathrm{DCE}}} \tag{5.20}$$

For the surface reaction as the rate determining step, following equations are obtained:

$$r_{EO} = k_{EO}\ \theta_{\mathrm{O_{el}},AgO_{sub}}\ \theta_{\mathrm{C_2H_4},AgO_{sub}} \tag{5.21}$$

$$r_{\mathrm{CO_2}} = k_{\mathrm{CO_2}}\ \theta_{O^*_{nu}}\ \theta_{\mathrm{C_2H_4},AgO_{sub}} \tag{5.22}$$

Combining eq. 5.7 - 5.22 leads to the final rate expression for the epoxidation reaction and total combustion of C_2H_4.

$$r_{EO} = \frac{k_{EO} \cdot \sqrt{K_{\mathrm{O_2},AgO_{sub}} \cdot P_{\mathrm{O_2}}} \cdot K_{\mathrm{C_2H_4},AgO_{sub}} \cdot P_{\mathrm{C_2H_4}}}{(1 + DEN_{AgO_{sub}})^2} \tag{5.23}$$

$$r_{CO_2} = \frac{k_{CO_2} \cdot \sqrt{K_{\mathrm{O_2},Ag_{step}} \cdot P_{\mathrm{O_2}}} \cdot K_{\mathrm{C_2H_4},AgO_{sub}} \cdot P_{\mathrm{C_2H_4}}}{(1 + DEN_{AgO_{sub}}) \cdot (1 + DEN_{Ag_{step}})} \tag{5.24}$$

with

$$DEN_{Ag_{step}} = \sqrt{K_{\mathrm{O_2},Ag_{step}}\ P_{\mathrm{O_2}}} + K_{\mathrm{CO_2},Ag_{step}}\ P_{\mathrm{CO_2}} + K_{\mathrm{DCE},Ag_{step}}\ P_{\mathrm{DCE}} \tag{5.25}$$

$$DEN_{AgO_{sub}} = \sqrt{K_{\mathrm{O_2},AgO_{sub}}\ P_{\mathrm{O_2}}} + K_{\mathrm{C_2H_4},AgO_{sub}}\ P_{\mathrm{C_2H_4}} + K_{\mathrm{CO_2},AgO_{sub}}\ P_{\mathrm{CO_2}} + K_{\mathrm{DCE},AgO_{sub}}\ P_{\mathrm{DCE}} \tag{5.26}$$

The bimolecular reaction rate for the selective reaction, r_{EO}, takes into account the adsorption of reactants O_2 and C_2H_4 and the reactants adsorbed on the selective catalytic sites such as CO_2 and DCE. First rate measurements showed that the reaction rates

are independent of the C_2H_4 concentration. This is due to the excess of C_2H_4 in the reaction mixture, which is 5 times the concentration of O_2. C_2H_4 was still considered in the rate law, which was derived from the mechanism proposed by the group of Schlögl [18], assuming the surface reaction as the rate determining step. For the unselective reaction, r_{CO_2}, the adsorption term for both sites has to be considered since C_2H_4 is assumed to adsorb only at the same site as electrophilic oxygen, see eq. 5.4e. The adsorption of H_2O was completely neglected because the reaction order was close to zero. Chlorine adsorption takes place on both nucleophilic and electrophilic sites since both reaction rates to EO and CO_2 are decreasing (Figure 5.5). Chlorine adsorption increases the EO selectivity by suppressing the unselective reaction rate to CO_2 more than the selective reaction rate to EO. The chlorine deposition via oxychlorination of the silver surface with DCE is assumed to take place only with the nucleophilic oxygen, occupying the unselective site with chlorine and decreasing the fractional coverage of nucleophilic oxygen atoms [93]. The rate law for the chlorine deposition reaction can then be written as:

$$\begin{aligned} r_{DCE} &= k_{DCE,AgO_{sub}} \cdot \theta_{DCE,AgO_{sub}} \cdot \theta_{O^*_{nu}} \\ &+ k_{DCE,Ag_{step}} \cdot \theta_{DCE,Ag_{step}} \cdot \theta_{O^*_{nu}} \end{aligned} \tag{5.27}$$

$$\begin{aligned} r_{DCE} = &\frac{k_{DCE,AgO_{sub}} \cdot \sqrt{K_{\mathrm{O_2},Ag_{step}} \cdot P_{\mathrm{O_2}}} \cdot K_{DCE,AgO_{sub}} \cdot P_{\mathrm{DCE}}}{(1 + DEN_{AgO_{sub}})(1 + DEN_{Ag_{step}})} \\ &+ \frac{k_{DCE,Ag_{step}} \cdot \sqrt{K_{\mathrm{O_2,Ag_{step}}} \cdot P_{\mathrm{O_2}}} \cdot K_{\mathrm{DCE,Ag_{step}}} \cdot P_{\mathrm{DCE}}}{(1 + DEN_{Ag_{step}})^2} \end{aligned} \tag{5.28}$$

To improve the robustness in the parameter estimation with the least-squares algorithm, the kinetic expression was reparametrized [145]. The reparametrization reduces the correlation between the frequency factor and the activation energy, as well as between the sticking coefficient and the heat of adsorption [146, 147]:

$$k_k = exp\left[ln(A_k) - \frac{Ea_k}{R \cdot T_{av}} + \frac{Ea_k}{R \cdot T_{av}} \cdot \left(\frac{T - T_{av}}{T}\right)\right], k = EO, CO_2 \tag{5.29}$$

$$k_{DCE,j} = exp\left[ln(k^0_{DCE,j}) - \frac{Ea_{DCE,j}}{R \cdot T_{av}} + \frac{Ea_{DCE,j}}{R \cdot T_{av}} \cdot \left(\frac{T - T_{av}}{T}\right)\right], j = AgO_{sub}, Ag_{step} \tag{5.30}$$

$$K_{i,j} = exp\left[ln(A_{i,j}) - \frac{\Delta H_{i,j}}{R \cdot T_{av}} + \frac{\Delta H_{i,j}}{R \cdot T_{av}} \cdot \left(\frac{T - T_{av}}{T}\right)\right], i = species \tag{5.31}$$

Depending on the temperature of each experiment, x, the average temperature, T_{av}, was calculated according to eq. 5.32 [147].

$$T_{av} = \left(\frac{1}{No.Exp.} \sum_x \frac{1}{T_x}\right)^{-1} \tag{5.32}$$

To evaluate the correlations between the fitted parameters the covariance matrix $M_\tau(i,j)$ was determined (eq. 5.33) from the Jacobian and the variance of the experimental fluctuations (assumed to be constant) [147].

$$M_\tau(i,j) = s^2 \cdot (J^T J)^{-1} \tag{5.33}$$

The Jacobian is obtained by the sensitivity analysis of the objective function of the corresponding fit parameter. The correlation between the fitting parameters is

calculated with eq. 5.34, where $\tau(i,j)$ is the covariance of parameter i and j and $s_{i,i}^2$ the variance of parameter i and $s_{j,j}^2$ the variance of parameter j.

$$\kappa_{i,j} = \frac{\tau(i,j)}{\sqrt{s_{i,i}^2 \cdot s_{j,j}^2}} \tag{5.34}$$

The evaluation of the binary interaction of the kinetic parameters is shown in Tables A.1-A.3 which can be found in the appendix in Section A.2.

The measured profiles were fitted by fitting the pre-exponential factors, activation energies and adsorption enthalpies using Comsol Multiphysics 5.5^{TM} applying the Levenberg-Marquardt solver algorithm. The method of the sum of squares minimization was applied to minimize the error of the measured and the fitted profiles using a plug flow model as described in Chapter 2.4.2. All profiles were fitted simultaneously to obtain parameters valid for all measured conditions.

5.2 Compact Profile Reactor

5.2.1 Heat and Mass Transfer Gradients

Mechanistic studies and kinetic parameter regression were performed using the profiles measured in the CPR. To ensure that these studies are not superimposed by heat or mass transfer effects the analytical methods introduced in Chapter 2.1.2 were applied.

External Gradients

Equation 2.11 was evaluated for the standard concentration conditions listed in Table 4.2 at a GHSV of 4750 h^{-1} a wall temperature of 225 °C and reactor pressure of 17 bara to verify the absence of external limitation effects analogically to Chapter 5.1.1. The used parameters are shown in Table 5.5, the remaining missing parameters were the same as in Table 5.1.

Table 5.5: Parameter for External Limitation Criteria Applied for the CPR Measurements.

Parameter	Value	Unit
k_f	$1.88 \cdot 10^{-4}$	m· s^{-1}
h	3.79	$W \cdot m^{-2} \cdot K^{-1}$
$r_{v,obs}$	0.53	$mol \cdot m^{-3} \cdot s^{-1}$

$$|\gamma_b \cdot \beta_e \cdot Ca| = |20.177 \cdot 0.307 \cdot 0.006| = 0.037 < 0.05 \tag{5.35}$$

The result of eq. 5.35 shows that external limitation during the profile measurements were negligibly small.

Internal Gradients

The criterion for the testing of internal gradients was applied analogously to Chapter 5.1.1 at the same reaction conditions like the external limitation testing above. All required parameters are listed in Table 5.5, Table 5.2, and Table 5.1, respectively.

$$\left|\gamma_s \cdot \beta_i \cdot \eta_i \phi^2\right| = \left|20.159 \cdot 0.739 \cdot 10^{-2} \cdot 0.671 \cdot 10^{-3}\right| = 9.996 \cdot 10^{-5} < 0.1 \tag{5.36}$$

The evaluation of eq. 5.36 shows that internal gradients are sufficiently small to be neglected during the CPR measurements.

Catalyst Bed Gradients

Since mass transfer in radial direction is negligible compared to heat-transfer eq. 5.3 can be evaluated analogously to Chapter 5.1.1 to verify whether catalyst bed gradients in radial direction are present. The parameters used in the criteria are listed in Table 5.6. The remaining required parameters are listed in Table 5.5.

Table 5.6: Parameter for the Catalyst Bed Limitation Criteria Applied for the CPR Measurements.

Parameter	Value	Unit
T_w	493	K
$\lambda_{bed,eff}$	0.33	$W \cdot m^{-1} \cdot K^{-1}$
d_t	4	mm
d_p	400	µm
$Bi_{h,w}$	0.26	-

$$|\gamma_w \cdot \beta_w \cdot B_w| = \left|20.177 \cdot 0.133 \cdot 10^{-2} \cdot 0.259\right| = 0.007 < 0.05 \tag{5.37}$$

The result of eq. 5.37 shows that catalyst bed gradients can be neglected during the CPR profile measurements.

5.2.2 CPR Profiles for Mechanistic Studies

GHSV = 4750 h^{-1}, 225 °C, 17 bara, and 1.25 ppm DCE

In Figure 5.8, molar flow rate and temperature profiles are shown for a GHSV of 4750 h^{-1} at a reactor pressure of 17 bara and a heating block temperature of 225 °C measured in a fused silica reactor tube. 1.25 ppm DCE was fed in this experiment. The other species concentrations are as listed in Table 4.2.

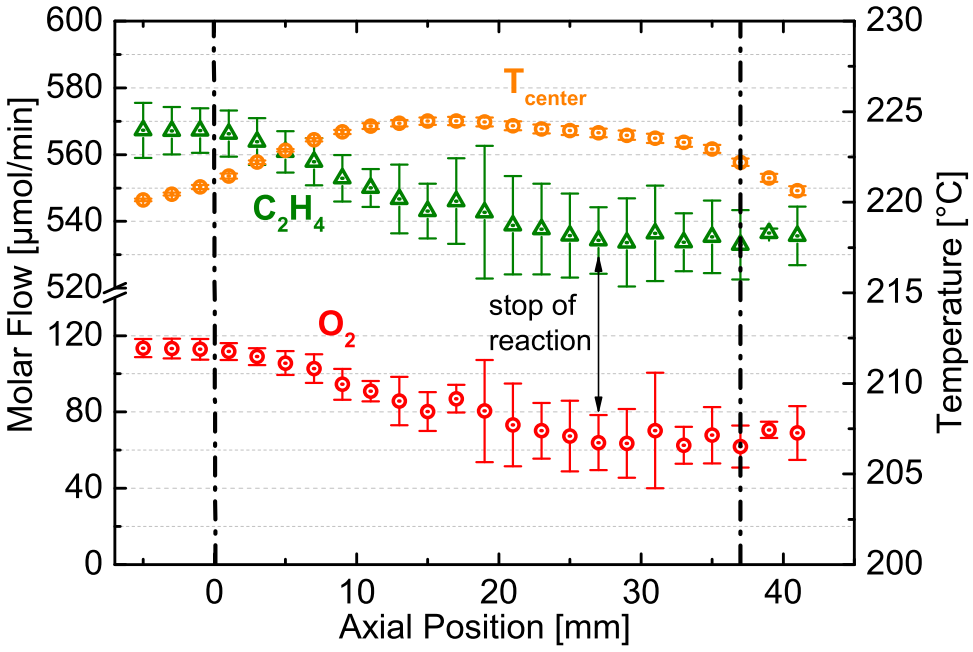
Molar Flow [µmol/min]
Temperature [°C]
Axial Position [mm]
T center
C2H4
O2
stop of
reaction
600
580
560
540
520
120
80
40
0
230
225
220
215
210
205
200
0
10
20
30
40

(a)

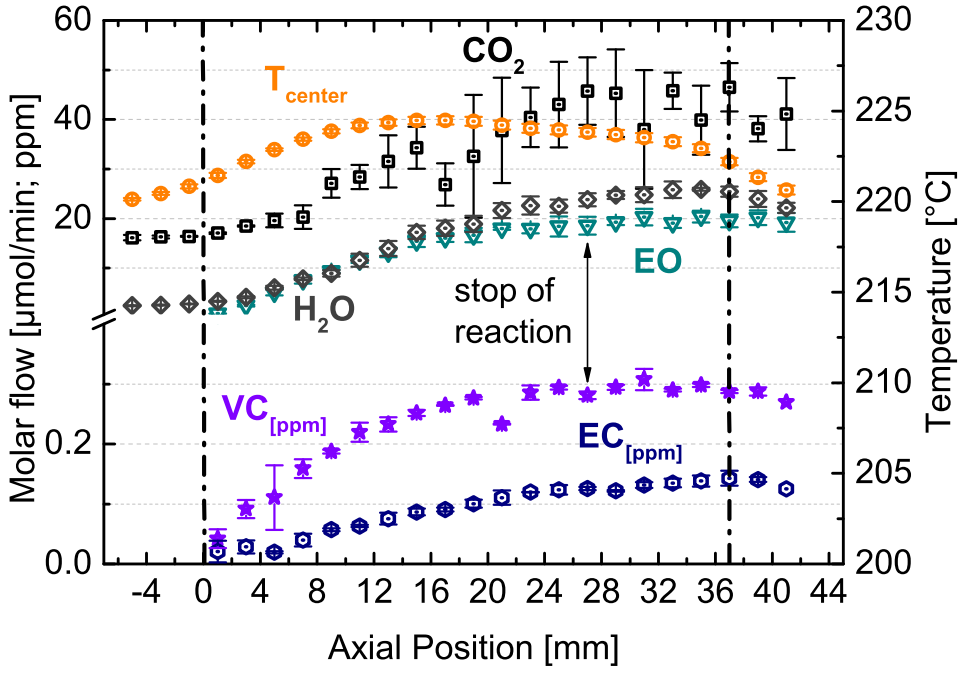
Molar flow [µmol/min; ppm]
Temperature [°C]
Axial Position [mm]
T center
CO2
H2O
EO
stop of
reaction
VC [ppm]
EC [ppm]
60
40
20
0.2
0.0
230
225
220
215
210
205
200
-4
0
4
8
12
16
20
24
28
32
36
40
44

(b)

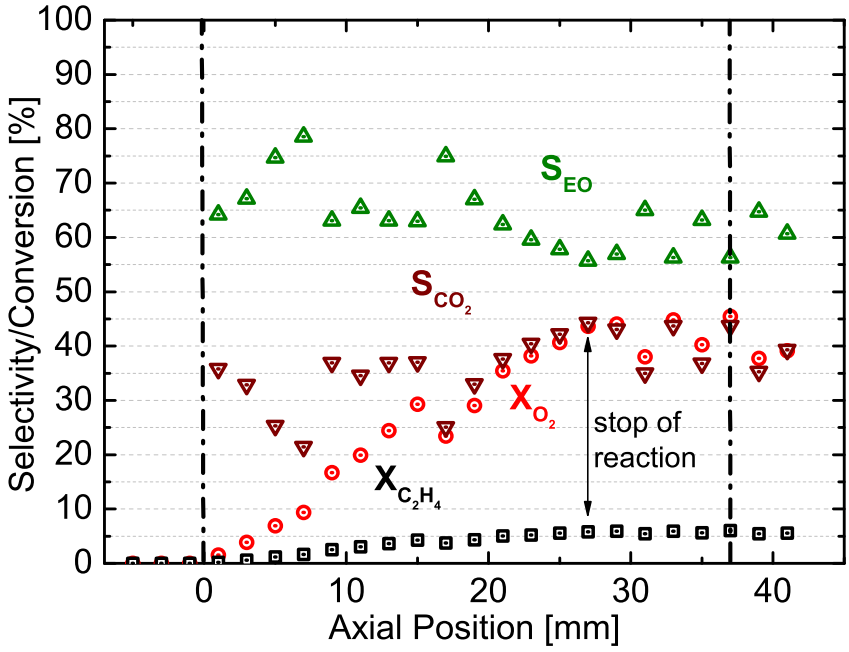

(c)

Figure 5.8: Molar flow rate and temperature profiles measured in the CPR at GHSV = 4750 h^{-1}, 225 °C heating block temperature, 17 bara pressure, and 1.25 ppm DCE concentration in the feed. (a) educt profiles and temperature, (b) product profiles, (c) conversion of oxygen and ethylene and selectivities to EO and CO_2.

Figure 5.8a shows the profiles of reactants ethylene and oxygen, as well as the temperature in the center of the catalyst bed. The vertical dashed-dotted lines indicate the beginning (0 mm) and the end (37 mm) of the catalyst bed, respectively. Before the catalyst bed begins, no conversion is observed, indicating that gas-phase reactions or reactions on the pure $\alpha - Al_2O_3$ support do not occur. Starting from the entrance of the catalyst bed (0 mm), O_2 and C_2H_4 are consumed up to about 27 mm. At this position, reactant consumption and product formation stop despite that C_2H_4 and O_2 are still available in the gas phase. Figure 5.8c shows that the conversion of C_2H_4 and O_2 at the end of the catalyst bed is only 5 % and 40 %, respectively.

Figure 5.8b shows the development of the reaction products. The vertical axes are split in two parts, the upper showing the molar flow of the main species in $\mu mol \cdot min^{-1}$ and the lower showing the concentration of VC and EC in ppm. DCE could not be measured in this experiment. Ethylene oxide, water, and carbon dioxide are formed from the beginning of the catalyst bed, indicating that all of them are primary products. Other reaction products, e.g., formaldehyde, were not observed. The production rates of EO, CO_2, and H_2O increase with increasing temperature, showing a maximum at around 15 mm which corresponds to the maximum temperature in the catalyst bed and then decrease to zero at about 27 mm. The scatter in the EO and CO_2 selectivity profiles is rather high, but there is a trend that the selectivity to EO decreases slightly with increasing ethylene conversion. EO selectivity is about 70 % at the entrance of the catalyst bed and decreases to about 60 % at 27 mm where the catalytic reactions effectively stop. Conversely, CO_2 selectivity increases from about 30 % to about 40 %. Since both EO and CO_2 are formed with a selectivity

$\gg 0$ % right from the reactor entrance (zero conversion), both products are identified as primary reaction products being formed in parallel channels (cp. Figure 2.8). With increasing conversion, EO selectivity decreases and CO_2 selectivity increases either due to changing rates of the parallel formation pathways or because of the consecutive reaction of EO to CO_2.

The halogenated trace components VC and EC, which are formed in subppm concentrations from DCE, show a different development. The profile of VC rises from the beginning of the catalyst bed until it reaches a plateau at 27 mm. This is exactly the position in the catalyst bed where all reactions cease. As VC is formed from DCE according to eq. 2.51, VC formation is indicative of chlorine deposition onto the silver surface. EC, which is formed from ethane by oxychlorination according to eq. 2.53, is indicative of chlorine removal from the Ag surface. Close inspection of the EC profile shows that EC is not formed right from the beginning of the catalyst bed. The first point, where the EC profile is higher than the baseline, is at about 5 mm. Just like VC, also EC plateaus from 27 mm on.

The concentration of both VC and EC is at the detection limit of the GC method, making a quantitative interpretation of their profiles difficult. In fact, at steady state, the deposition rate of chlorine atoms onto the silver surface must equal the rate of removal of chlorine atoms from the silver surface, and both the VC and EC profiles should fall on top of each other. However, in Figure 5.8b, the VC profile rises more steeply than the EC profile. If interpreted in the foregoing way, there would be a net chlorine deposition on the catalyst. The different developments of the VC and EC profile can have several reasons: First, the reactor might not have been in steady state yet, causing indeed a net chlorine deposition on the catalyst. This assumption is rather unlikely since the catalyst was pretreated with the reaction mixture for a 100 h time period on stream before the profiles in Figure 5.8 were recorded. The measurement of one set of profiles took 56 h from the entrance to the end of the bed. Assuming that all silver atoms were exposed to the gas phase at a 14.5 wt-% loading of silver and a total catalyst mass of 637 mg, it would have taken approximately 12 h with a DCE concentration of 1.25 ppm to chlorinate all silver atoms. Second, significant amounts of deposited chlorine might go subsurface [96]. Also, this explanation is rather unlikely taking into account that saturation would have been reached within a few hours. Next, chlorinated species could be formed, which were not detected by the applied GC method, removing chlorine from the silver surface. Also, the calibrations of VC and EC could not have been accurate enough such that the observed deviations are simply measurement errors. The most likely explanation, however, is that before EC can leave the silver surface, it reacts with oxygen atoms to VC in an oxidative dehydrogenation reaction.

$$C_2H_5Cl + AgO \rightarrow C_2H_3Cl + Ag + H_2O \tag{5.38}$$

If this was the case, the VC profile would reflect both chlorine deposition and chlorine removal, and the VC profile could indeed be higher than the EC profile. An oxidative dehydrogenation of EC to VC according to eq. 5.38 could also explain that EC is not formed right from the entrance of the catalyst bed where the catalyst temperature is still low and the gas-phase oxygen concentration is highest, leading to a high concentration of oxygen atoms at the silver surface and in turn to a rapid consecutive reaction of EC to VC. As the catalyst temperature increases and the gas-phase oxygen concentration decreases, the coverage of AgO drops, and EC can escape into the gas phase. The slopes of the VC and EC profiles decrease with increasing distance from the entrance of the catalyst bed, indicating that chlorination and dechlorination decrease in rate until they stop entirely at 27 mm. From this point on, VC and EC

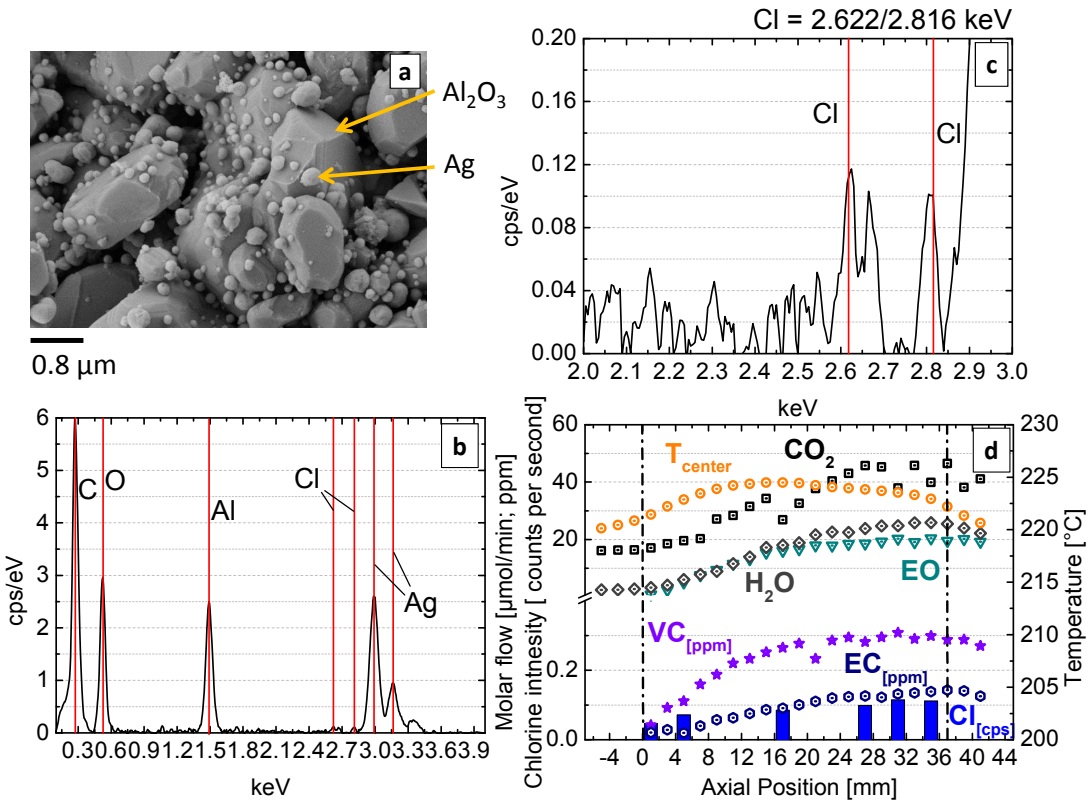

Figure 5.9: a) SEM picture of the Ag/Al_2O_3 catalyst. b) EDX spectrum of main components. c) EDX spectrum at the noise level. d) Species profiles and chlorine signal heights.

formation stops, just like all other reactions. The most obvious explanation for the stop of all reactions from this point onward is that all active silver atoms are blocked by chlorine. The oxygen partial pressure has become too low to remove chlorine by oxychlorination. To verify this, the catalyst was extracted layer by layer from the reactor, and EDX measurements were performed as shown in Figure 5.9. The chlorine signals are small but can be distinguished from noise level. Plotting the signal intensity vs. position shows that chlorine is already present at the silver surface from the entrance of the catalyst bed and increases along the reactor length (Figure 5.9 d). The trend is subtle, but also the chlorine signal plateaus from around 27 mm, in line with the hypothesis that the blockade of Ag sites by chlorine is the reason for ceased activity of the catalyst. Taking into account that O_2 has a strong positive and DCE a strong negative impact on EO and CO_2 formation (cf. Chapter 5.1.2), one probable explanation for the increasing chlorine coverage along the catalyst bed is that O and Cl, both electrophiles, are competing for the same adsorption sites. Cl adsorbs much stronger than O, which is why it can compete for Ag sites despite being present only in single-digit ppm concentrations compared with O_2 being present at a concentration of 7 vol-% (70.000 ppm). With decreasing O_2 concentration in the gas-phase, the O coverage at the surface decreases, and the active Ag sites become irreversibly blocked by chlorine because the adsorption strength of chlorine increases with decreasing O-coverage.

GHSV = 9500 h^{-1}, 225 °C, 17 bara, and 1.25 ppm DCE

A second measurement was performed in the CPR at GHSV = 9500 h^{-1} corresponding to doubled flow rates using again the feed composition in Table 4.2 with 1.25 ppm DCE. The data are shown in Figure 5.10. As expected, doubling the GHSV leads to a stretch of all profiles. The VC profile rises from the beginning of the catalyst bed and plateaus at around 19 mm. In contrast, the EC profile is zero from the entrance of the catalyst bed until about 11 mm. Between 11 and 19 mm, the EC profile rises, and from 19 mm onward, the EC profile plateaus just like the VC profile, with, if at all, a very small increase in EC molar flow rate toward the end of the catalyst bed. Again, as chlorine deposition and removal rates must be equal in steady state, these very different profile shapes of VC and EC can only be explained if i) chlorine deposition and chlorine removal lead both to the formation of VC, e.g. by simultaneous occurrence of reactions shown in eq. 2.51, 2.53, and 5.38 or ii) if chlorine is removed from the Ag surface by another, yet undetected molecular species.

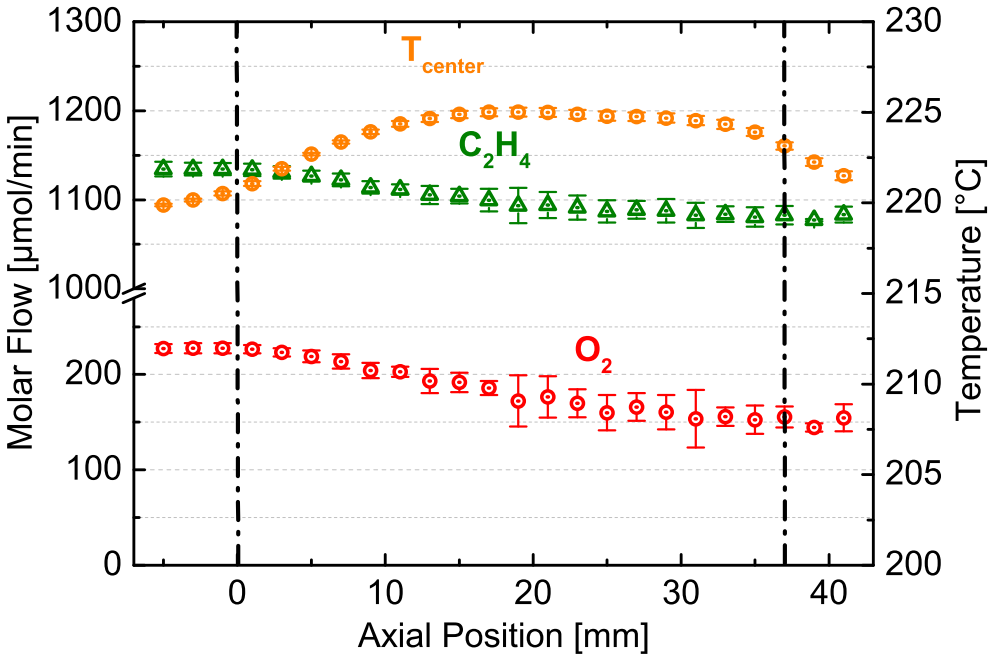

(a)

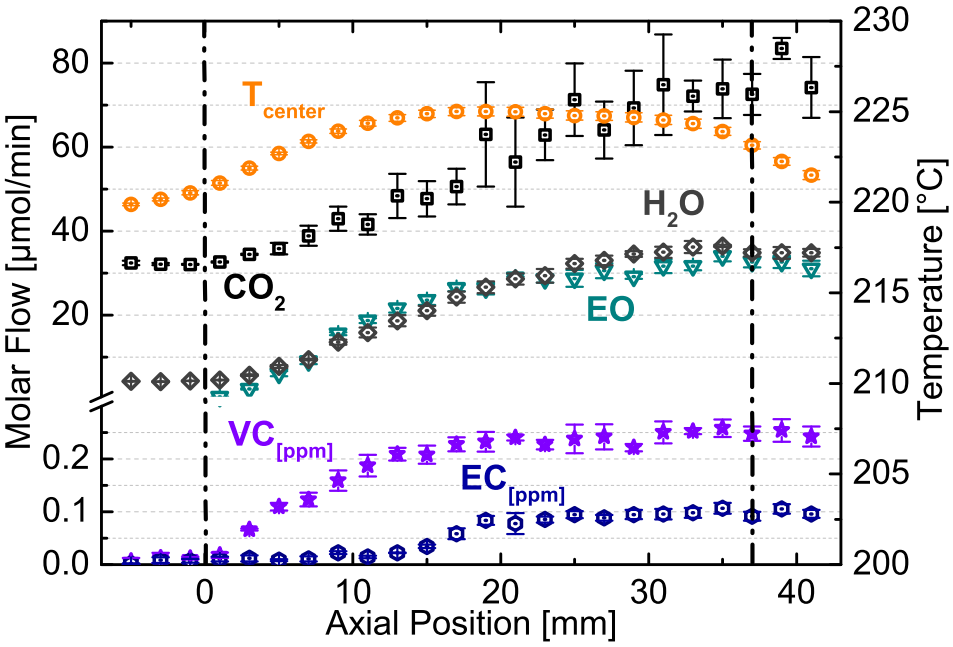

(b)

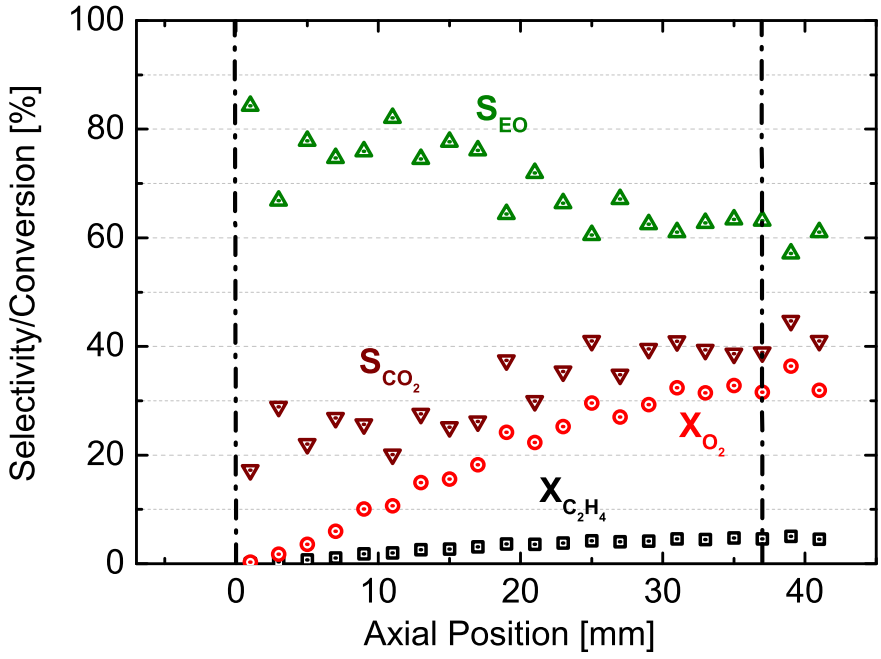

(c)

Figure 5.10: CPR profiles at GHSV = 9500 h^{-1}, 225 °C heating block temperature, 17 bara pressure, and 1.25 ppm DCE concentration in the feed. (a) educt profiles and temperature, (b) product profiles, (c) conversion of oxygen and ethylene and selectivities to EO and CO_2.

The lack of EC production before 11 mm would be in line with a more efficient EC conversion to VC according to eq. 5.38 due to a longer zone of oxygen-covered silver sites at GHSV = 9500 h^{-1}. Indeed, overall less VC is formed at GHSV = 9500 h^{-1} (0.22 ppm, Figure 5.10b) compared with GHSV = 4750 h^{-1} (0.30 ppm, Figure 5.8b), highlighting again the delicate competition oxygen adsorption and chlorine adsorption. The conversion of C_2H_4 and O_2 stretches almost entirely over the catalyst bed. In contrast to GHSV = 4750 h^{-1}, both C_2H_4 and O_2 conversion does not come to hold because the higher O_2 concentration throughout the bed prevents complete coverage of the silver surface with chlorine. At the end of the bed, O_2 conversion reaches about 32 % compared to about 40 % at GHSV = 4750 h^{-1}. According to the kinetic measurements presented in Chapter 5.1.2, the reaction is first-order with respect to the stoichiometrically limiting reactant oxygen. External and internal mass and heat-transfer limitations can be neglected according to the criteria evaluated in Chapter 5.2.1 [40]. Because the CPR is in good approximation a plug flow reactor, the following mole balance can be formulated for O_2:

$$Da = -ln(1 - X) \tag{5.39}$$

Therefore, a conversion of $X_{O_2} = 0.4$ at GHSV = 4750 h^{-1} corresponds to a Damköhler number of $Da(4750\ h^{-1}) = 0.52$. For a first-order reaction, $Da = k_{app} \cdot \tau$, with k_{app} being the apparent rate constant and τ the hydrodynamic residence time. At GHSV = 9500 h^{-1} and otherwise identical conditions, $Da(9500\ h^{-1}) = 0.26$. From this Da number, a conversion of $X(9500\ h^{-1}) = 0.23$ should be expected, which is much lower than the measured value of $X(9500\ h^{-1}) = 0.32$. Also, this calculation supports the hypothesis that O and Cl compete for the same active sites. At GHSV = 9500 h^{-1}, the O_2 concentration in the gas phase throughout the catalyst bed is higher than at GHSV = 4750 h^{-1}, leading to fewer chlorine-blocked Ag sites. Quantitatively, this means that the apparent rate constant, k_{app}, containing the active site density as a factor, is higher at GHSV = 9500 h^{-1} than at GHSV = 4750 h^{-1} at otherwise constant temperature and pressure conditions. In consequence, a higher conversion is reached at GHSV = 9500 h^{-1} than what would be expected from the reduced contact time.

GHSV = 9500 h^{-1}, 225 °C, 17 bara, and 2.50 ppm DCE

Figure 5.11 shows profiles for GHSV = 9500 h^{-1} and 2.50 ppm DCE in the feed measured in the CPR in a stainless steel reactor tube at otherwise identical conditions as in the experiments in Section 5.2.2.

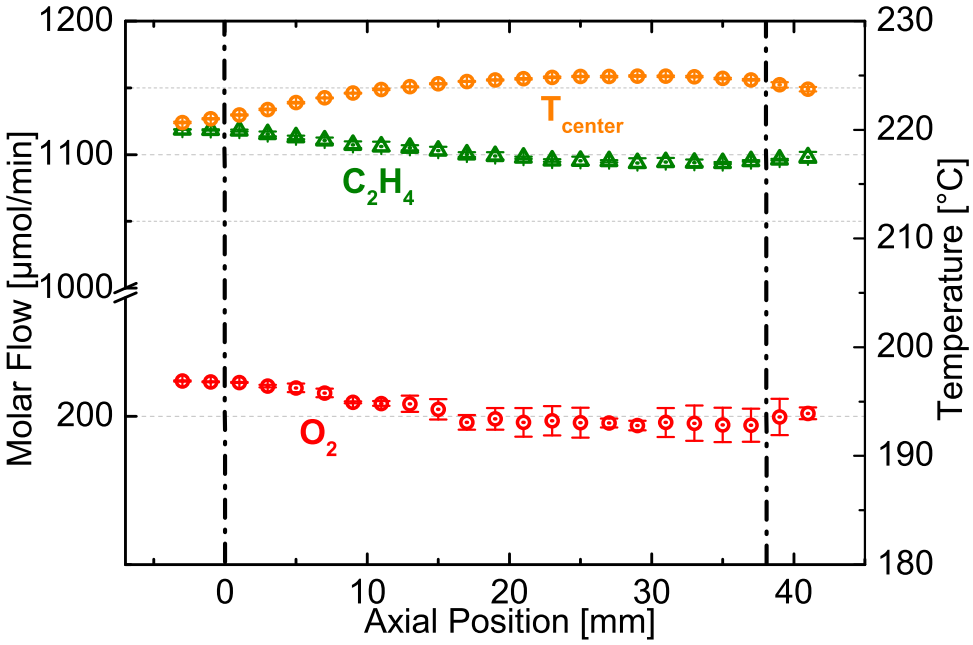
1200
1100
1000
200
Molar Flow [µmol/min]
230
220
210
200
190
180
Temperature [°C]
T center
C2H4
O2
0
10
20
30
40
Axial Position [mm]

(a)

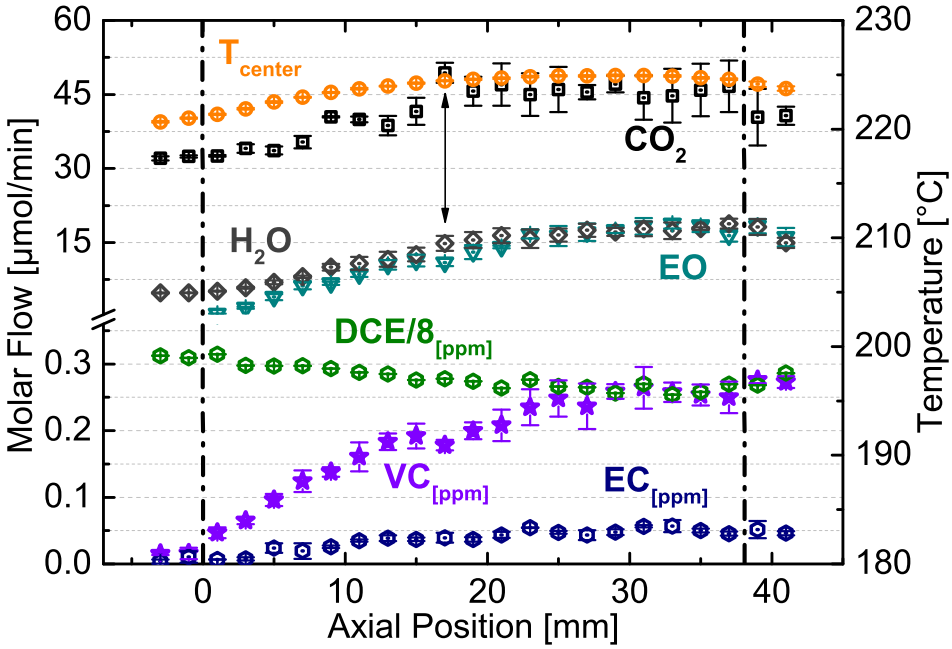
60
45
30
15
0.3
0.2
0.1
0.0
Molar Flow [µmol/min]
230
220
210
200
190
180
Temperature [°C]
T center
CO2
H2O
EO
DCE/8[ppm]
VC[ppm]
EC[ppm]
0
10
20
30
40
Axial Position [mm]

(b)

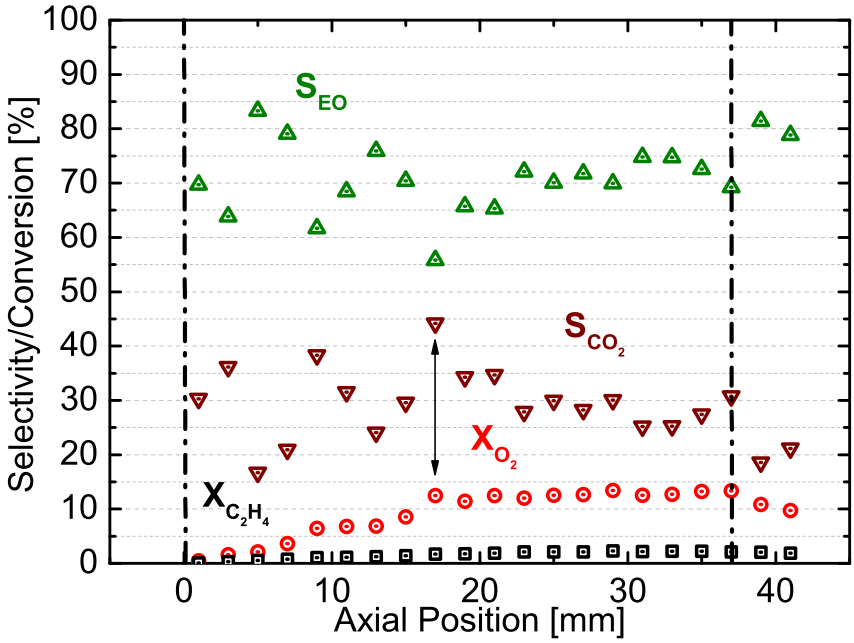

(c)

Figure 5.11: CPR profiles at GHSV = 9500 h^{-1}, 225 °C heating block temperature, 17 bara pressure, and 2.50 ppm DCE concentration in the feed. (a) educt profiles and temperature, (b) product profiles, (c) conversion of oxygen and ethylene and selectivities to EO and CO_2.

Doubling the DCE concentration in the feed reduces the reactant conversion drastically, from 32 % O_2 conversion at the bed exit at 1.25 ppm DCE to 14 % at 2.5 ppm DCE. The O_2 molar flow rate profile decreases slowly in the first half of the catalyst bed. From 16 mm onward, the decrease is barely visible anymore. Selectivities remain almost constant throughout the bed with an average of 70 % for EO and 30 % for CO_2. In this experiment, DCE could be measured as well, showing the expected decline. Comparing the VC and EC profiles in Figures 5.10b and 5.11b, respectively, shows that doubling the DCE concentration leads to only slightly more VC formation and even less EC formation (VC: 0.25 ppm vs. 0.22 ppm, EC: 0.05 ppm vs. 0.1 ppm, respectively). The onset of EC formation shifts from 11 mm (1.25 ppm DCE and GHSV = 9500 h^{-1}) to 3 mm (2.5 ppm DCE and GHSV = 9500 h^{-1}) in line with the interpretation that less surface oxygen atoms are available for the oxidative dehydrogenation of EC to VC according to eq. 5.38.

5.2.3 Interrupting DCE Feeding

Directly after a profile had been recorded feeding 1.25 ppm DCE (GHSV = 4750 h^{-1}, 17 bara reactor pressure, 225 °C heating block temperature, and standard feed composition as listed in Table 4.2), the DCE feeding was interrupted, and measurements were conducted in the CPR without cofeeding of DCE. As the sampling capillary was now behind the catalyst bed, this profile was measured in reverse direction, viz., from outlet to inlet. The measurement started immediately after switching off the DCE feed and took 56 h for the complete profile. The data are shown in Figure 5.12.

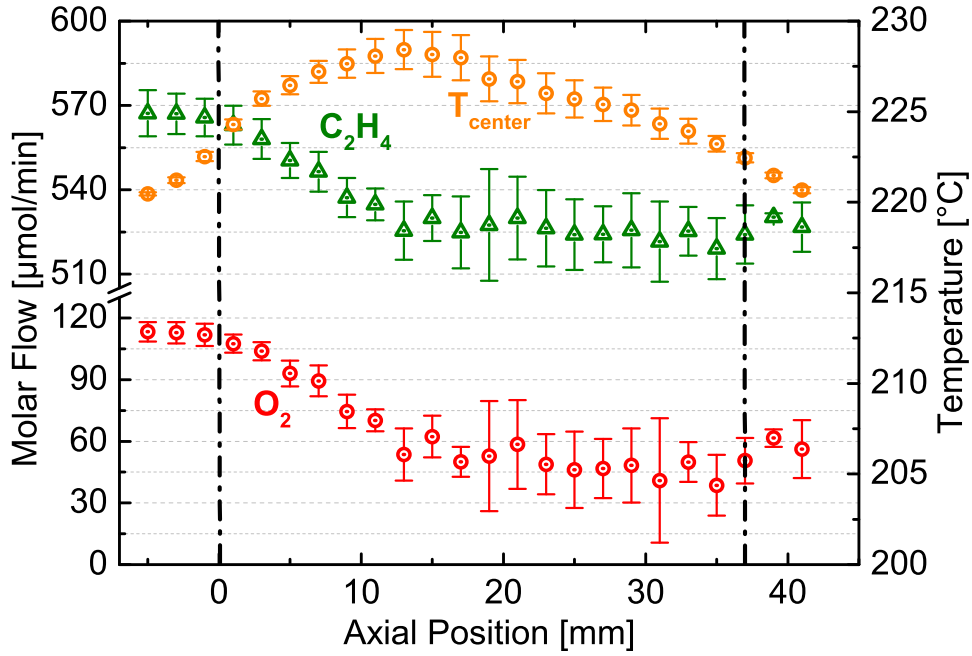
600
570
540
510
120
90
60
30
0
230
225
220
215
210
205
200
0
10
20
30
40
Molar Flow [µmol/min]
Temperature [°C]
Axial Position [mm]
C2H4
O2
Tcenter

(a)

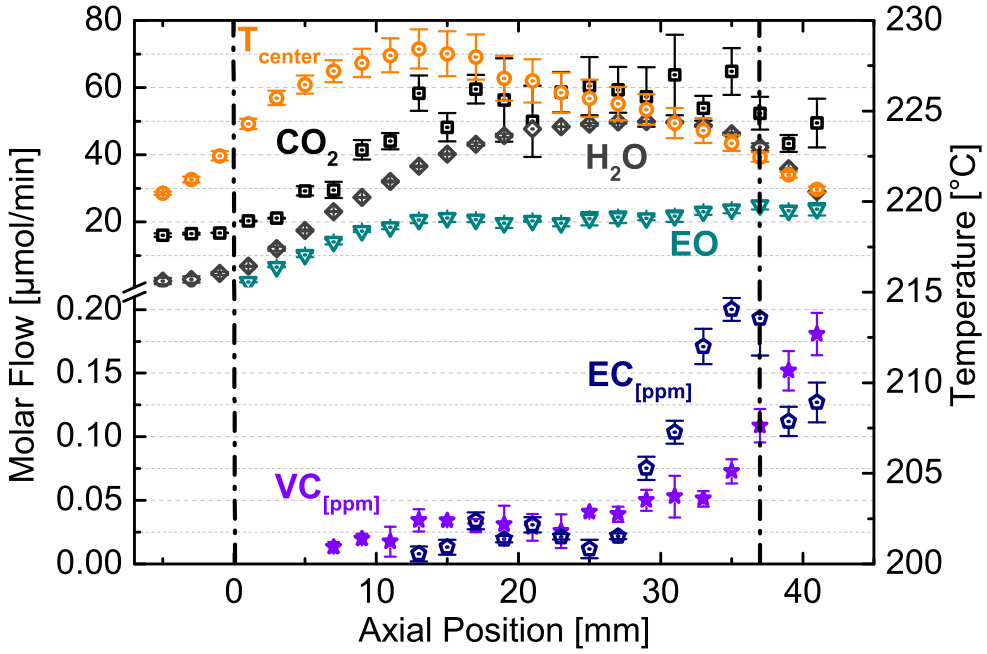
80
60
40
20
0.20
0.15
0.10
0.05
0.00
230
225
220
215
210
205
200
0
10
20
30
40
Molar Flow [µmol/min]
Temperature [°C]
Axial Position [mm]
Tcenter
CO2
H2O
EO
EC[ppm]
VC[ppm]

(b)

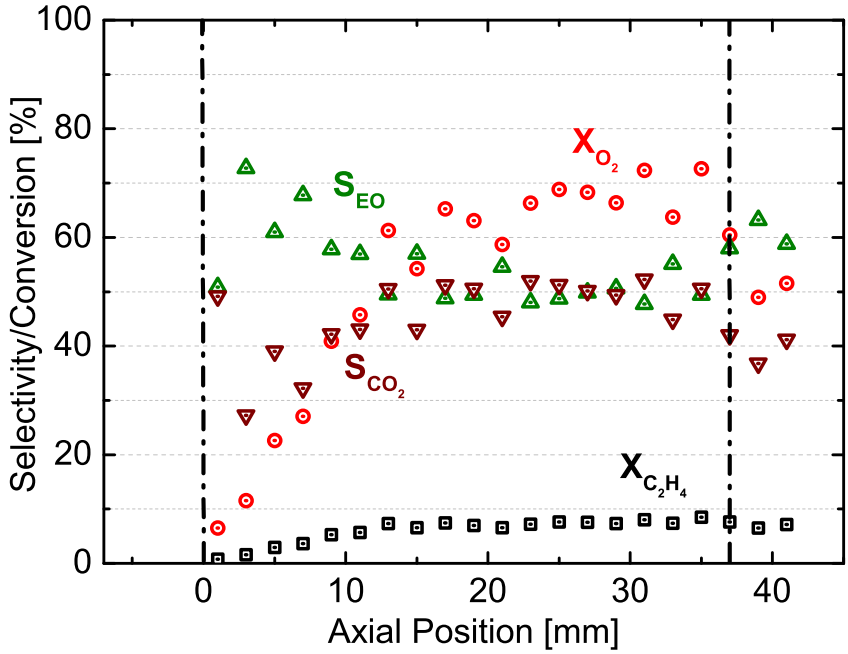

(c)

Figure 5.12: CPR profiles at GHSV = 4750 h^{-1}, 225 °C heating block temperature, and 17 bara pressure without DCE cofeeding. Profile measurement from outlet to inlet. (a) educt profiles and temperature, (b) product profiles, (c) conversion of oxygen and ethylene and selectivities to EO and CO_2.

In Figure 5.12a, the reactant profiles are shown. In comparison to the same experimental conditions with a DCE cofeeding of 1.25 ppm (see Figure 5.8a), O_2 and C_2H_4 are consumed more rapidly right from the beginning of the catalyst bed. Both profiles, C_2H_4 and O_2, decrease steeply until 13 mm into the catalyst bed. At 13 mm, reactant conversion ceases abruptly. From this position on to the end of the bed, the rates of C_2H_4 and O_2 consumption are very small. Overall, reactant conversion is higher without DCE cofeeding. As shown in Figure 5.12c, O_2 conversion reaches ≈ 70 % at the end of the bed in comparison to the same measurement with 1.25 ppm DCE cofeeding in Figure 5.8c, where only 40 % O_2 conversion was reached. The temperature profile increases in front of the catalyst bed since the wall temperature was not reached in the prepacking. With heat release from the reaction, the temperature increases, reaching a hot spot at about 13 mm when reactant conversion stops. After the hot spot, the temperature decreases until the end of the bed. The cause of the sudden slowdown of reactant conversion at around 13 mm is again the coverage of the silver surface with chlorine. Even though no DCE was fed in this experiment, VC and EC are still removed from the surface, and the onset points of both profiles match in good approximation the position at which the conversion of the reactants comes to hold (cp. Fig. 5.12b, lower part). From 7 mm until 25 mm, viz., in a zone around the hot spot, it seems that the VC profile is higher than the EC profile. From 25 mm until the bed exit, the EC profile increases steeply, overtaking the VC profile. The fact that VC is formed at all, even without cofeeding of any chlorine precursor in the feed, substantiates the thesis that VC formation is an additional chlorine removal channel from the silver surface. Taking into account that EC formation overtakes VC toward

the end of the catalyst bed, viz., in the first measurements points in this instationary experiment (profile was measured from outlet to inlet) supports the hypothesis that EC formation according to eq. 2.53 is the primary chlorine removal channel. At high surface oxygen concentrations, EC is immediately converted into VC by eq. 5.38, but this pathway is not effective here anymore because O_2 conversion has reached ≈ 70 % as shown in Figure 5.12c.

Despite some scatter in the data, the chlorine coverage profile is also reflected in the selectivity development of EO and CO_2 as shown in Figure 5.12c. The EO and CO_2 selectivities extrapolated to the entrance of the catalyst bed amount to about 80 % and 20 %, respectively. With increasing conversion, EO selectivity drops steeply and CO_2 selectivity rises steeply, until about 7 mm into the bed, the point from which VC formation is detected being indicative of some remaining chlorine coverage of the Ag surface. From this point onward until about 29 mm, the decrease/increase of EO/CO_2 selectivity is very small. From 29 mm until the end of the catalyst bed, viz., in the zone of still high chlorine coverage, the EO selectivity seems to increase again, while the CO_2 selectivity decreases accordingly, indicating again a parallel formation of EO and CO_2 with relative rates depending on the chlorine coverage. In summary, the data in Figure 5.12 show that chlorine remains at the silver surface for some time after DCE feeding is terminated. Whether this chlorine is surface bound or whether it segregates slowly from the silver bulk to the surface cannot be inferred from the data. In any case, the surface-bound chlorine slows down reactant conversion significantly but favors the formation of EO over CO_2. The detection of VC and EC without feeding DCE indicates that surface chlorine is removed by both, VC and EC formation. Most likely, EC is the primary chlorine removal product, while VC is formed from EC.

After the first measurement without feeding DCE was completed, a second measurement without DCE cofeed was started, without changing any parameters. The measurement took again 56 h; the only difference was that this second profile without DCE cofeed was measured from inlet to outlet. The results of this measurement are shown in Figure 5.13.

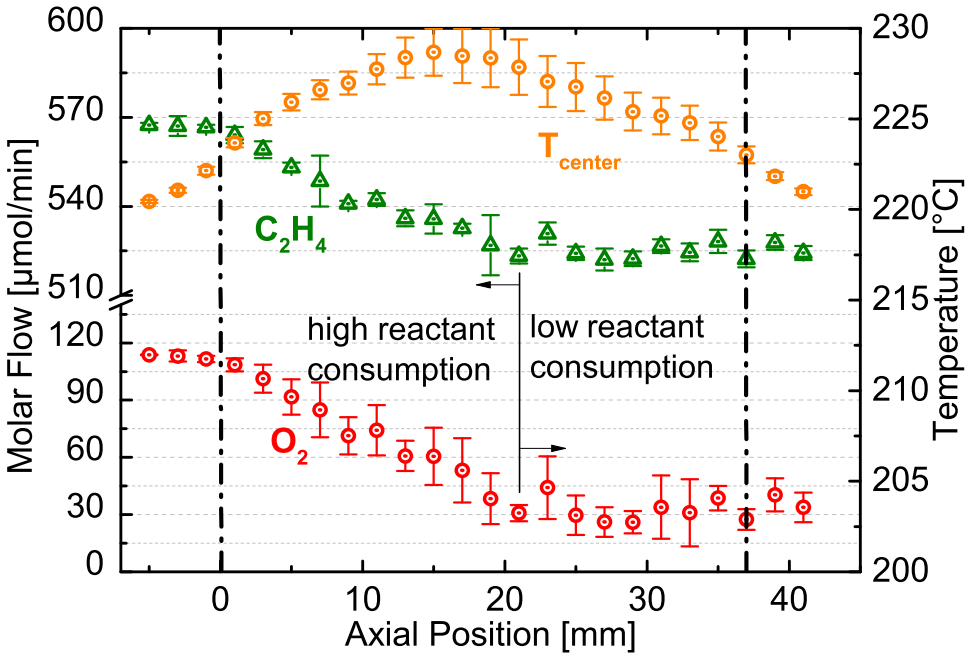
Molar Flow [µmol/min]
Temperature [°C]
Axial Position [mm]
C2H4
O2
T center
high reactant consumption
low reactant consumption

(a)

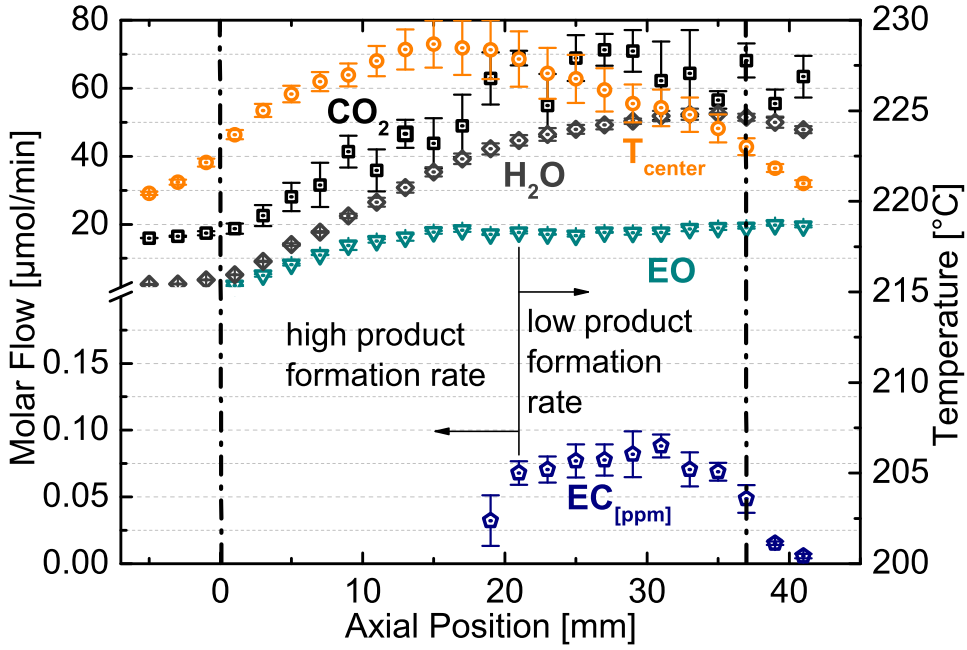
Molar Flow [µmol/min]
Temperature [°C]
Axial Position [mm]
CO2
H2O
T center
EO
EC[ppm]
high product formation rate
low product formation rate

(b)

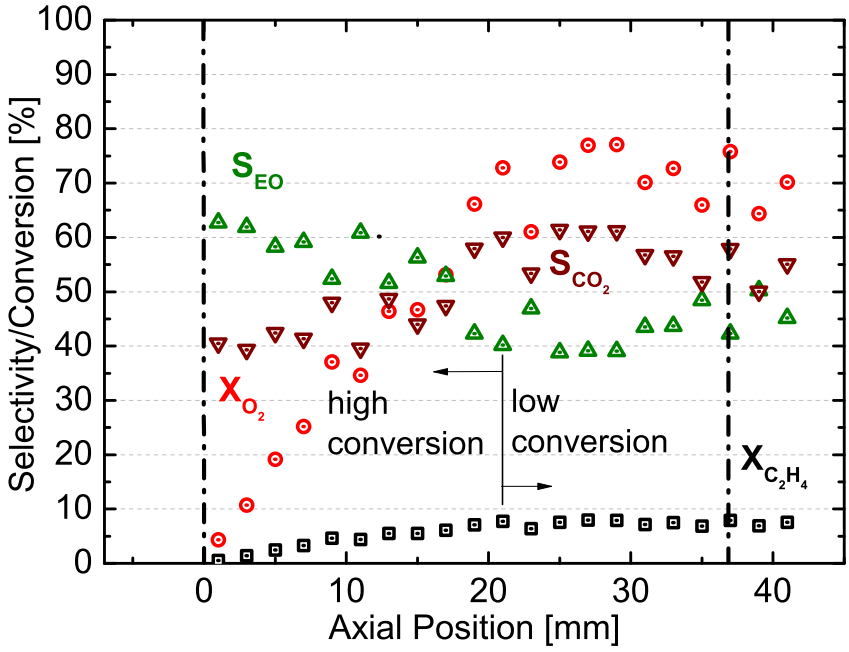

(c)

Figure 5.13: CPR profiles at GHSV = 4750 h^{-1}, 225 °C heating block temperature, and 17 bara pressure without DCE cofeeding. Profile measurement from inlet to outlet. (a) educt profiles and temperature, (b) product profiles, (c) conversion of oxygen and ethylene and selectivities to EO and CO_2.

Ethylene and oxygen are consumed rapidly (Figure 5.13a) until conversion levels off at about 21 mm. In comparison to the first profile measurements without feeding DCE shown in Figure 5.12, the position at which reactant conversion levels-off has shifted from 13 mm to 21 mm, showing the gradual removal of surface chlorine with time on stream if there is no DCE in the feed. From 21 mm onward, reactant conversion and product formation slow down significantly. In line with the extended reaction zone, the hot spot shifted further down the catalyst bed to about 17 mm. The temperature curve takes on a distinct bell-like shape. Temperature increases as long as reactants are converted and decreases after the hot spot when reactant conversion stops. The EO profile in Figure 5.13b shows a plateau beginning from 17 mm until the end of the bed. While H_2O increases further until the end of the bed, CO_2 seems to stop to increase at 21 mm. Only EC, the primary chlorine removal product, could still be detected in subppm amounts in this experiment. The position from which EC was still detected (19 mm) matches almost exactly with the position at which reactant conversion and formation of EO and CO_2 stopped (19 – 21 mm). This is another manifestation of the blockage of active silver sites by chlorine atoms which remain at the surface even hours after DCE feeding was interrupted or diffuse slowly from subsurface sites to be removed by the oxychlorination reaction [96]. VC could not be detected in this measurement any longer. As VC is most likely formed by oxidative dehydrogenation from EC according to eq. 5.38, its concentration is either below the GC detection limit, or the oxygen concentration is too low for eq. 5.38 to be effective anymore. While the selectivity toward EO decreases quickly in the absence of surface chlorine from 60 to 40 % (Figure 5.13c, CO_2 increases accordingly), it increases again

slightly from 21 mm until the end of the catalyst bed due to the selectivity enhancing effect of the remaining surface chlorine.

5.2.4 Spatially Resolved Kinetic Measurements

Axial and Radial Dispersion

In order to choose the appropriate model for the profile fitting, the criteria for axial and radial dispersion were evaluated. Radial dispersion is negligible when catalyst bed gradients are absent since heat-transfer limitation dominate in radial direction. As shown in Chapter 5.2.1 catalyst bed gradients can be neglected for the profile measurements in the CPR and thus also the radial dispersion in the model for the parameter fitting.

According to eq. 2.54 axial dispersion can be neglected in the model as well, when the evaluation of the criterion is below 0.05. The parameters used in the criterion are listed in Table 5.7. Applying eq. 2.54 with the reaction order of one with regards of

Table 5.7: Parameters for Diagnostic Evaluation of the Presence of Axial Dispersion.

Parameter	Value	Unit
u_0	$5.4 \cdot 10^{-3}$	$\mathrm{m} \cdot \mathrm{s}^{-1}$
$c_{i,0}$	29.03	$\mathrm{mol} \cdot \mathrm{m}^{-3}$
D_{ax}	$2.6 \cdot 10^{-6}$	$\mathrm{m}^2 \cdot \mathrm{s}^{-1}$
ρ_f	11.63	$\mathrm{kg} \cdot m^{-3}$
cp_f	1429.7	$\mathrm{J} \cdot \mathrm{kg}^{-1} \cdot \mathrm{K}^{-1}$
λ_{ax}	0.36	$\mathrm{W} \cdot \mathrm{m}^{-1} \cdot \mathrm{K}^{-1}$

the reaction order of the limiting species (O_2) gives the following result:

$$\left| \frac{13.4 \cdot 10^{-4}}{1.67} - \frac{19.97 \cdot 2.53 \cdot 10^{-4}}{0.2} \right| < 0.05 \tag{5.40}$$

$$0.02 < 0.05 \tag{5.41}$$

For the spatial profile fitting the 1D pseudohomogeneous plug-flow model was chosen, resulting of the criteria described in Chapter 2.4.1 and the results of eq. 5.37 and 5.40.

CPR Profile Fitting

The profile measurements were conducted in a stainless steel reactor (1.4571) to mimic the industrial conditions including wall material. The applicability of the CPR for kinetic measurements was tested by measuring profiles in the CPR at different reaction conditions. Using the CPR, near isotherm profile measurements over the entire fixed-bed can be conducted. Due to the low amount of catalyst employed, less heat evolves during the reaction. Thus, profile measurements using the CPR can be used to determine kinetic parameters by fitting the measured concentration and temperature profiles. Kinetic information for conversions higher 5 % can be obtained which is an advantage compared to a common differential reactor. For that purpose profiles were measured at three different reaction conditions. The results for the parameter fitting of the CPR profiles for eq. 5.23, 5.24 and 5.28 are summarized in Table 5.8. For all profile measurements in the CPR (Figure 5.14 - 5.16), the reaction temperature in the

beginning of the bed was still approaching the wall temperature; that is why, the temperature was also taken into account for the parameter fitting process. The activation energies determined from initial rate measurements were taken as starting conditions for the profile regression.

From profile regression, it can be seen that the proposed reaction rate expressions derived from the dual-site mechanism fit the temperature and concentration profiles inside the CPR well. In the beginning of the bed, the fitted temperature is in all the three measurements slightly higher than the measured values, and the temperature profile develops too steeply. This is because axial dispersion of heat was neglected in the model, according to the results of the axial dispersion criteria of eq. 5.40 in Chapter 5.2.4 and the slope of the temperature profile was obtained from a plug flow heat balance (eq. 2.59). Because the absolute temperature deviation between the experiment and model is very small (<3 K) and the inclusion of axial heat conduction would turn eq. 2.59 into a second-order ODE with the effective axial thermal conductivity as unknown model parameter, the more simple plug flow heat balance was retained. The measured temperature profile is damped by the heat conduction in the wall of the stainless steel capillary in which the thermocouple was sitting. Overall, this dampening effect is small since the temperature gradient over the entire catalyst bed is small and the measured temperature is to a large extent determined by the sampled gas stream flowing around the thermocouple tip. More accurate temperature profiles could have been measured by using a fused silica capillary instead of a stainless steel capillary and a pyrometer fiber collecting the infrared radiation directly from the catalyst instead of a thermocouple. However, in the present application, stainless steel capillaries had to be used because the hard corundum catalyst support leads to repeated breaking of fused silica capillaries.

Figure 5.14 shows the profile fitting for GHSV = 4750 h^{-1} and a heating block temperature of 200 °C with 1.25 ppm DCE in the feed. All fitted species profiles show a good agreement at 200 °C, all being within error bars. The decrease of DCE is also captured well. The VC and EC profiles cannot be modeled with the current model because VC is formed on the one hand from DCE according to eq. 2.51 and on the other hand in an unknown proportion by oxidative dehydrogenation of EC according to eq. 5.38. Upon closer inspection, it can be seen that the measured profiles level-off from about 26 mm onward due to blockage of silver sites by chlorine, whereas the fitted profiles show a monotonous decrease for the reactants and a monotonous increase for the products throughout the entire catalyst bed. This is because eqs. 5.23, 5.24 and 5.28 represent a Langmuir-Hinshelwood model in which the active site density is fixed and encoded in the respective rate constants (fit parameters A_k, $k^0_{DCE,j}$). Also, the adsorption-desorption equilibria of the various species blocking active sites are modeled by simple Langmuir-isotherms, which means without coverage-dependent heats of adsorption (fit parameters $\Delta H_{i,j}$). It is not possible with this type of kinetic model to include the loss of active surface sites by irreversible blockage of silver atoms with chlorine and to capture the fine details of the competing adsorption of oxygen and chlorine depending on coverage. At higher temperatures of 210 and 225 °C but otherwise identical conditions (Figures 5.15 and 5.16, respectively), the fitted profiles of C_2H_4, O_2, EO, CO_2, H_2O, and DCE show again good agreement with the experimental profiles except for the leveling-off of the profiles once all active silver sites are blocked by chlorine.

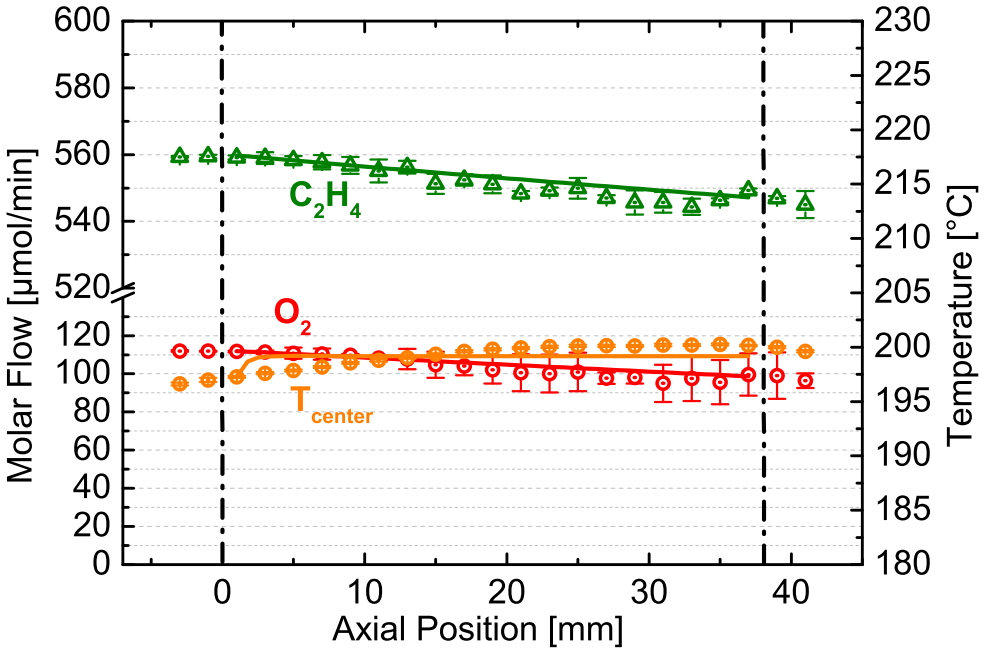

(a)

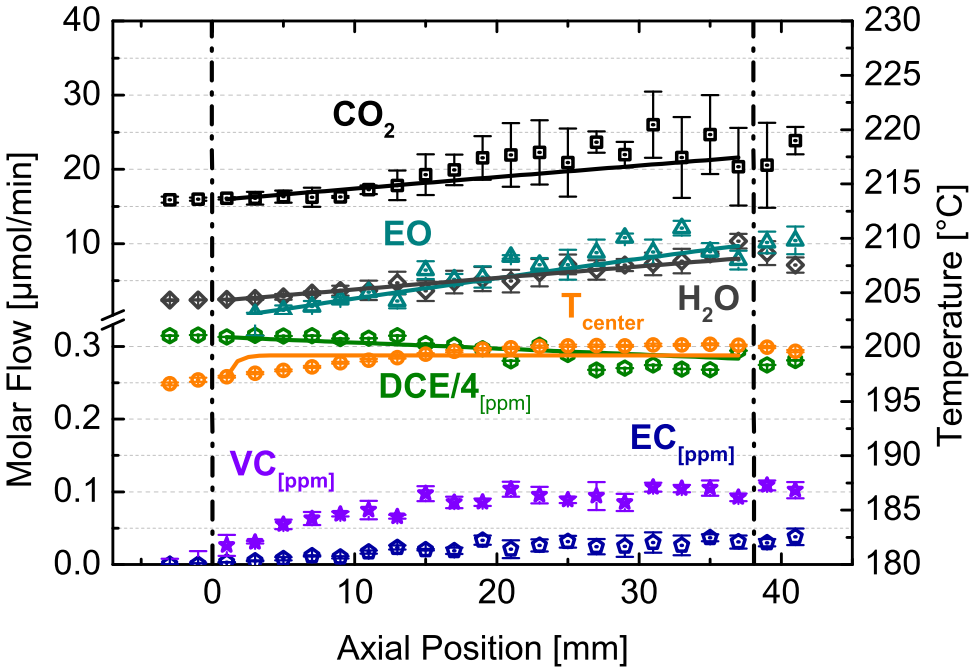

(b)

Figure 5.14: CPR profiles fitted at GHSV = 4750 h^{-1}, 200 °C heating block temperature, 17 bara pressure and 1.25 ppm DCE concentration in the feed. (a) educt profiles, (b) product profiles. The lines represent the resulting fitting, the discrete points represent measurements.

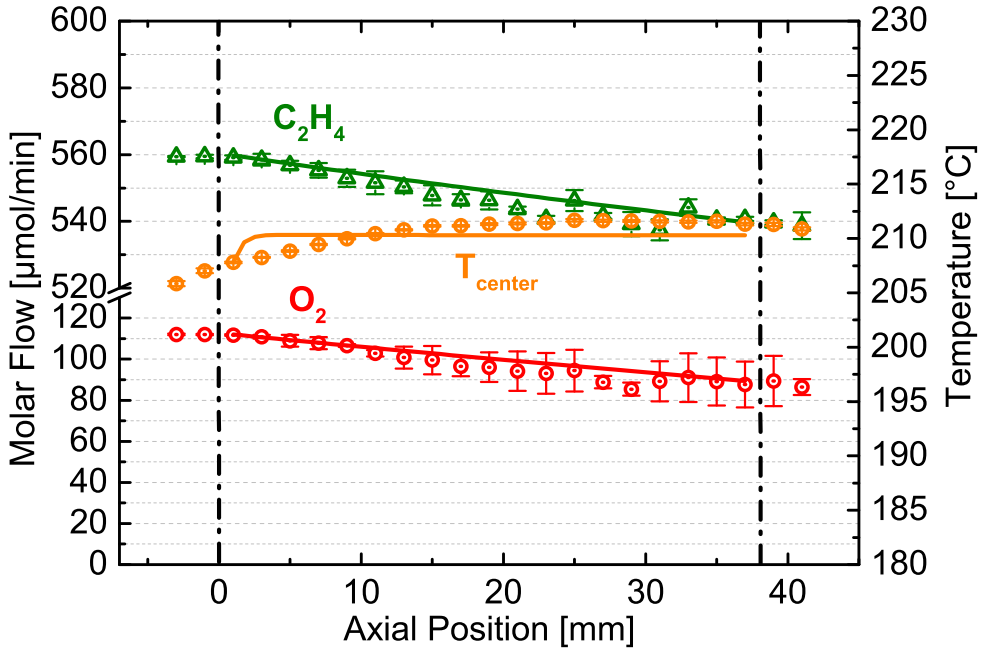

(a)

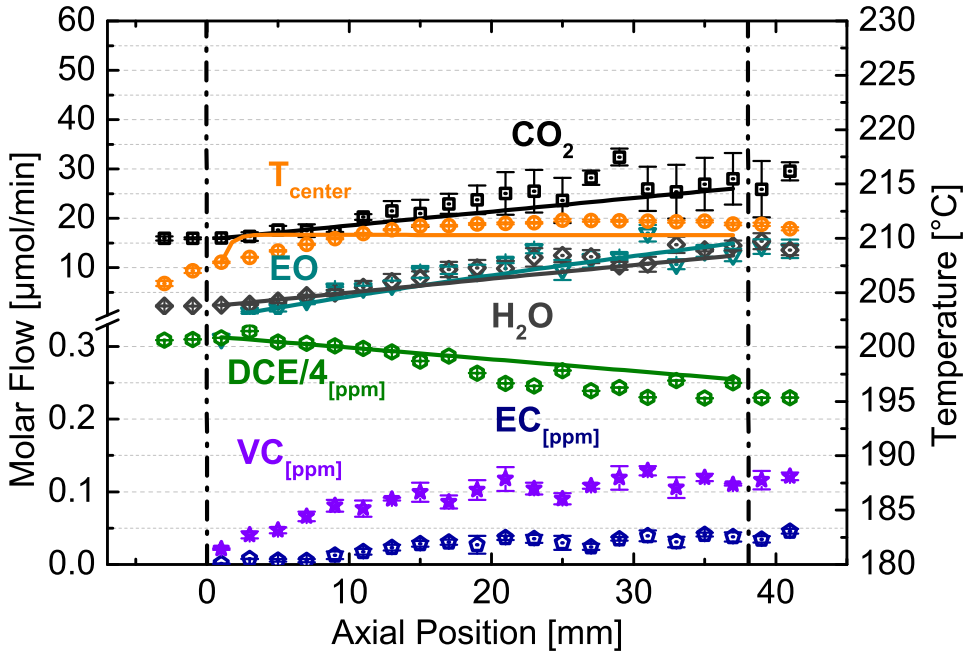

(b)

Figure 5.15: CPR profiles fitted at GHSV = 4750 h^{-1}, 210 °C heating block temperature, 17 bara pressure and 1.25 ppm DCE concentration in the feed. (a) educt profiles, (b) product profiles. The lines represent the resulting fitting, the discrete points represent measurements.

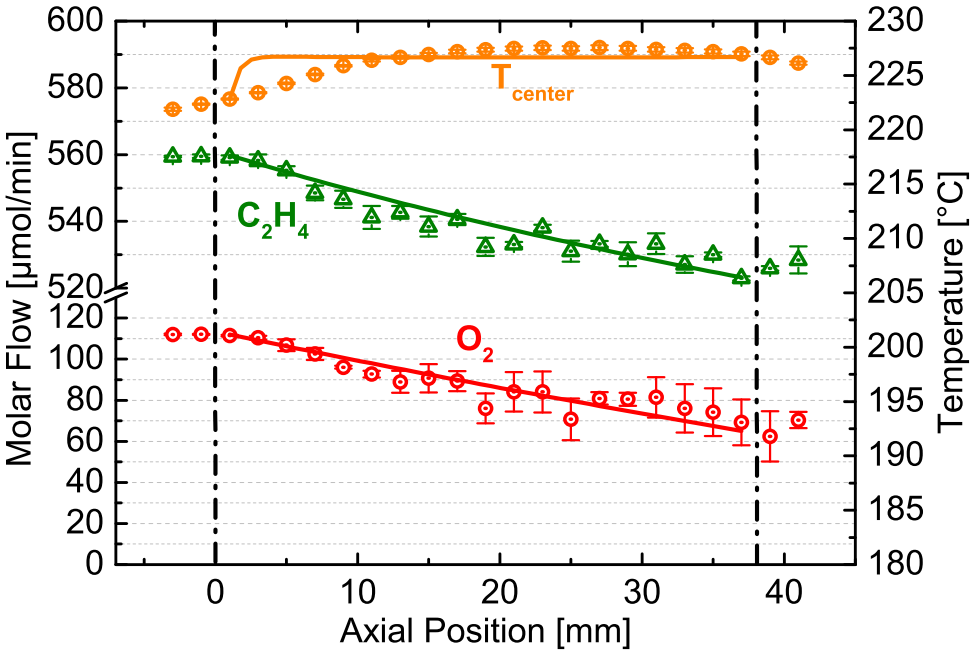

(a)

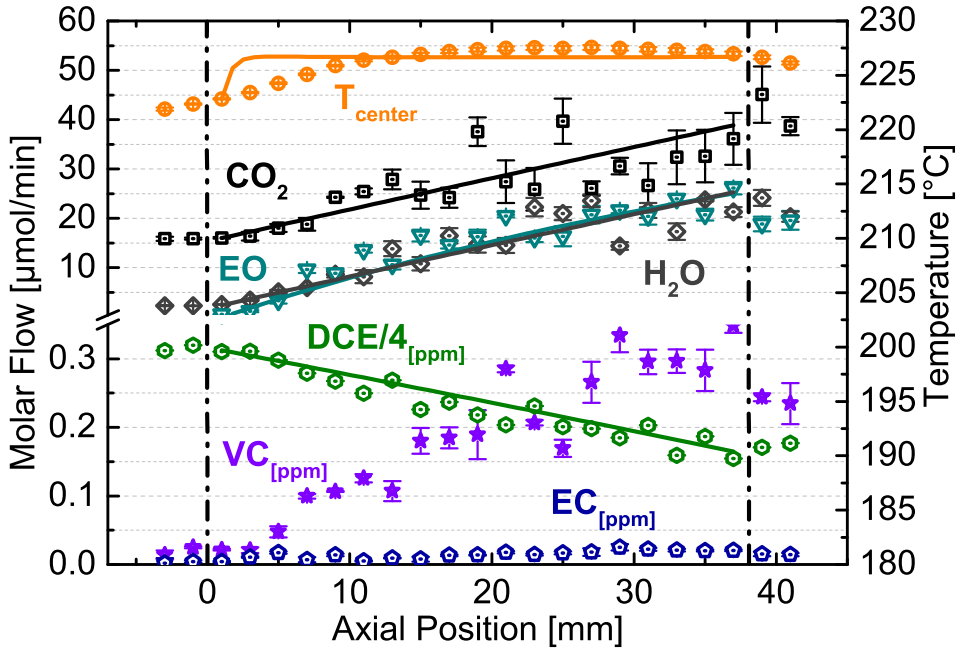

(b)

Figure 5.16: CPR profiles fitted at GHSV = 4750 h^{-1}, 225 °C heating block temperature, 17 bara pressure and 1.25 ppm DCE concentration in the feed. (a) educt profiles, (b) product profiles. The lines represent the resulting fitting, the discrete points represent measurements.

Table 5.8: Kinetic Parameter Determined by Regression of Profiles Measured in the CPR Using the Levenberg-Marquardt Solver Algorithm in ComSol 5.5^{TM}.

Parameter	Value	Confidence (95 %)	Unit
A_{EO}	$3.54{\cdot}10^{6}$	$\pm$ 0.05 $\cdot 10^{6}$	mol $\cdot$ kg^{-1} $\cdot$ s^{-1}
Ea_{EO}	74.30	$\pm$ 0.23	kJ $\cdot$ mol^{-1}
A_{CO_2}	2.78 $\cdot 10^{5}$	$\pm$ 0.16 $\cdot 10^{5}$	mol $\cdot$ kg^{-1} $\cdot$ s^{-1}
Ea_{CO_2}	76.10	$\pm$ 2.97	kJ $\cdot$ mol^{-1}
$A_{C_2H_4,AgO_{sub}}$	7.68 $\cdot 10^{-3}$	$\pm$ 0.89 $\cdot 10^{-3}$	bar^{-1}
$\Delta H_{C_2H_4,AgO_{sub}}$	-19.79	$\pm$ 1.58	kJ $\cdot$ mol^{-1}
$A_{O_2,Ag_{step}}$	174.40 $\cdot 10^{-3}$	$\pm$ 13.61 $\cdot 10^{-3}$	bar^{-1}
$\Delta H_{O_2,Ag_{step}}$	-19.93	$\pm$ 1.25	kJ $\cdot$ mol^{-1}
$A_{O_2,AgO_{sub}}$	0.62 $\cdot 10^{-3}$	$\pm$ 0.12 $\cdot 10^{-3}$	bar^{-1}
$\Delta H_{O_2,AgO_{sub}}$	-15.89	$\pm$ 1.08	kJ $\cdot$ mol^{-1}
$A_{CO_2,AgO_{sub}}$	28.52 $\cdot 10^{-3}$	$\pm$ 3.81 $\cdot 10^{-3}$	bar^{-1}
$\Delta H_{CO_2,AgO_{sub}}$	-23.67	$\pm$ 4.24	kJ $\cdot$ mol^{-1}
$A_{CO_2,Ag_{step}}$	29.86 $\cdot 10^{-3}$	$\pm$ 6.22 $\cdot 10^{-3}$	bar^{-1}
$\Delta H_{CO_2,Ag_{step}}$	-20.68	$\pm$ 7.19	kJ $\cdot$ mol^{-1}
$A_{DCE,AgO_{sub}}$	95.58	$\pm$ 6.90	bar^{-1}
$\Delta H_{DCE,AgO_{sub}}$	-20.13	$\pm$ 0.13	kJ $\cdot$ mol^{-1}
$A_{DCE,Ag_{step}}$	84.01	$\pm$ 3.23	bar^{-1}
$\Delta H_{DCE,Ag_{step}}$	-40.01	$\pm$ 2.03	kJ $\cdot$ mol^{-1}
$k^0_{DCE,Ag_{step}}$	5.49 $\cdot 10^{2}$	$\pm$ 0.26 $\cdot 10^{2}$	mol $\cdot$ kg^{-1} $\cdot$ s^{-1}
$Ea_{DCE,Ag_{step}}$	90.41	$\pm$ 3.47	kJ $\cdot$ mol^{-1}
$k^0_{DCE,AgO_{sub}}$	52.82 $\cdot 10^{2}$	$\pm$ 2.15 $\cdot 10^{2}$	mol $\cdot$ kg^{-1} $\cdot$ s^{-1}
$Ea_{DCE,AgO_{sub}}$	106.06	$\pm$ 2.34	kJ $\cdot$ mol^{-1}

As a result of the reparametrization the correlation between the parameters is low as can be seen in Table A.1-A.3 in Section A.2.

5.3 Pilot Scale Profile Reactor Simulation

5.3.1 Axial and Radial Dispersion

Evaluating eq. 2.30 decides which model has to be used for the Pilot Scale Profile simulations, the used parameters for the criteria are listed in Table 5.9. For the particle diameter the worst case was considered assuming that all particles have a diameter of 900 µm. The result of eq. 5.42 shows that radial dispersion cannot be neglected for the PSPR simulation leading to the requirement of a 2D pseudohomogeneous simulation accounting for the radial dispersion in the model. The used model accounted for both the radial as well as the axial dispersion.

$$|\gamma_w \cdot \beta_w \cdot B_w| = |21.300 \cdot 0.024 \cdot 0.187| = 0.1 \not< 0.05 \tag{5.42}$$

Table 5.9: Parameters for Diagnostic Evaluation of the Presence of Radial Dispersion.

Parameter	Value	Unit
$r_{V,obs}$	0.26	$mol \cdot m^{-3} \cdot s^{-1}$
d_p	900	µm
T_w	467	K
$\lambda_{bed,eff}$	0.14	$W \cdot m^{-1} \cdot K^{-1}$
d_t	15	mm
$Bi_{h,w}$	0.19	-

5.3.2 2D Pseudohomogeneous Profile Simulation

For validating the kinetic model derived in Chapter 5.1.4, species flow rate and temperature profiles measured in the PSPR and simulated with a 2D pseudohomogeneous model (Chapetr 2.4.4). The rate laws and kinetic parameters from the regression of the CPR profiles (Chapter 5.2.4) were used. Measurements and simulations were performed for a DCE concentration in the feed of 1.53 and 3.18 ppm, respectively, with the rest of the feed being identical to that presented in Table 4.2. A GHSV of 4750 h^{-1} was chosen, the reactor pressure was set to 17 bara, and the cooling fluid temperature of 194 °C was chosen for the validation case. The remaining results of the PSPR profile measurements with temperature, DCE, and CO_2 concentration variations were not used for the validation and can be seen in the appendix in Chapter A.3.

Figure 5.17 shows measurements (symbols) and simulations (solid lines) for 1.53 ppm DCE in the feed. Apart from the last datapoint which is disturbed by mixing behind the catalyst bed, the reactants, C_2H_4 and O_2, as well as the inhibitor, DCE, are monotonously converted along the entire catalyst bed. Accordingly, the reaction products EO, CO_2, H_2O, and VC, are monotonously produced along the entire catalyst bed. A sudden slow down or even stop of reactant conversion and product formation due to the blockage of active silver sites by chlorine as observed in the CPR does not occur in the PSPR under these conditions. In fact, the opposite is true. While reactant conversion and product formation are rather slow up to 340 mm into the bed ($X_{O_2} \approx 8$ % and $X_{C_2H_4} \approx 3$ %), the reaction rates increase noticeably beyond this point reaching $X_{O_2} \approx 20$ % and $X_{C_2H_4} \approx 8$ % at the end of the catalyst bed. As can be seen in the temperature profile, this sudden increase of reaction rates at 340 mm is a thermal effect. Due to the larger inner diameter of the PSPR compared to that of the CPR (15 vs. 4 mm ID), the PSPR is more prone to thermal runaway. The highest heat-transfer resistance in catalytic fixed-bed reactors is inside the catalyst bed, and the more heat a reaction produces and the larger the diameter of the catalyst bed is, the higher is the risk for thermal runaway. For 1.53 ppm DCE, the highest temperature of the cooling fluid at which the PSPR could still be operated was in fact 194 °C. Only 0.5 °C higher cooling temperature led to thermal runaway. Due to the low temperature in the catalyst bed before the "light-off" point at 340 mm ($T \leq 205$ °C), chlorine deposition onto the silver surface is very inefficient, as can be seen from the DCE and VC profiles. Until 340 mm, almost no DCE is converted, and very little VC is formed. The fact that no EC could be detected at all indicates that the silver surface has a high oxygen coverage, leading to immediate oxidative dehydrogenation of EC, which is the primary product of chlorine removal, such that only VC is leaving the surface formed by eq. 2.51 and eq. 5.38. At the "light-off" point at 340 mm, the rate of heat production becomes substantially greater than the rate of heat removal, in particular,

because the silver surface is not yet sufficiently covered with chlorine. The insufficient chlorine coverage leads to a selectivity shift toward more exothermic CO_2 production as can be seen in the selectivity profiles of EO and CO_2 which decrease/increase faster from 340 mm onward (Figure 5.17c). This releases even more reaction heat fueling thermal runaway ($-1327\ \mathrm{kJ \cdot mol^{-1}}$ for CO_2 vs. $-105\ \mathrm{kJ \cdot mol^{-1}}$ for EO) [148].

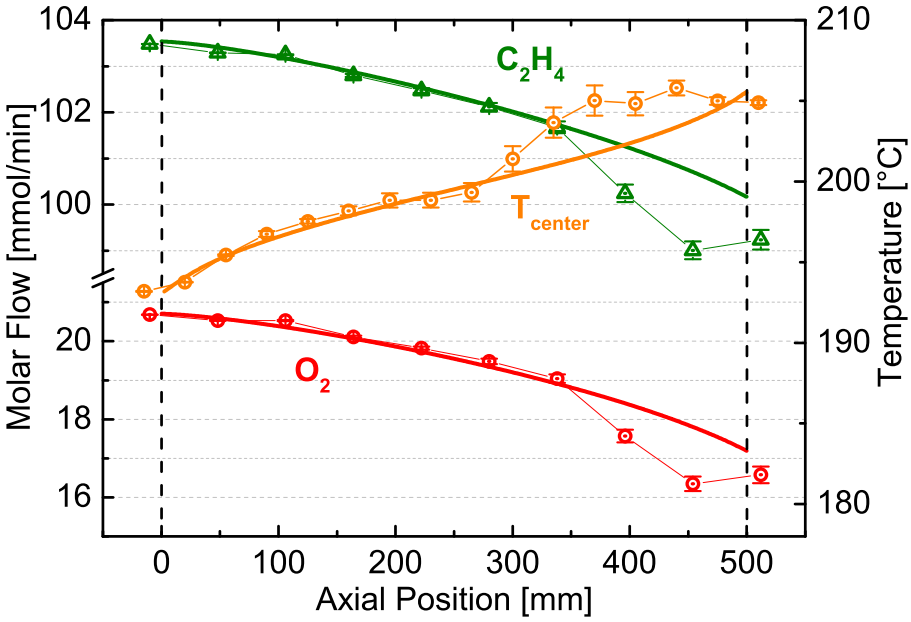

(a)

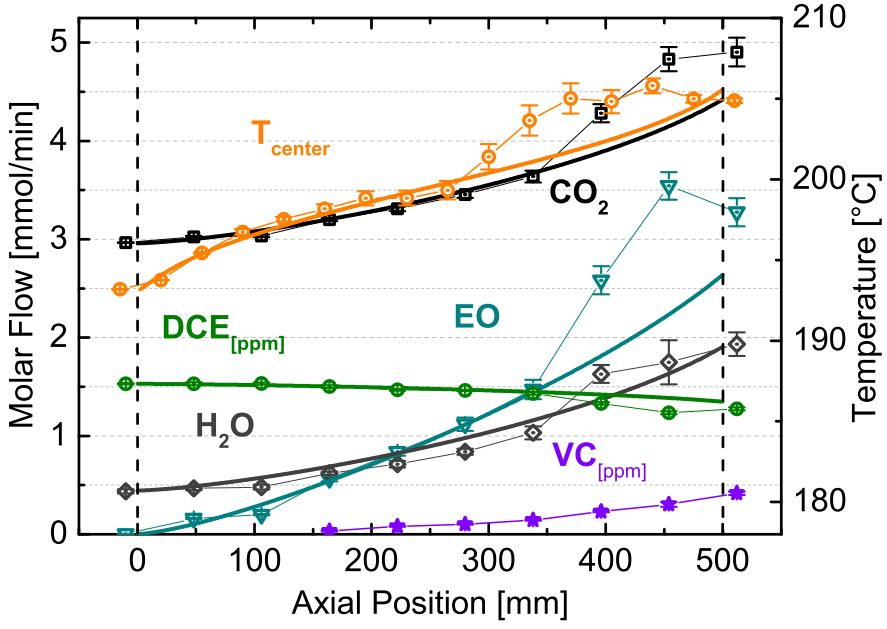

(b)

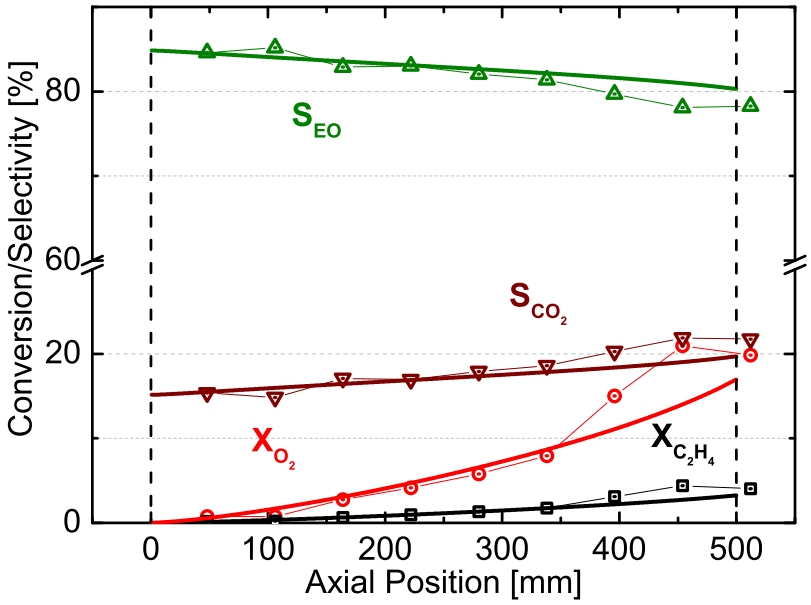

(c)

Figure 5.17: Pilot reactor profiles at GHSV = 4750 h^{-1}, 194 °C temperature of the heat-transfer fluid, 17 bara pressure, and 1.53 ppm DCE concentration in the feed. Discrete points were measured; the compact lines show simulation results by applying the measured kinetic parameters. Reactants and temperature (a), products (b) and conversion and selectivity (c).

From 340 mm onward, the increasing catalyst temperature spurs chlorine deposition onto the silver surface as can be seen from the decreasing DCE profile and the increasing VC profile, but it is too late; the thermal runaway has set in. The kinetic model developed in Chapter 5.1.4 captures the species and temperature profiles quite accurately up to the "light-off" point at 340 mm. The model also predicts a nonlinear increase in reaction rates and temperature toward the end of the catalyst bed, which is qualitatively correct; however, the model underestimates how sudden the slopes change at 340 mm.

A second measurement was done in the PSPR, this time at a doubled DCE concentration in the feed of 3.18 ppm. The results are shown in Figure 5.18. Doubling the DCE concentration in the CPR from 1.25 to 2.50 ppm caused basically a shutdown of all catalytic reactions due to coverage of all active silver sites with chlorine (cp. Figures 5.10 vs. 5.11), whereas doubling the DCE concentration in the PSPR from 1.53 to 3.18 ppm had almost no effect, at least not up to the "light-off" point, which was again at almost the same position at 340 mm. The reason for this different behavior is the overall lower temperature of the catalyst bed. While the CPR was not prone to thermal runaway due to efficient heat removal from the slender catalyst bed (4 mm inner diameter) and could be operated at temperatures above 220 °C where chlorine deposition was effective, the larger PSPR (15 mm inner diameter) could only be operated up to 194 °C cooling medium temperature. If the cooling medium temperature was set only 0.5 °C higher, thermal runaway occurred.

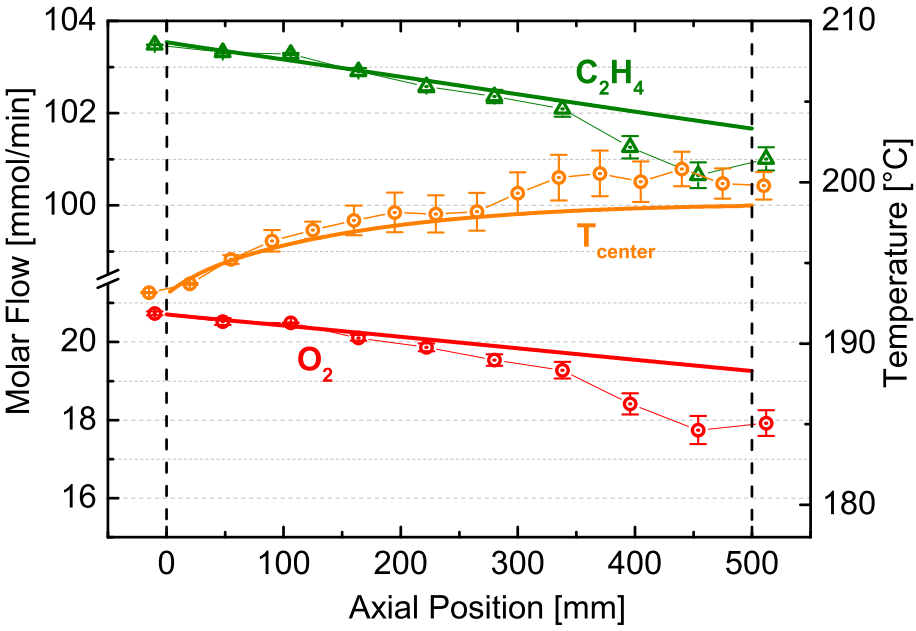
104
102
100
20
18
16
210
200
190
180
Molar Flow [mmol/min]
Temperature [°C]
0
100
200
300
400
500
Axial Position [mm]
C2H4
Tcenter
O2

(a)

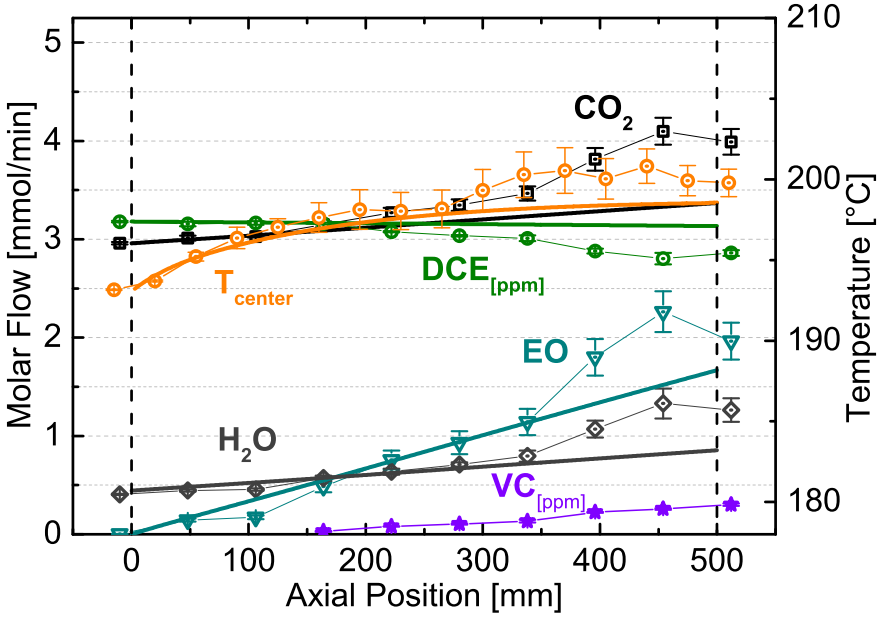
5
4
3
2
1
0
210
200
190
180
Molar Flow [mmol/min]
Temperature [°C]
0
100
200
300
400
500
Axial Position [mm]
CO2
Tcenter
DCE[ppm]
EO
H2O
VC[ppm]

(b)

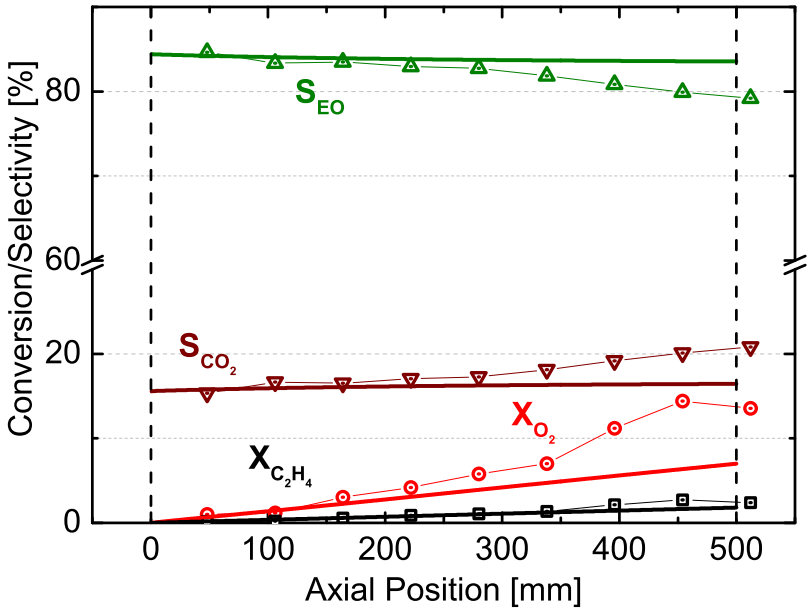

(c)

Figure 5.18: Pilot reactor profiles at GHSV = 4750 h^{-1}, 194 °C temperature of the heat-transfer fluid, 17 bara pressure, and 3.18 ppm DCE concentration in the feed. Discrete points were measured; the compact lines show simulation results by applying the measured kinetic parameters. Reactants and temperature (a), products (b) and conversion and selectivity (c).

At these low temperatures, chlorine deposition onto the silver surface was not effective yet as can be seen in Figure 5.18b. Despite doubling the DCE concentration to 3.18 ppm, almost no DCE is converted, and no VC is formed before 340 mm. At 340 mm, the onset of thermal runaway can still be seen, but the reaction rates and the selectivity to CO_2 increase less strongly because the higher DCE concentration leads to a faster rise of the chlorine coverage of the silver surface, once temperature rises above the threshold temperature for chlorine deposition. An alternative explanation for the low reaction rate before the light off point at 340 mm would be that the silver surface is blocked by chemisorbed DCE and that the chlorine removal mechanism is not very efficient yet. This would be in line with the observation that doubling the DCE concentration from 1.53 to 3.18 has no effect because the surface is already saturated with DCE. As before, the reactor model reproduces the molar flow rate and temperature profiles fairly well up to 340 mm but is unable to capture the reactor light-off point correctly.

Summary and Conclusions

6

In this thesis the ethylene epoxidation reaction with cofeeding of 1,2-dichloroethane (DCE) was investigated under near industrial process pressure, temperature, and contact time using the profile measurement technique developed by Horn et al. [15]. The employed catalyst was an unpromoted supported split shape $Ag/\alpha - Al_2O_3$ with a silver loading of 14.5 wt-% provided by BASF SE [136]. In order to derive a reaction rate expression and to determine intrinsic kinetic parameters, a differentially operated fixed-bed reactor was designed and constructed which could be operated at industrial relevant pressure of 17 bara and a temperature range of $50 - 550$ °C with an isotherm reaction zone heated by a fluidized sand-bath. By operating the kinetic test reactor gradient free, kinetic parameters could be determined directly from product formation rates. Feed gas composition was close to industrial conditions with a C_2H_4/O_2 ratio of 5 and cofeeding of 1 vol-% of CO_2 and 0.15 vol-% of H_2O to mimic industrial conditions. In order to see the effect of promotion by cofeeding halogenated hydrocarbons, DCE was added in ppm amounts. From initial reaction rate measurements in which all concentrations were kept constant and only one species concentration was varied, was concluded that at high C_2H_4/O_2 ratios the effect of C_2H_4 concentration on the reaction rate is minor due to the excess concentration of C_2H_4 in the feed. CO_2 has a slightly negative effect by occupying active sites responsible for both, selective and unselective reactions. With increasing O_2 partial pressure, both reaction rates for selective and unselective reaction increase giving a reaction order of $+1$, while DCE cofeeding decreased the catalyst activity dramatically, and increasing the selectivity toward EO with a reaction order of -1 for both reactions. From these results can be seen that despite the vastly different concentrations of their molecular precursors in the feed, O_2 at 7 vol-% and DCE at $1 - 3$ ppm, O and Cl compete for the same active silver sites. Activation energy measurements at two different DCE concentrations gave an increasing activation energy with increasing DCE concentration for both, the selective and unselective reaction. Thereby, increasing the activation energy for the CO_2 formation more than for EO formation.

To gain information about the reaction mechanism, profile measurements in a Compact Profile Reactor (CPR), developed by Reacnostics GmbH, were conducted [17]. The CPR uses the profile technique based on the development by Horn et al. [15] with a capillary mounted in the center of the catalyst bed and sampling reaction gas mixture via a laser drilled orifice in the wall of the capillary. The capillary sampling position is adjusted by moving the reactor brass block in which the fixed-bed reactor is mounted and heated using a slide on which the block is attached and moved by a stepper motor in micro meter resolution while the capillary is statically mounted on both sides. With such a configuration, concentration and temperature profiles at industrial pressure and temperature conditions can be measured minimizing radial gradients by small reactors and utilizing only little of the catalyst. The measurements were performed at 17 bara, reaction temperatures in a range of $180 - 225$ °C, two different contact times (GHSV=4750 h^{-1} and 9500 h^{-1}), and two different DCE feed concentrations (1.25 and

2.5 ppm). The sampling gas flow was adjusted to less than 5 % of the total flow by micro meter needle valves which were situated in a heated box to avoid condensation. All tubes to the reactor were heated as well as from the reactor to the GC to analyze the gas composition quantitatively. The employed catalyst was sieved to a fraction of $200 - 400$ µm to maintain plug flow behavior during the measurements. The profiles confirmed the competing behavior of O_2 and Cl. Chlorine is deposited on the silver surface by reaction of DCE with AgO to VC, AgCl, and H_2O. Chlorine removal occurs by oxychlorination of ethane being present in a concentration of some hundred ppm in the feed, leading to EC as a primary chlorine removal product. If the surface oxygen coverage is high, EC is quickly converted to VC by oxidative dehydrogenation, and VC is the only chlorine-containing product leaving the surface. With increasing O_2 conversion along the catalyst bed, Cl coverage increases, and fewer O atoms can adsorb on the active sites, slowing all catalytic surface reactions down, including i) the selective epoxidation reaction, ii) the unselective oxidation of C_2H_4 and EO to CO_2, iii) chlorine removal by oxychlorination of ethane, and iv) EC conversion to VC by oxidative dehydrogenation. The formation of products stops before reaching the end of the reaction zone although educts in sufficient concentrations are present. An EDX measurement of the stackwise extracted catalyst revealed an increasing chlorine content on the catalyst surface until the position at which the reactions stopped. This observation is of significant relevance for operation of industrial EO reactors with respect to efficient use of the catalyst inventory. Cofeeding DCE is mandatory to achieve high EO selectivity, but overinhibition is easily possible. If the DCE concentration in the feed is chosen only slightly too high, all reactions will shut down somewhere inside the catalyst bed, and significant parts of the catalyst inventory will not be used at all. If no DCE is fed at all or not enough, CO_2 formation has only a slightly higher activation energy than EO formation, and the initially high EO selectivity achieved at the inlet of the catalyst bed decreases quickly with increasing catalyst temperature. With increasing chlorine surface coverage, the activation energy for CO_2 formation increases much more strongly compared with the activation energy for EO formation, yielding higher EO selectivity at the expense of a reduced conversion.

Since in the species and temperature measurements in the CPR, radial gradients could be neglected, the profiles were well suited for kinetic parameter determination by profile regression. The derived LHHW rate law was based on the dual-site mechanism postulated by Schlögl [18]. The results of the differentially operated fixed-bed reactor measurements were used as initial values to fit the CPR profiles at different conditions. Concentration and temperature profiles were fitted simultaneously for all conditions to cover the complete measurement conditions. To validate the kinetic parameters a Pilot Scale Profile Reactor (PSPR) was designed and built that allowed the measurement of species and temperature profiles in a pilot scale. The reactor had an inner diameter of 15 mm and a total length of 1 meter in which a catalyst bed of up to 0.5 m could be tested. The sampling was realized with 10 static capillaries, which were mounted in the center of the catalyst bed, arranged equidistantly in axial direction. To measure temperature simultaneously, 16 K-type thermocouples (ø 250 µm) were placed in a liner in the center of the catalyst bed. Gas composition was analyzed quantitatively by two GCs for faster measurements. The sampling capillary was selected with a selector valve and guided to the GC with an automatic start of analysis. Extensive safety installations were equipped to run the reaction 24/7 unattended with inlet and outlet O_2 concentration as well as temperature monitoring and several alarm level. An over-flow valve in front and behind of the bed should release the reactor pressure in case of slow pressure increase. Fast rising pressure could be released by two rupture discs in case of thermal runaway.

In order to validate the measured kinetic parameters, profile simulations were performed using a two-dimensional pseudohomogeneous model. Dispersion in radial and axial direction was accounted using the Tsotsas [63] and Winterberg et al. [125] model (see Chapter 2.4.4). The simulation could predict the profile behavior very well, until the reaction rates accelerated with a changed selectivity at 340 mm in the bed which was a thermal effect given the larger inner diameter of the PSPR compared to the CPR (15 vs. 4 mm). The profile measurements reveal that the already delicate interplay between too much or too little DCE in the feed is further complicated by the requirement of a certain lower threshold temperature for chlorine deposition or chlorine removal to be effective and a certain upper temperature limit above which thermal runaway occurs if the feed hits a largely unchlorinated surface.

In summary the results of this work show the beneficial application of spatial profile reactors to investigate heterogeneously catalyzed reactions in fixed-bed reactors even at industrial conditions. Starting from isothermal differentially operated fixed-bed reactors to gain kinetic information to small scale profile reactors suitable to obtain profiles for kinetic parameter regression to validation of those parameters by measuring and simulating profiles of the reaction in large scale reactors. The profile reactors are a huge win to study complex reactions like the ethylene epoxidation reaction by investigating the influence of catalyst promotion resolving chlorine profiles in subppm level. Information from the former "black-box" can be used to knowledge based optimize the reactor and catalyst performance.

A

Appendix

A.1 GC-Calibration

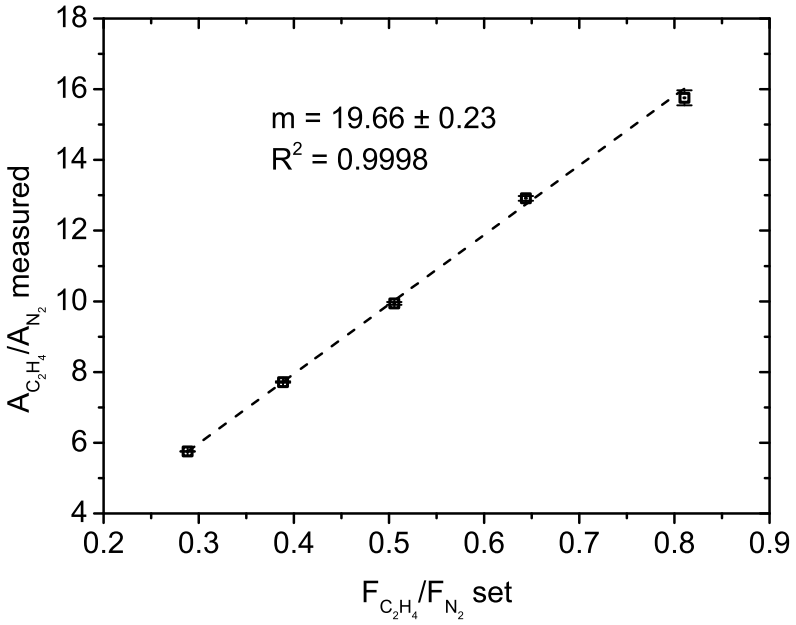

Figure A.1: GC Calibration for molar flow of C_2H_4 to N_2 adjusted to measured area ratio $A_{C_2H_4}/A_{N_2}$.

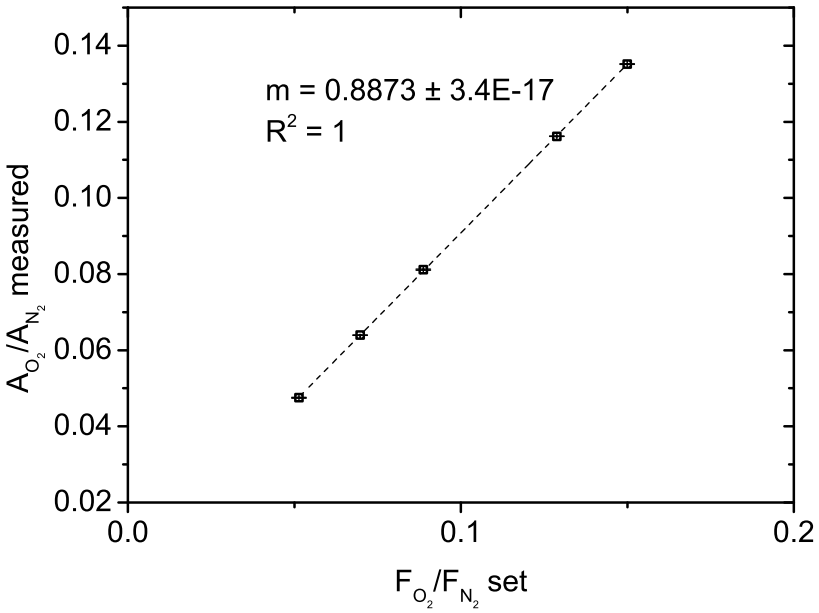

Figure A.2: GC Calibration for molar flow of O_2 to N_2 adjusted to measured area ratio A_{O_2}/A_{N_2}.

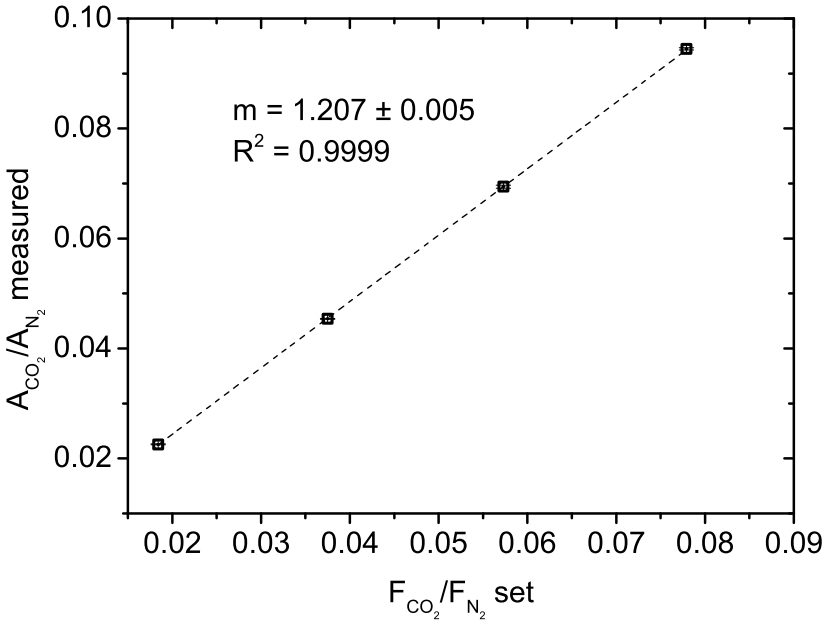

Figure A.3: GC Calibration for molar flow of CO_2 to N_2 adjusted to measured area ratio A_{CO_2}/A_{N_2}.

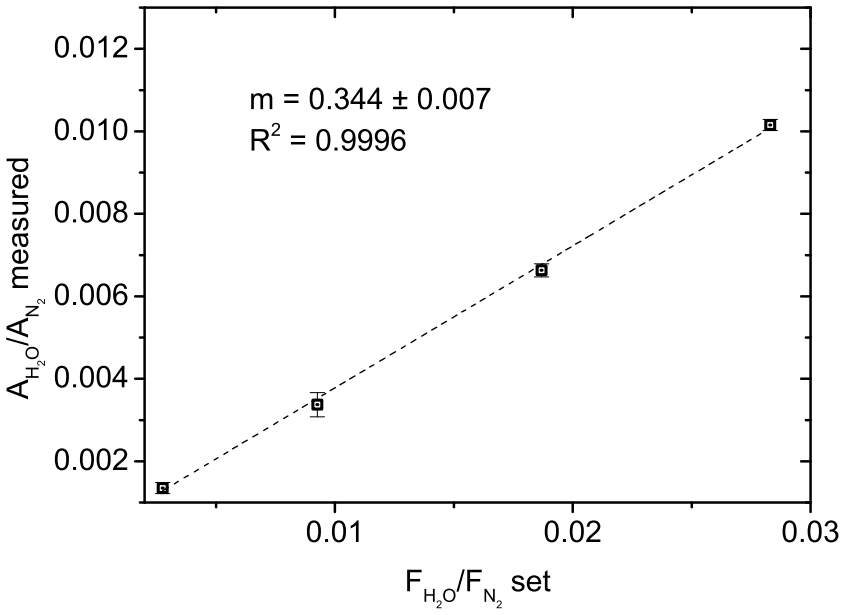

Figure A.4: GC Calibration for molar flow of H_2O to N_2 adjusted to measured area ratio A_{H_2O}/A_{N_2}.

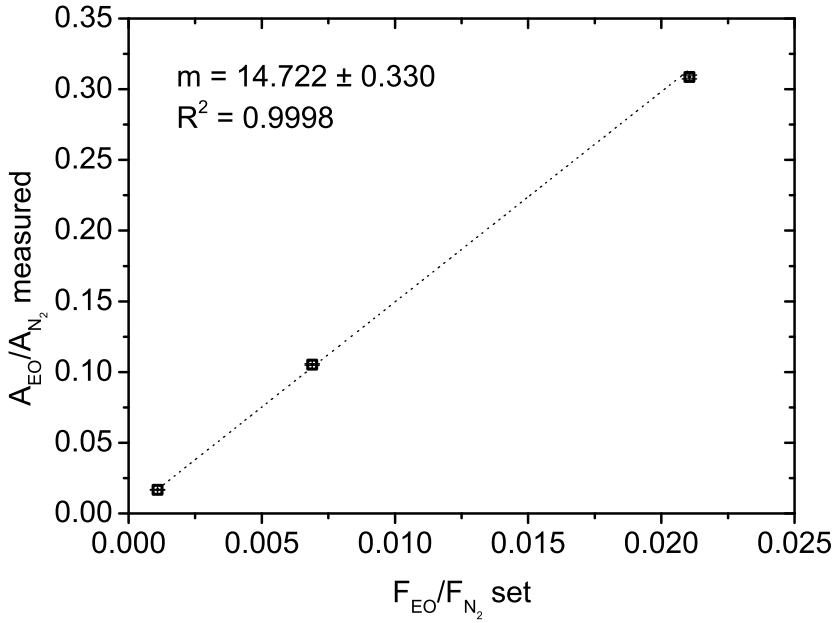

Figure A.5: GC Calibration for molar flow of EO to N_2 adjusted to measured area ratio A_{EO}/A_{N_2}.

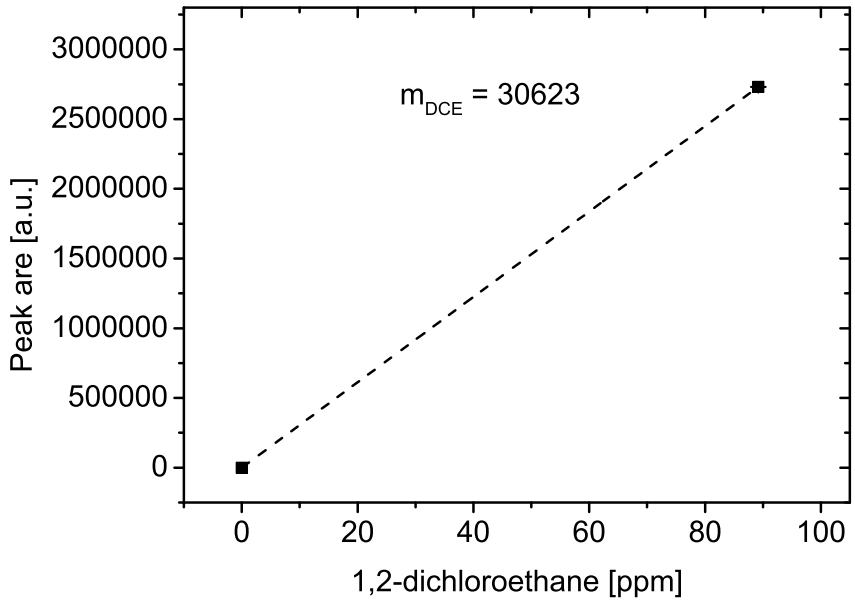

Figure A.6: GC Calibration for molar flow of 1,2-dichloroethane to N_2 adjusted to measured area ratio $A_{\mathrm{DCE}}/A_{\mathrm{N_2}}$.

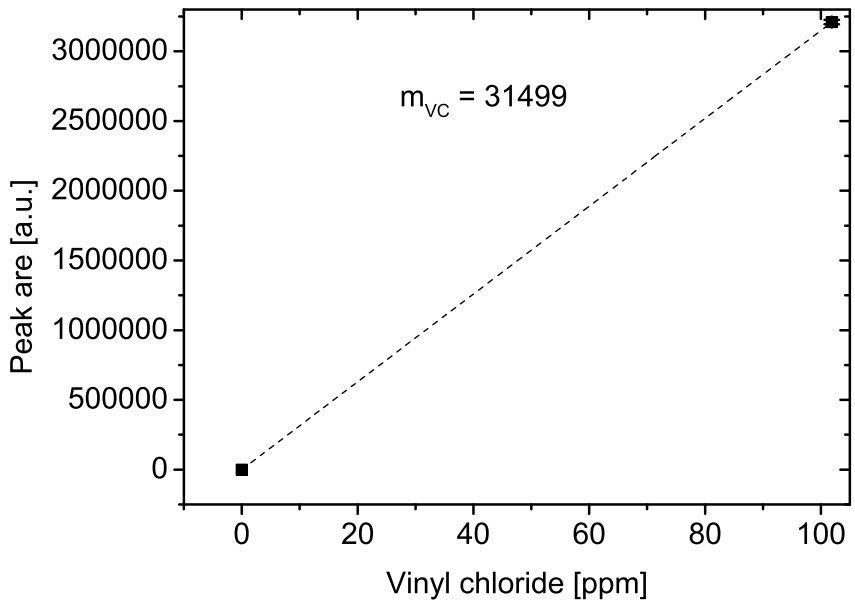

Figure A.7: GC Calibration for molar flow of vinyl chloride to N_2 adjusted to measured area ratio $A_{\mathrm{VC}}/A_{\mathrm{N_2}}$.

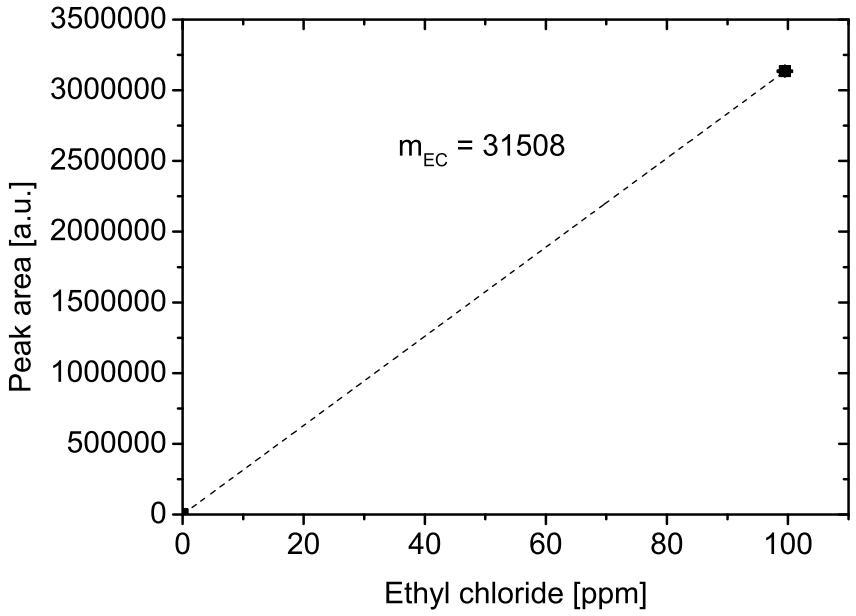

Figure A.8: GC Calibration for molar flow of ethyl chloride to N_2 adjusted to measured area ratio A_{EC}/A_{N_2}.

A.2 Correlation Matrix for Fitted Kinetic Parameters

Table A.1: Correlation of the Kinetic Parameters Determined by Regression of Profiles Measured in the CPR Using the Levenberg-Marquardt Solver Algorithm in ComSol 5.5^{TM} (Part 1).

Parameter	Ea_{EO}	Ea_{CO_2}	$\Delta H_{DCE,Ag_{step}}$	$\Delta H_{O_2,AgO_{sub}}$	$\Delta H_{CO_2,AgO_{sub}}$	$\Delta H_{C_2H_4,AgO_{sub}}$	$\Delta H_{DCE,AgO_{sub}}$
Ea_{EO}	1						
Ea_{CO_2}	-0.59	1					
$\Delta H_{DCE,Ag_{step}}$	0.62	0.11	1				
$\Delta H_{O_2,AgO_{sub}}$	-0.71	-0.45	-0.72	1			
$\Delta H_{CO_2,AgO_{sub}}$	0.22	0.43	0.00	-0.27	1		
$\Delta H_{C_2H_4,AgO_{sub}}$	-0.48	0.55	0.44	-0.80	0.40	1	
$\Delta H_{DCE,AgO_{sub}}$	0.05	0.52	0.17	-0.37	0.44	-0.62	1
$\Delta H_{O_2,Ag_{step}}$	0.77	-0.09	0.46	-0.64	0.21	0.70	-0.06
$\Delta H_{CO_2,Ag_{step}}$	0.00	0.12	-0.02	0.06	-0.11	-0.11	-0.10
$Ea_{DCE,AgO_{sub}}$	0.50	0.32	0.13	-0.60	0.08	-0.03	-0.59
$Ea_{DCE,Ag_{step}}$	0.00	0.43	0.26	0.27	0.02	0.36	0.06
A_{EO}	0.27	0.00	0.00	0.00	0.00	0.00	0.00
A_{CO_2}	-0.09	0.19	-0.01	-0.14	0.06	0.06	-0.16
$A_{DCE,Ag_{step}}$	-0.05	0.03	-0.03	-0.03	0.00	0.05	0.01
$A_{O_2,AgO_{sub}}$	0.24	0.00	0.00	0.00	0.00	0.00	0.00
$A_{CO_2,AgO_{sub}}$	-0.01	0.01	0.00	0.00	-0.02	0.00	-0.16
$A_{C_2H_4,AgO_{sub}}$	-0.19	0.00	0.00	0.00	0.00	0.00	0.00
$A_{DCE,AgO_{sub}}$	0.59	0.08	-0.07	0.05	0.03	0.18	0.04
$A_{O_2,Ag_{step}}$	0.33	-0.39	0.25	-0.56	-0.36	0.18	-0.62
$A_{CO_2,Ag_{step}}$	-0.06	0.12	-0.01	-0.07	-0.03	0.01	-0.67
$k^0_{DCE,AgO_{sub}}$	-0.01	0.04	0.00	0.04	0.02	-0.02	0.07
$k^0_{DCE,Ag_{step}}$	-0.43	0.18	-0.12	-0.66	-0.26	0.30	-0.31

Table A.2: Correlation of the Kinetic Parameters Determined by Regression of Profiles Measured in the CPR Using the Levenberg-Marquardt Solver Algorithm in ComSol 5.5$^{\mathrm{TM}}$ (Part 2).

Parameter	$\Delta H_{O_2,Ag_{step}}$	$\Delta H_{CO_2,Ag_{step}}$	$Ea_{DCE,AgO_{sub}}$	$Ea_{DCE,Ag_{step}}$	A_{EO}	A_{CO_2}	$A_{DCE,Ag_{step}}$	$A_{O_2,AgO_{sub}}$
Ea_{EO}								
Ea_{CO_2}								
$\Delta H_{DCE,Ag_{step}}$								
$\Delta H_{O_2,AgO_{sub}}$								
$\Delta H_{CO_2,AgO_{sub}}$								
$\Delta H_{C_2H_4,AgO_{sub}}$								
$\Delta H_{DCE,AgO_{sub}}$								
$\Delta H_{O_2,Ag_{step}}$	1							
$\Delta H_{CO_2,Ag_{step}}$	-0.10	1						
$Ea_{DCE,AgO_{sub}}$	0.61	-0.18	1					
$Ea_{DCE,Ag_{step}}$	-0.16	-0.01	-0.02	1				
A_{EO}	0.00	0.00	0.00	0.01	1			
A_{CO_2}	-0.04	-0.83	0.53	0.03	0.00	1		
$A_{DCE,Ag_{step}}$	-0.06	0.00	0.58	0.07	0.00	0.00	1	
$A_{O_2,AgO_{sub}}$	0.00	0.00	0.00	0.17	0.18	0.00	0.00	1
$A_{CO_2,AgO_{sub}}$	0.01	0.12	-0.36	-0.58	0.01	0.05	0.00	0.03
$A_{C_2H_4,AgO_{sub}}$	0.00	-0.01	-0.02	0.76	0.01	0.01	0.00	-0.12
$A_{DCE,AgO_{sub}}$	-0.22	-0.01	0.04	0.16	0.00	0.00	0.28	0.00
$A_{O_2,Ag_{step}}$	0.51	0.76	-0.61	-0.03	0.00	-0.90	-0.01	0.00
$A_{CO_2,Ag_{step}}$	-0.02	-0.16	-0.62	0.02	0.00	-0.40	0.00	-0.01
$k^0_{DCE,AgO_{sub}}$	-0.02	-0.13	-0.56	0.06	0.00	-0.27	0.00	0.00
$k^0_{DCE,Ag_{step}}$	0.13	-0.06	0.32	-0.49	0.00	-0.01	-0.22	0.00

Table A.3: Correlation of the Kinetic Parameters Determined by Regression of Profiles Measured in the CPR Using the Levenberg-Marquardt Solver Algorithm in ComSol 5.5$^{\mathrm{TM}}$ (Part 3).

Parameter	$A_{CO_2,AgO_{sub}}$	$A_{C_2H_4,AgO_{sub}}$	$A_{DCE,AgO_{sub}}$	$A_{O_2,Ag_{step}}$	$A_{CO_2,Ag_{step}}$	$k^0_{DCE,AgO_{sub}}$	$k^0_{DCE,Ag_{step}}$
Ea_{EO}							
Ea_{CO_2}							
$\Delta H_{DCE,Ag_{step}}$							
$\Delta H_{O_2,AgO_{sub}}$							
$\Delta H_{CO_2,AgO_{sub}}$							
$\Delta H_{C_2H_4,AgO_{sub}}$							
$\Delta H_{DCE,AgO_{sub}}$							
$\Delta H_{O_2,Ag_{step}}$							
$\Delta H_{CO_2,Ag_{step}}$							
$Ea_{DCE,AgO_{sub}}$							
$Ea_{DCE,Ag_{step}}$							
A_{EO}							
A_{CO_2}							
$A_{DCE,Ag_{step}}$							
$A_{O_2,AgO_{sub}}$							
$A_{CO_2,AgO_{sub}}$	1						
$A_{C_2H_4,AgO_{sub}}$	0.31	1					
$A_{DCE,AgO_{sub}}$	0.00	0.00	1				
$A_{O_2,Ag_{step}}$	-0.06	-0.02	0.02	1			
$A_{CO_2,Ag_{step}}$	0.15	0.04	0.00	-0.60	1		
$k^0_{DCE,AgO_{sub}}$	0.14	0.02	0.00	-0.29	-0.60	1	
$k^0_{DCE,Ag_{step}}$	0.00	0.00	-0.19	0.10	-0.01	-0.01	1

A.3 Pilot Scale Profile Reactor Measurements

A.3.1 Profile Measurements at T = 180 °C

At 180 °C three different DCE cofeeding concentrations were tested. Profile measurements were started with 1.5 ppm of DCE, subsequently no DCE was fed to the reactor and profiles were measured. The last condition was at 0.75 ppm of DCE. The measurements were conducted in the described order. In Figure A.9a C_2H_4 and O_2 profiles can be seen measured at 180 °C and a DCE concentration of 1.5 ppm. The reaction starts slow at the entrance of the reactor due to the low wall temperature. When the temperature inside the fixed-bed increases, the reaction starts to accelerate slowly as can be seen by a change in the slope for the educt and product profiles in Figure A.9a - A.9b. This slope change can be good recognized in the EO profile, where for the CO_2 profile this is not so pronounced. After 100 mm inside the catalyst bed, the slope of the EO profile changes and more EO is produced. In the first 100 mm only little amounts of EO and CO_2 are formed, which is probably caused by the low temperature and the high O_2 coverage on the silver surface. Due to less vacant sites, less C_2H_4 can adsorb to react with O_2. After a starting phase, where vacant sites are formed, the reaction starts to accelerate to produce EO and CO_2. This explanation suits to the DCE and VC profile as well, since in the beginning of the bed, the DCE profile decreases only slightly and no VC could be measured, indicating that low amounts of chlorine could be deposited by DCE to form VC. At approximately 350 mm inside the bed, the reaction starts to accelerate even further, changing the slope of all components present in the reaction mixture. More EO and CO_2 are suddenly formed and more DCE is consumed and VC could be detected. In this phase of the reaction, the selectivity towards EO decreases until the end of the bed simultaneously with a conversion increase (Figure A.9c). For the next measurements, DCE was not fed to the reactor, as can be seen in Figure A.10. Although no DCE was fed, VC can still be detected at the end of the reactor showing the strong bond of chlorine to the surface and the slow reaction of removal chlorine adatoms from the surface as was already shown from CPR measurements. Due to the missing DCE to occupy vacant sites, higher reaction rates (activity) resulting in higher product and side product formation and higher temperatures can be detected. The shape of the profiles, look similar to the previous measurement, but more pronounced. The selectivity to EO decreases monotonically from the start of the reaction to the end of the bed. Whereas in the previous measurement, the selectivity did not drop as much as without DCE cofeeding. The comparison of O_2 conversion, shows the higher activity without DCE cofeeding by exceeding 10 % whereas with cofeeding approximately 7 % O_2 conversion is reached. The profile measurements at 0.75 ppm DCE in the feed give similar profile shapes as for the 1.5 ppm DCE cofeeding although a higher activity can be observed due to lower DCE cofeeding concentration. The O_2 conversion exceeds 10 % and selectivity to EO keeps above 80 %. In general, with decreasing DCE content in the feed, the overall activity increases leading to higher amount of reaction products and higher reaction temperature. The profile shape looks for all three cases similar with a kink in the temperature and concentration profiles and a different profile slope after the kink. This kink can be observed for each measurement, and is more pronounced without DCE cofeeding and higher activity. The overall selectivity decreases with decreased DCE cofeeding and a simultaneous increase in O_2 conversion.

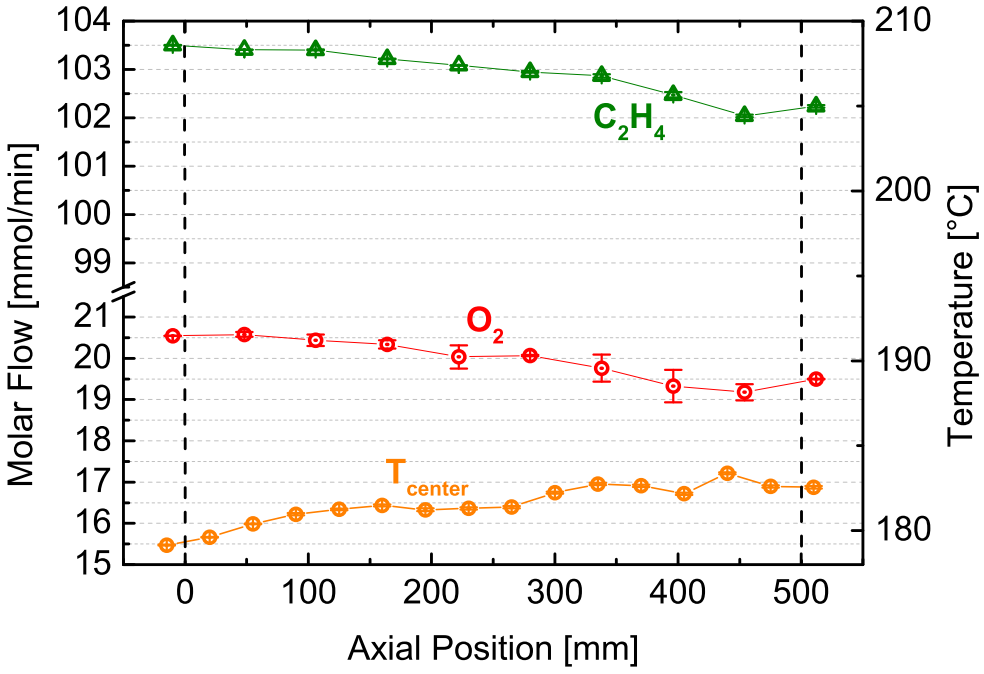

(a) Educt profile at 180 °C, 17 bara at GHSV = 4750 h^{-1} and 1.5 ppm DCE.

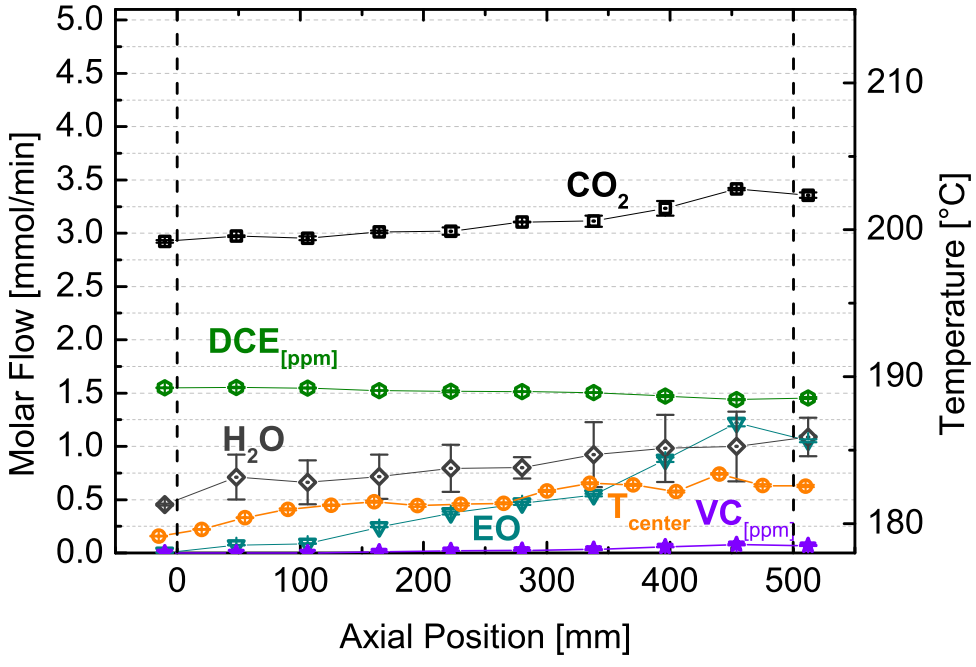

(b) Product profile at 180 °C, 17 bara at GHSV = 4750 h^{-1} and 1.5 ppm DCE.

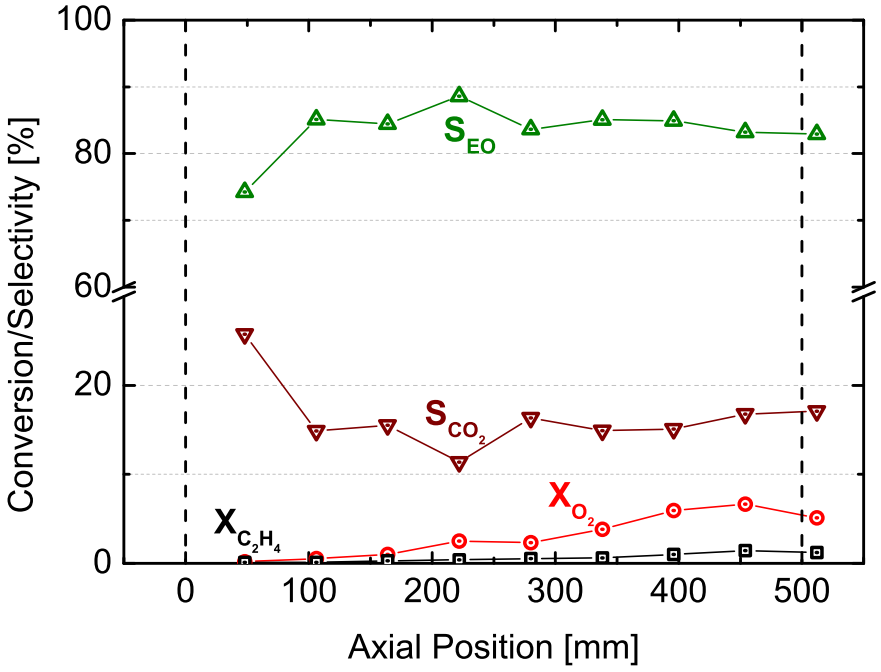

(c) Selectivity and conversion profile at 180 °C, 17 bara at GHSV = 4750 h^{-1} and 1.5 ppm DCE.

Figure A.9: Profiles measured in the Pilot Scale Profile Reactor at 180 °C, 17 bara at GHSV = 4750 h^{-1} and 1.5 ppm DCE.

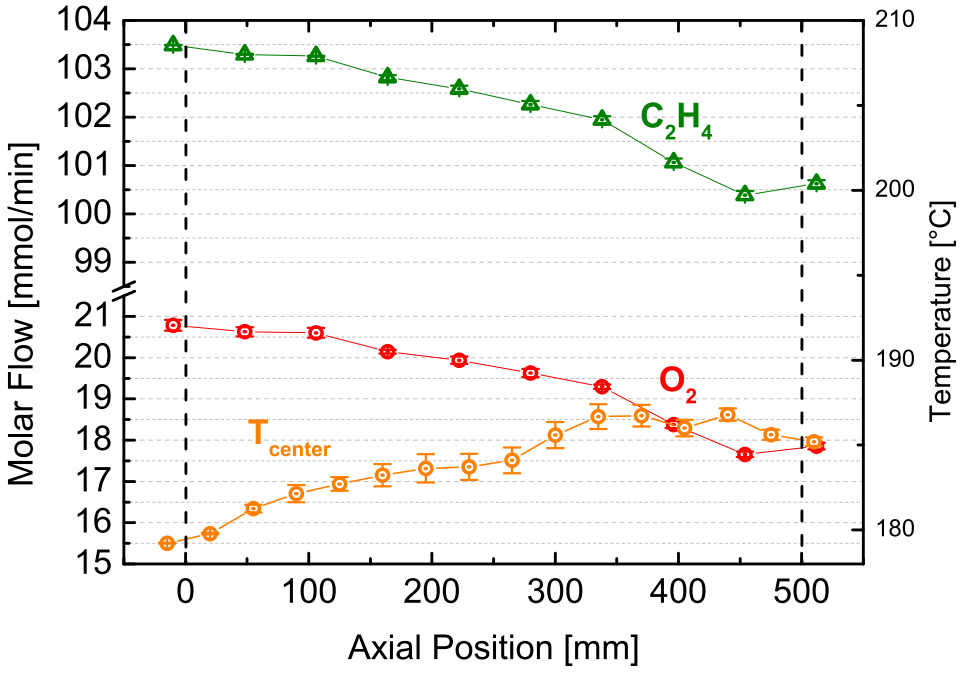

(a) Educt profile at 180 °C, 17 bara at GHSV = 4750 h^{-1} and 0 ppm DCE.

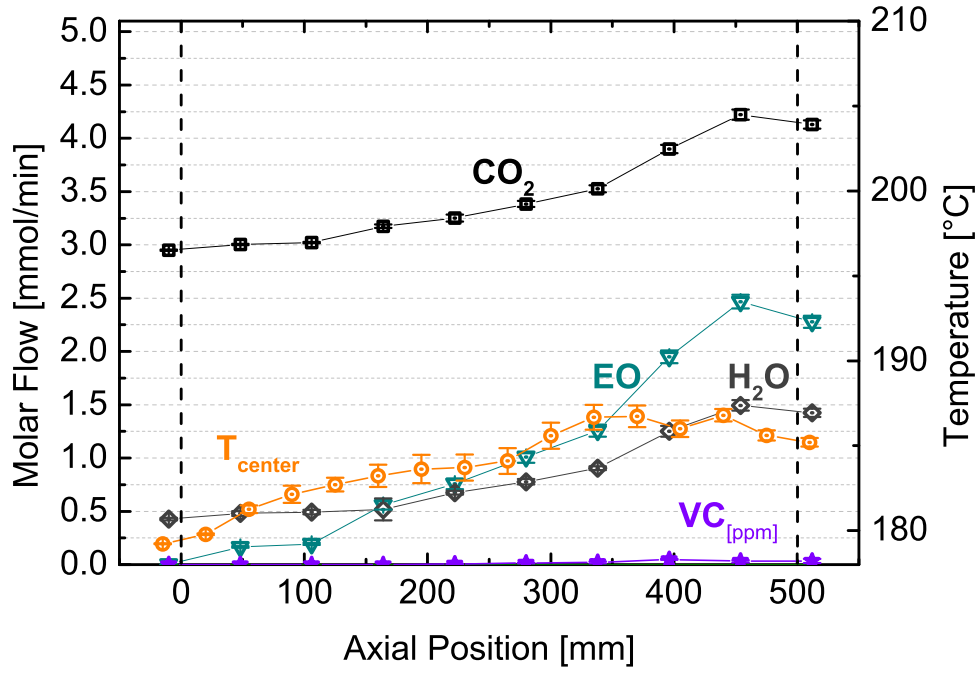

(b) Product profile at 180 °C, 17 bara at GHSV = 4750 h^{-1} and 0 ppm DCE.

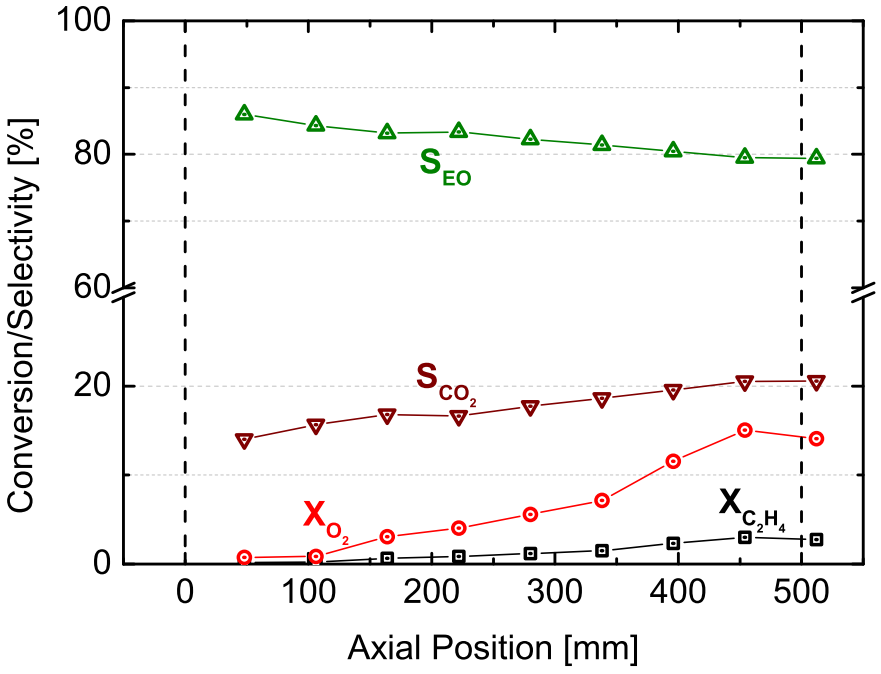

(c) Selectivity and conversion profile 180 °C, 17 bara at GHSV = 4750 h^{-1} and 0 ppm DCE.

Figure A.10: Profiles measured in the Pilot Scale Profile Reactor at 180 °C, 17 bara at GHSV = 4750 h^{-1} and 0 ppm DCE.

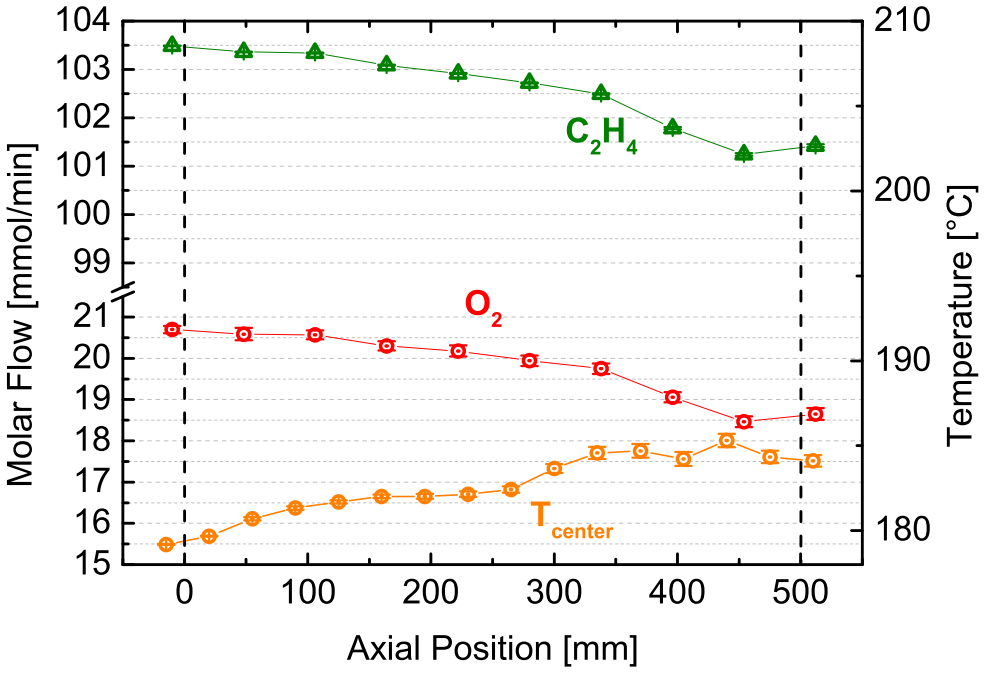

(a) Educt profile at 180 °C, 17 bara at GHSV = 4750 h^{-1} and 0.75 ppm DCE.

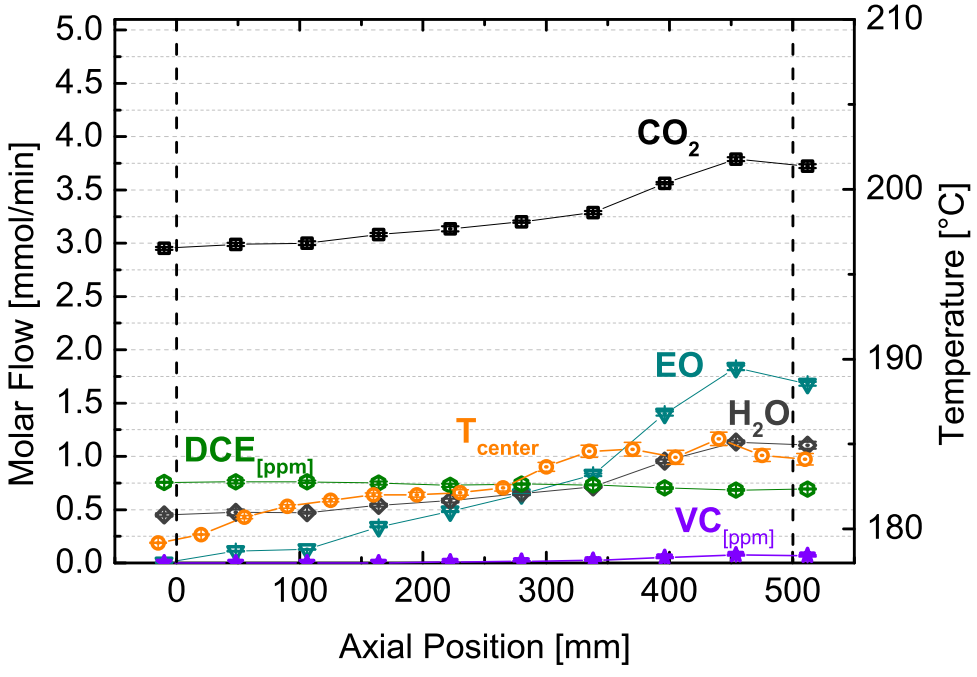

(b) Product profile at 180 °C, 17 bara at GHSV = 4750 h^{-1} and 0.75 ppm DCE.

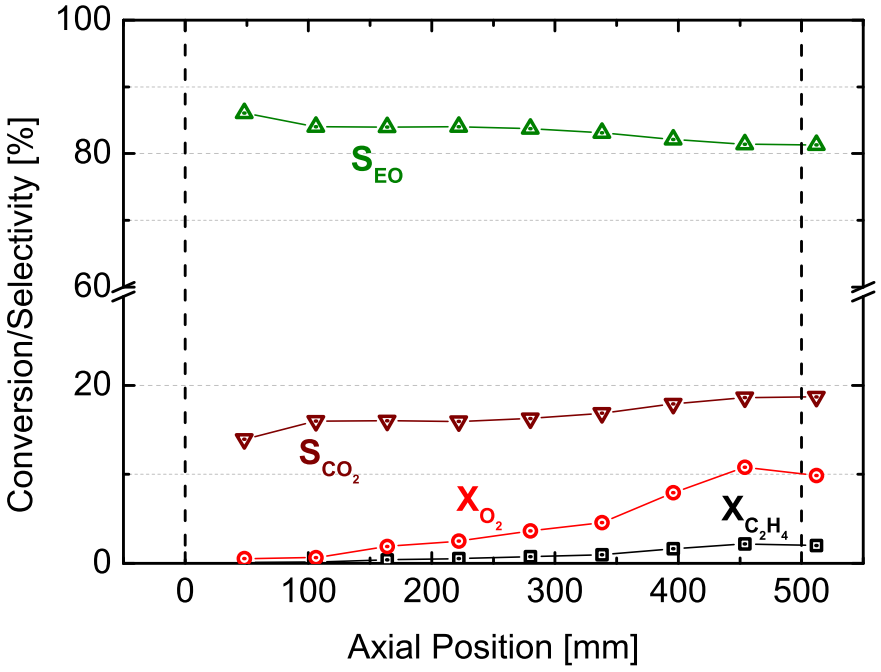

(c) Selectivity and conversion profile at 180 °C, 17 bara at GHSV = 4750 h^{-1} and 0.75 ppm DCE.

Figure A.11: Profiles measured in the Pilot Scale Profile Reactor at 180 °C, 17 bara at GHSV = 4750 h^{-1} and 0.75 ppm DCE.

A.3.2 Profile Measurements at T = 190 °C

At 190 °C two different conditions were measured. The first was at standard conditions with 1.5 ppm DCE in the feed, the second was with the same DCE concentration and without cofeeding CO_2. The profiles are illustrated in Figure A.12 and Figure A.13. When both conditions are compared with each other, it can be concluded that CO_2 cofeeding decreases the activity by blocking active sites, making them unavailable for the reaction. In opposite to DCE, CO_2 blocks all sites and does not enhance the selectivity to EO. Without CO_2 cofeeding the catalyst activity is higher, leading to higher reaction temperatures as can be seen in Figure A.13. The hot-spot temperature exceeds 200 °C compared to 196 °C with CO_2 cofeeding. Furthermore, the hot-spot temperature forms after 300 mm in the bed and not at the end. After the hot-spot, the temperature decreases again, due to wall cooling. Due to higher catalyst activity, O_2 conversion exceeds 20 % and EO selectivity drops below 80 % to 77 %, whereas the O_2 conversion with cofeeding CO_2 reaches 14 % with an EO selectivity of 80.5 %.

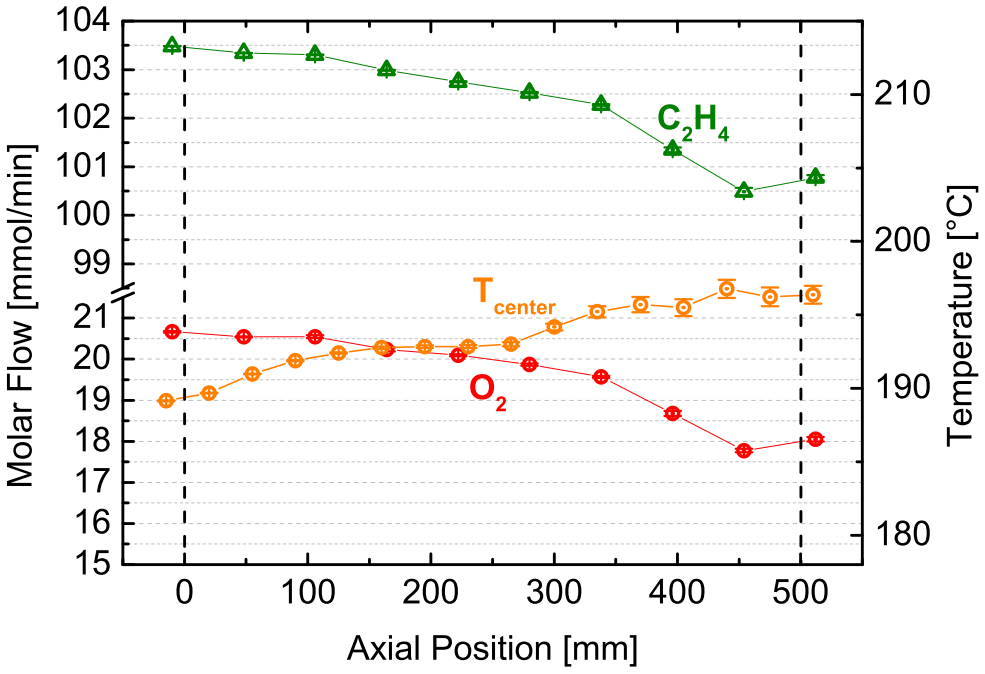

(a) Educt profile at 190 °C, 17 bara at GHSV = 4750 h^{-1} and 1.5 ppm DCE.

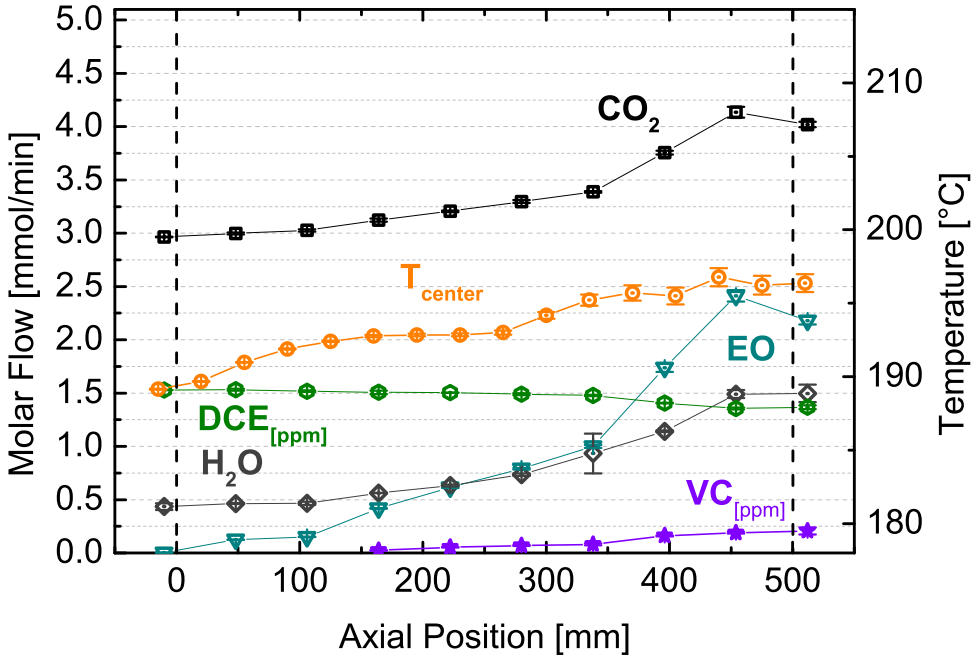

(b) Product profile at 190 °C, 17 bara at GHSV = 4750 h^{-1} and 1.5 ppm DCE.

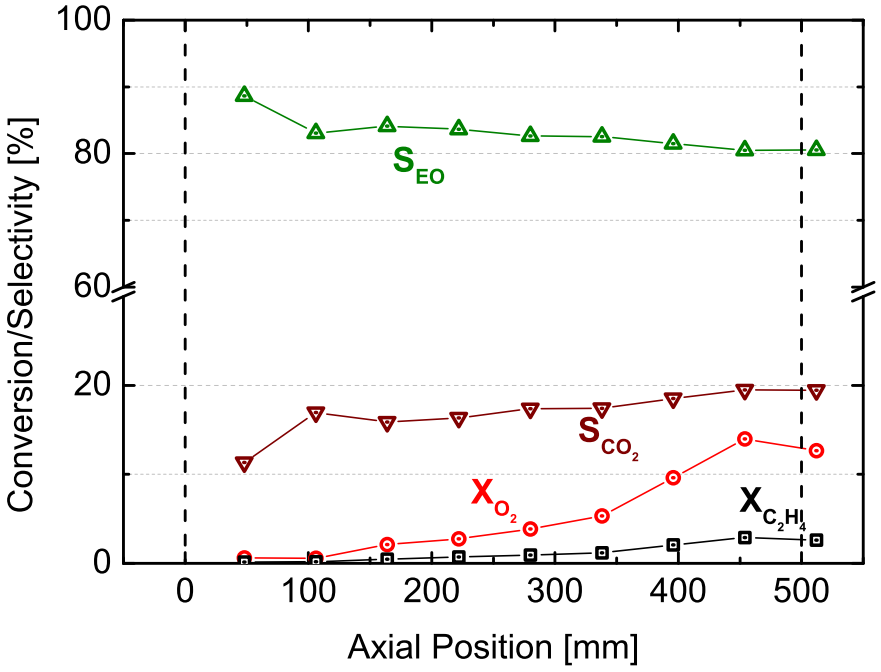

(c) Selectivity and conversion profile at 190 °C, 17 bara at GHSV = 4750 h^{-1} and 1.5 ppm DCE.

Figure A.12: Profiles measured in the Pilot Scale Profile Reactor at 190 °C, 17 bara at GHSV = 4750 h^{-1} and 1.5 ppm DCE.

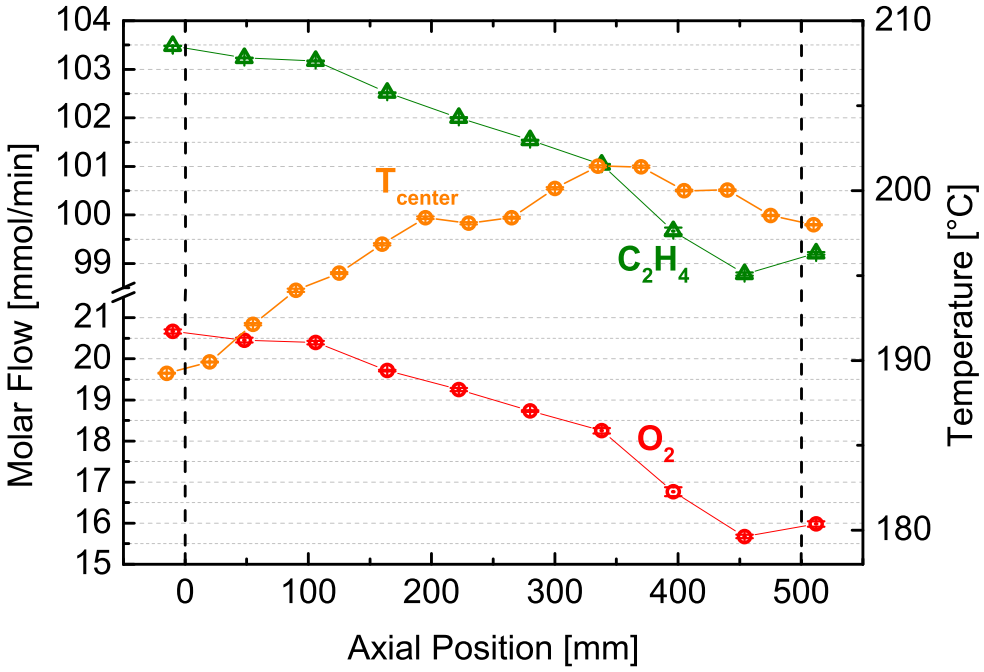

(a) Educt profile at 190 °C, 17 bara at GHSV = 4750 h^{-1} and 1.5 ppm DCE without CO_2 cofeeding.

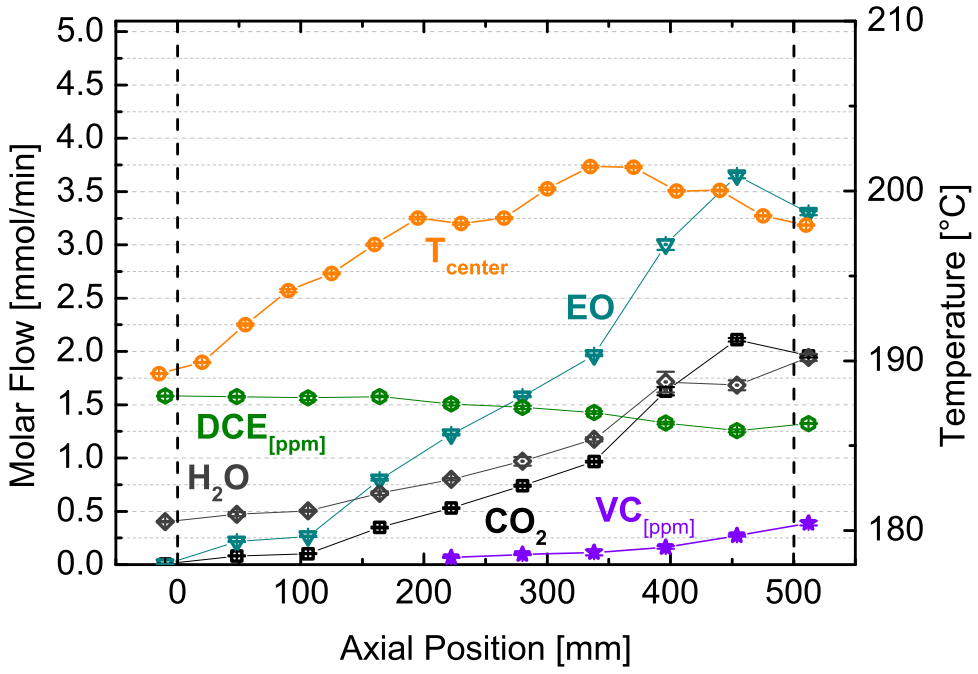

(b) Product profile at 190 °C, 17 bara at GHSV = 4750 h^{-1} and 1.5 ppm DCE without CO_2 cofeeding.

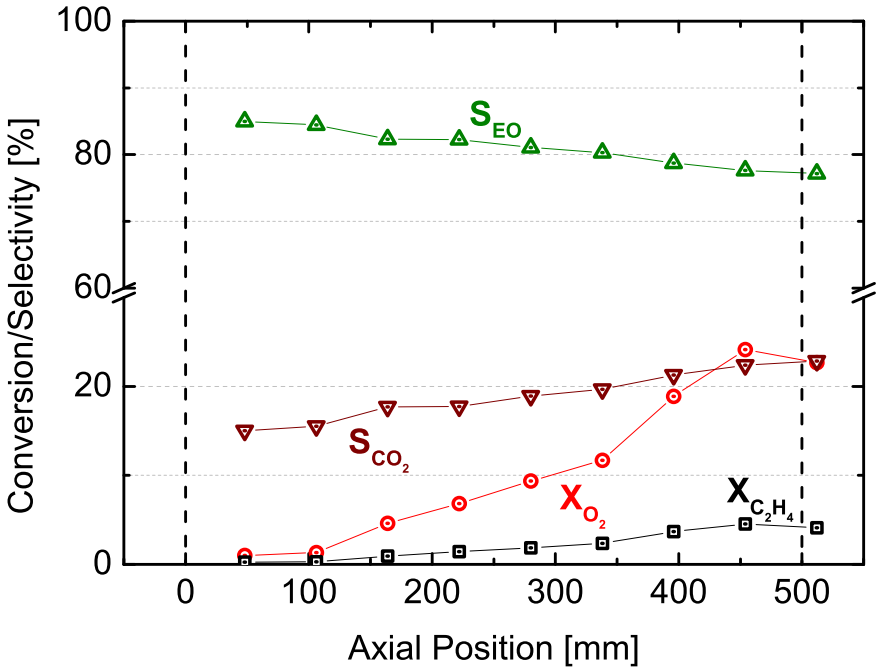

(c) Selectivity and conversion profile at 190 °C, 17 bara at GHSV = 4750 h^{-1} and 1.5 ppm DCE without CO_2 cofeeding.

Figure A.13: Profiles measured in the Pilot Scale Profile Reactor at 190 °C, 17 bara at GHSV = 4750 h^{-1} and 1.5 ppm DCE without CO_2 cofeeding.

A.3.3 Profile Measurements at T = 200 °C

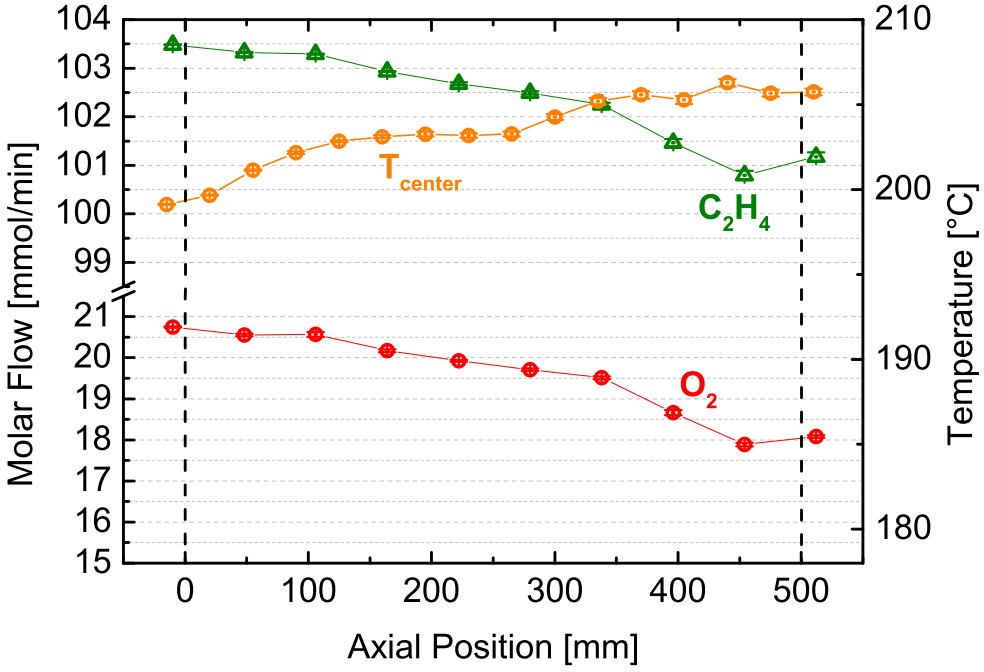

(a) Educt profile at 200 °C, 17 bara at GHSV = 4750 h^{-1} and 3.18 ppm DCE.

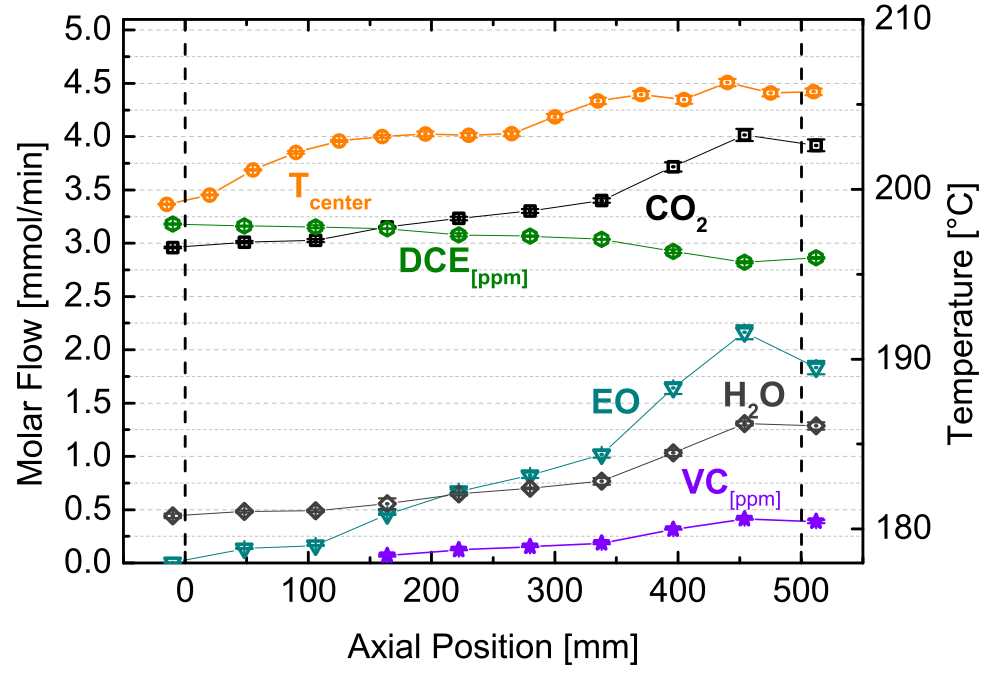

(b) Product profile at 200 °C, 17 bara at GHSV = 4750 h^{-1} and 3.18 ppm DCE.

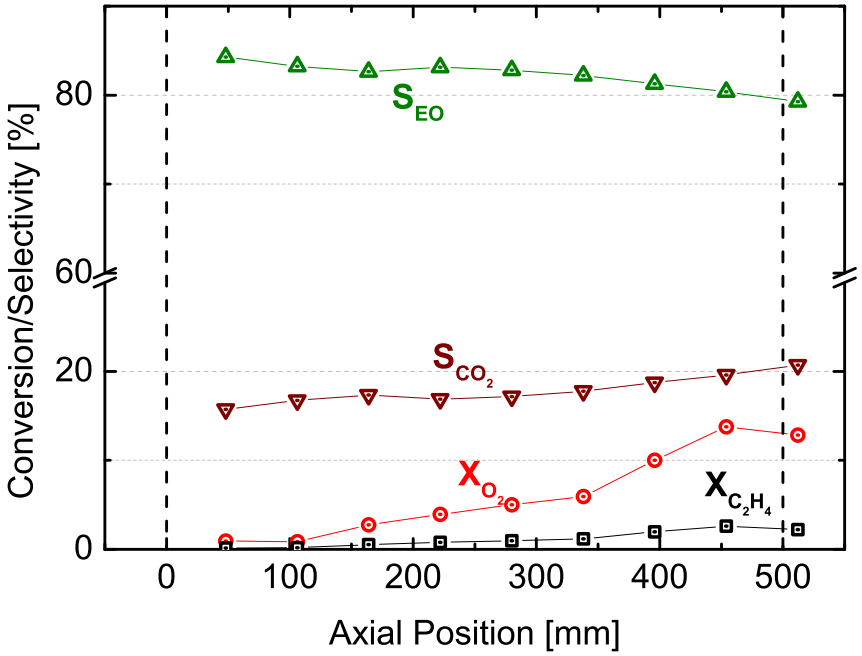

(c) Selectivity and conversion profile at 200 °C, 17 bara at GHSV = 4750 h^{-1} and 3.18 ppm DCE.

Figure A.14: Profiles measured in the Pilot Scale Profile Reactor at 200 °C, 17 bara at GHSV = 4750 h^{-1} and 3.18 ppm DCE.

The measurements at 200 °C show the importance of temperature. In no other measurement is the DCE consumption as pronounced as here. The VC formation reaches a value of about 0.5 ppm, more than in any other measurement. Due to the higher temperature, the threshold temperature in the reactor is approached, at which enough heat is available to allow chlorine deposition to occur more rapidly. Nevertheless, CPR-like behavior is not observed even at 200 °C because the reaction temperature is still too low compared to the measurements in the CPR.

Bibliography

[1] G. Eigenberger, W. Ruppel, Catalytic fixed-bed reactors, in: Ullmann's Encyclopedia of Industrial Chemistry, Wiley-VCH Verlag GmbH & Co. KGaA, Weinheim, Germany, 2012.

[2] R. Horn, Reaktoren für Fluid-Feststoff-Reaktionen: Festbettreaktoren, in: W. Reschetilowski (Ed.), Handbuch Chemische Reaktoren, Springer Berlin Heidelberg, Berlin, Heidelberg, 2019, pp. 1–70.

[3] M. Votsmeier, T. Kreuzer, J. Gieshoff, G. Lepperhoff, B. Elvers, Automobile Exhaust Control, in: Ullmann's Encyclopedia of Industrial Chemistry, John Wiley & Sons, Ltd, 2019, pp. 1–19.

[4] K. Pangarkar, T. J. Schildhauer, J. R. van Ommen, J. Nijenhuis, F. Kapteijn, J. A. Moulijn, Structured Packings for Multiphase Catalytic Reactors, Industrial & Engineering Chemistry Research 47 (10) (2008) 3720–3751.

[5] H. S. Fogler, Elements of Chemical Reaction Engineering, 5th Edition, Prentice Hall, Boston, 2016.

[6] O. Korup, S. Mavlyankariev, M. Geske, C. F. Goldsmith, R. Horn, Measurement and Analysis of Spatial Reactor Profiles in high Temperature Catalysis Research, Chemical Engineering and Processing: Process Intensification 50 (10) (2011) 998–1009.

[7] O. Korup, C. F. Goldsmith, G. Weinberg, M. Geske, T. Kandemir, R. Schlögl, R. Horn, Catalytic Partial Oxidation of Methane on Platinum Investigated by Spatial Reactor Profiles, Spatially Resolved Spectroscopy, and Microkinetic Modeling, Journal of Catalysis 297 (2013) 1–16.

[8] L. G. Pinaeva, A. S. Noskov, Prospects for the Development of Ethylene Oxide Production Catalysts and Processes (Review), Petroleum Chemistry 60 (11) (2020) 1191–1206.

[9] Ethylene Oxide Global Market Volume 2015-2029, `https://www.statista.com/statistics/1245260/ethylene-oxide-market-volume-worldwide/`, (accessed 2022-08-07).

[10] S. Rebsdat, D. Mayer, Ethylene Oxide, in: Wiley-VCH Verlag GmbH & Co. KGaA (Ed.), Ullmann's Encyclopedia of Industrial Chemistry, Wiley-VCH Verlag GmbH & Co. KGaA, Weinheim, Germany, 2001.

[11] R. van Santen, The Mechanism of Ethylene Epoxidation, Journal of Catalysis 98 (2) (1986) 530–539.

[12] S. Linic, M. A. Barteau, Control of Ethylene Epoxidation Selectivity by Surface Oxametallacycles, Journal of the American Chemical Society 125 (14) (2003) 4034–4035.

[13] C.-J. Chen, J. W. Harris, A. Bhan, Kinetics of Ethylene Epoxidation on a Promoted Ag/α-Al_2O_3 Catalyst–The Effects of Product and Chloride Co-Feeds on Rates and Selectivity, Chemistry – A European Journal 24 (47) (2018) 12405–12415.

[14] J. Falbe, H. Römpp (Eds.), Römpp-Lexikon Chemie, 10th Edition, Thieme, Stuttgart, 1996.

[15] R. Horn, O. Korup, M. Geske, U. Zavyalova, I. Oprea, R. Schlögl, Reactor for in Situ Measurements of Spatially Resolved Kinetic Data in Heterogeneous Catalysis, Review of Scientific Instruments 81 (6) (2010) 064102.

[16] D. Kunii, O. Levenspiel, Fluidization Engineering, 2nd Edition, Butterworth-Heinemann Series in Chemical Engineering, Butterworth-Heinemann, Boston, 1991.

[17] R. Horn, O. Korup, Application profile reactor for operando measurements, WO 2018/033523 (Feb. 2018).

[18] R. Schlögl, Heterogeneous Catalysis, Angewandte Chemie International Edition 54 (11) (2015) 3465–3520.

[19] J. Moulijn, P. van Leeuwen, R. Van Santen, History of Catalysis, in: Studies in Surface Science and Catalysis, Vol. 79, Elsevier, 1993, pp. 3–21.

[20] C. G. Hill, An Introduction to Chemical Engineering Kinetics & Reactor Design, Wiley, New York, 1977.

[21] K. G. Denbigh, The Principles of Chemical Equilibrium: With Applications in Chemistry and Chemical Engineering, 4th Edition, Cambridge University Press, 1981.

[22] O. Deutschmann, H. Knözinger, K. Kochloefl, T. Turek, Heterogeneous Catalysis and Solid Catalysts, in: Ullmann's Encyclopedia of Industrial Chemistry, Wiley-VCH Verlag GmbH & Co. KGaA, Weinheim, Germany, 2009.

[23] C. S. John, M. S. Scurrell, Catalytic Properties of Aluminas for Reactions of Hydrocarbons and Alcohols, in: C. Kemball (Ed.), Catalysis, Vol. 1, Royal Society of Chemistry, Cambridge, 1977, pp. 136–167.

[24] S. Govender, H. Friedrich, Monoliths: A Review of the Basics, Preparation Methods and Their Relevance to Oxidation, Catalysts 7 (12) (2017) 62.

[25] M. V. Twigg, J. T. Richardson, Fundamentals and Applications of Structured Ceramic Foam Catalysts, Industrial & Engineering Chemistry Research 46 (12) (2007) 4166–4177.

[26] G. Poncelet, P. Grange, P. A. Jacobs, Preparation of Catalysts III: Scientific Bases for the Preparation of Heterogeneous Catalysts : Proceedings of the Third International Symposium, Louvain-la-Neuve, September 6-9, 1982, Elsevier, Amsterdam; New York, 1983.

[27] A. B. Stiles, T. A. Koch, Catalyst Manufacture, 2nd Edition, CRC Press, Boca Raton, 1995.

[28] J. W. Geus, A. J. van Dillen, Preparation of Supported Catalysts by Deposition-Precipitation, in: G. Ertl, H. Knözinger, F. Schüth, J. Weitkamp (Eds.), Handbook of Heterogeneous Catalysis, Wiley-VCH Verlag GmbH & Co. KGaA, Weinheim, Germany, 2008.

[29] H. Düdder, K. Kähler, B. Krause, K. Mette, S. Kühl, M. Behrens, V. Scherer, M. Muhler, The Role of Carbonaceous Deposits in the Activity and Stability of Ni-Based Catalysts Applied in the Dry Reforming of Methane, Catalysis Science & Technology 4 (9) (2014) 3317–3328.

[30] J. B. Butt, E. E. Petersen, Activation, Deactivation, and Poisoning of Catalysts, Academic Press, San Diego, 1988.

[31] J. Hagen, Industrial Catalysis: A Practical Approach, 2nd Edition, Wiley-VCH Verlag GmbH & Co. KGaA, Weinheim, 2006.

[32] M. Kraus, G. M. Pajonk, W. M. H. Sachtler, Z. Pal, G. A. Somorjai, J. H. Block, D. L. Cocke, N. Kruse, D. S. Santilli, B. Gates, J. A. Martens, P. A. Jacobs, C. R. A. Catlow, A. T. Bell, E. J. Maginn, D. N. Theodorou, Elementary Steps and Mechanisms: Sections 5.3– 5.5, in: G. Ertl, H. Knzinger, J. Weitkamp (Eds.), Handbook of Heterogeneous Catalysis, Wiley-VCH Verlag GmbH, Weinheim, Germany, 1997, pp. 1051–1188.

[33] G. J. Hutchings, Promotion in Heterogeneous Catalysis: A Topic Requiring a New Approach?, Catalysis Letters 75 (1/2) (2001) 1–12.

[34] M. Atkins, J. Couves, M. Hague, B. Sakakini, K. Waugh, On the Role of Cs, Cl and Subsurface O in Promoting Selectivity in Ag/α-Al_2O_3 Catalysed Oxidation of Ethene to Ethene Epoxide, Journal of Catalysis 235 (1) (2005) 103–113.

[35] V. A. Likholobov, B. L. Moroz, R. A. van Santen, Organic Reactions: Sections 4.5– 4.6, in: G. Ertl, H. Knözinger, J. Weitkamp (Eds.), Handbook of Heterogeneous Catalysis, Wiley-VCH Verlag GmbH, Weinheim, Germany, 1997, pp. 2231–2334.

[36] M. Boudart, B. H. Davis, H. Heinemann, Principles of Heterogeneous Catalysis, in: G. Ertl, H. Knözinger, J. Weitkamp (Eds.), Handbook of Heterogeneous Catalysis, Wiley-VCH Verlag GmbH, Weinheim, Germany, 1997, pp. 1–48.

[37] H. S. Taylor, E. F. Armstrong, A Theory of the Catalytic Surface, Proceedings of the Royal Society of London. Series A, Containing Papers of a Mathematical and Physical Character 108 (745) (1925) 105–111.

[38] P. H. Emmett, Fifty Years of Progress in the Study of the Catalytic Synthesis of Ammonia, in: E. Drauglis, R. I. Jaffee (Eds.), The Physical Basis for Heterogeneous Catalysis, Springer US, Boston, MA, 1975, pp. 3–34.

[39] O. Hougen, K. Watson, Chemical Process Principles: Kinetics and Catalysis, Chemical Process Principles, J. Wiley & Sons, Incorporated, 1947.

[40] F. Kapteijn, J. A. Moulijn, Laboratory Catalytic Reactors: Aspects of Catalyst Testing, in: G. Ertl, J. Weitkamp (Eds.), Handbook of Heterogeneous Catalysis, Wiley-VCH Verlag GmbH & Co. KGaA, Weinheim, Germany, 2008.

[41] G. F. Froment, K. B. Bischoff, Chemical Reactor Analysis and Design, John Wiley and Sons, New York, 1979.

[42] P. Trambouze, H. van Landeghem, J.-P. Wauquier, Chemical Reactors: Design, Engineering, Operation, Institut Français Du Pétrole Publications, Editions Technip, Paris, 1988.

[43] C. N. Satterfield, Heterogeneous Catalysis in Industrial Practice, 2nd Edition, McGraw-Hill, New York, 1992.

[44] A. Cybulski, M. Van Dalen, J. Verkerk, P. Van Den Berg, Gas-Particle Heat Transfer Coefficients in Packed Beds at Low Reynolds Numbers, Chemical Engineering Science 30 (9) (1975) 1015–1018.

[45] L. K. Doraiswamy, M. M. Sharma, Heterogeneous Reactions: Analysis Examples and Reactor Design. Vol. 1: Gas Solid and Solid-Solid Reactions, John Wiley and Sons, New York, NY, 1984.

[46] Y. Dong, F. J. Keil, O. Korup, F. Rosowski, R. Horn, Effect of the Catalyst Pore Structure on Fixed-Bed Reactor Performance of Partial Oxidation of n-Butane: A Simulation Study, Chemical Engineering Science 142 (2016) 299–309.

[47] E. L. Cussler, Diffusion: Mass Transfer in Fluid Systems, 2nd Edition, Cambridge University Press, New York, 1997.

[48] R. C. Reid, J. M. Prausnitz, B. E. Poling, The Properties of Gases and Liquids, 4th Edition, McGraw-Hill, New York, 1987.

[49] J. O. Hirschfelder, C. F. Curtiss, R. B. Bird, Molecular Theory of Gases and Liquids, corr. print. with notes added Edition, Structure of Matter Series, Wiley, New York,NY, 1964.

[50] E. C. Itean, A. R. Glueck, R. A. Svehla, Collision Integrals for a Modified Stockmayer Potential, National Aeronautics and Space Administration, 1961.

[51] M. Klein, F. J. Smith, Tables of Collision Integrals for the (m,6) Potential Function for 10 Values of m, Journal of Research of the National Bureau of Standards Section A: Physics and Chemistry 72A (4) (1968) 359.

[52] P. D. Neufeld, A. R. Janzen, R. A. Aziz, Empirical Equations to Calculate 16 of the Transport Collision Integrals $\Omega^{(l,s)^*}$ for the Lennard-Jones (12–6) Potential, The Journal of Chemical Physics 57 (3) (1972) 1100–1102.

[53] F. Keil, Diffusion und Chemische Reaktionen in der Gas/Feststoff-Katalyse, Springer Berlin, Heidelberg, 1999.

[54] C. N. Satterfield, Mass Transfer in Heterogeneous Catalysis, M.I.T. Press, Cambridge, Mass, 1969.

[55] E. Mason, A. Malinauskas, Gas Transport in Porous Media: The Dusty-Gas Model, Chemical Engineering Monographs, Elsevier, 1983.

[56] E. W. Thiele, Relation between Catalytic Activity and Size of Particle, Industrial & Engineering Chemistry 31 (7) (1939) 916–920.

[57] J. J. Carberry, Physico-Chemical Aspects of Mass and Heat Transfer in Heterogeneous Catalysis, in: J. R. Anderson, M. Boudart (Eds.), Catalysis: Science and Technology, Catalysis, Springer, Berlin, Heidelberg, 1987, pp. 131–171.

[58] J. Moulijn, A. Tarfaoui, F. Kapteijn, General Aspects of Catalyst Testing, Catalysis Today 11 (1) (1991) 1–12.

[59] D. E. Mears, Tests for Transport Limitations in Experimental Catalytic Reactors, Industrial & Engineering Chemistry Process Design and Development 10 (4) (1971) 541–547.

[60] O. Bey, G. Eigenberger, Gas Flow and Heat Transfer through Catalyst Filled Tubes, International Journal of Thermal Sciences 40 (2) (2001) 152–164.

[61] D. Mears, Diagnostic Criteria for Heat Transport Limitations in Fixed Bed Reactors, Journal of Catalysis 20 (2) (1971) 127–131.

[62] D. Kunii, O. Levenspiel, A General Equation for the Heat-Transfer Coefficient at Wall Surfaces of Gas/Solid Contactors, Industrial & Engineering Chemistry Research 30 (1) (1991) 136–141.

[63] E. Tsotsas, M7 Heat and Mass Transfer in Packed Beds with Fluid Flow, in: VDI e. V. (Ed.), VDI Heat Atlas, Springer Berlin Heidelberg, Berlin, Heidelberg, 2010, pp. 1327–1342.

[64] M. Neubronner, T. Bodmer, C. Hübner, P. B. Kempa, E. Tsotsas, A. Eschner, G. Kasparek, F. Ochs, H. Müller-Steinhagen, H. Werner, M. H. Spitzner, D6 Properties of Solids and Solid Materials, in: VDI e. V. (Ed.), VDI Heat Atlas, Springer Berlin Heidelberg, Berlin, Heidelberg, 2010, pp. 551–614.

[65] C. F. Chu, K. M. Ng, Flow in Packed Tubes with a Small Tube to Particle Diameter Ratio, AIChE Journal 35 (1) (1989) 148–158.

[66] M. Boudart, H. Brenner, Kinetics of Chemical Processes: Butterworth-Heinemann Series in Chemical Engineering, Elsevier Science, Saint Louis, 2014.

[67] I. Langmuir, Chemical Reactions at Low Pressures, Journal of the American Chemical Society 37 (5) (1915) 1139–1167.

[68] O. A. Hougen, K. M. Watson, General Principles, Industrial & Engineering Chemistry 35 (5) (1943) 529–541.

[69] F. Kapteijn, J. A. Moulijn, G. Emig, R. Dittmeyer, J. Krger, Kinetics and Transport Processes, in: G. Ertl, H. Knözinger, J. Weitkamp (Eds.), Handbook of Heterogeneous Catalysis, Wiley-VCH Verlag GmbH, Weinheim, Germany, 1997, pp. 1189–1261.

[70] C. T. Campbell, Surface Science Study of Selective Ethylene Epoxidation Catalyzed by the Ag(110) Surface: Structural Sensitivity, Journal of Vacuum Science & Technology A: Vacuum, Surfaces, and Films 2 (2) (1984) 1024–1027.

[71] K. Yang, O. Hougen, Determination of Mechanism of Catalyzed Gaseous Reactions, Chemical Engineering Progress 46 (3) (1950) 146–157.

[72] W. M. H. Sachtler, C. Backx, R. A. V. Santen, On the Mechanism of Ethylene Epoxidation, Catalysis Reviews 23 (1-2) (1981) 127–149.

[73] N. Cant, Catalytic Oxidation VI. Oxidation of Labeled Olefins over Silver, Journal of Catalysis 52 (1) (1978) 81–94.

[74] H. Gierman, Design of Laboratory Hydrotreating Reactors, Applied Catalysis 43 (2) (1988) 277–286.

[75] T. E. Lefort, Process for the production of ethylene oxide, US1998878A (Apr. 1935).

[76] H.-J. Arpe, Industrielle organische Chemie: bedeutende Vor- und Zwischenprodukte, 6th Edition, Wiley-VCH, Weinheim, 2007.

[77] J. W. Bolk, K. R. Westerterp, Influence of Hydrodynamics on the Upper Explosion Limit of Ethene–Air–Nitrogen Mixtures, AIChE Journal 45 (1) (1999) 124–144.

[78] J. M. Berty, Inhibitor Action of Chlorinated Hydrocarbons in Oxidation of Ethylene to Ethylene Oxide, Chemical Engineering Communications 82 (1) (1989) 229–232.

[79] D. A. Bulushev, E. A. Paukshtis, Y. N. Nogin, B. S. Bal'zhinimaev, Transient Response and Infrared Studies of Ethylene Oxide Reactions on Silver Catalysts and Supports, Applied Catalysis A-General 123 (2) (1995) 301–322.

[80] V. I. Bukhtiyarov, I. P. Prosvirin, R. I. Kvon, S. N. Goncharova, B. S. Bal'zhinimaev, XPS Study of the Size Effect in Ethene Epoxidation on Supported Silver Catalysts, Journal of the Chemical Society, Faraday Transactions 93 (13) (1997) 2323–2329.

[81] R. van Santen, H. Kuipers, The Mechanism of Ethylene Epoxidation, in: Advances in Catalysis, Vol. 35, Elsevier, 1987, pp. 265–321.

[82] P. A. Kilty, W. M. H. Sachtler, The Mechanism of the Selective Oxidation of Ethylene to Ethylene Oxide, Catalysis Reviews 10 (1) (1974) 1–16.

[83] D. Park, S. Ghazali, G. Gau, A cyclic reactor study of ethylene epoxidation, Applied Catalysis 6 (2) (1983) 175–193.

[84] H. R. Dettwiler, A. Baiker, W. Richarz, Kinetics of Ethylene Oxidation on a Supported Silver Catalyst, Helvetica Chimica Acta 62 (6) (1979) 1689–1700.

[85] C. T. Campbell, Chlorine Promotion of Selective Ethylene Oxidation over Ag(110): Kinetics and Mechanism, Journal of Catalysis 92 (2) (1985) 272–283.

[86] C. T. Campbell, Chlorine Promoters in Selective Ethylene Epoxidation over Ag(111): A Comparison with Ag(110), Journal of Catalysis 99 (1) (1986) 28–38.

[87] R. B. Grant, R. M. Lambert, A Single Crystal Study of the Silver-Catalysed Selective Oxidation and Total Oxidation of Ethylene, Journal of Catalysis 92 (2) (1985) 364–375.

[88] R. B. Grant, R. M. Lambert, Basic Studies of the Oxygen Surface Chemistry of Silver: Chemisorbed Atomic and Molecular Species on Pure Ag(111), Surface Science 146 (1) (1984) 256–268.

[89] E. L. Force, A. T. Bell, The Effect of Dichloroethane Moderation on the Adsorbed Species Present during the Oxidation of Ethylene over Silver, Journal of Catalysis 44 (2) (1976) 175–182.

[90] E. L. Force, A. T. Bell, Infrared Spectra of Adsorbed Species Present during the Oxidation of Ethylene over Silver, Journal of Catalysis 38 (1) (1975) 440–460.

[91] E. L. Force, A. T. Bell, The Relationship of Adsorbed Species Observed by Infrared Spectroscopy to the Mechanism of Ethylene Oxidation over Silver, Journal of Catalysis 40 (3) (1975) 356–371.

[92] M. O. Özbek, I. Önal, R. A. van Santen, Chlorine and Caesium Promotion of Silver Ethylene Epoxidation Catalysts, ChemCatChem 5 (2) (2013) 443–451.

[93] T. C. R. Rocha, M. Hävecker, A. Knop-Gericke, R. Schlögl, Promoters in Heterogeneous Catalysis: The Role of Cl on Ethylene Epoxidation over Ag, Journal of Catalysis 312 (2014) 12–16.

[94] V. Bukhtiyarov, A. Nizovskii, H. Bluhm, M. Hävecker, E. Kleimenov, A. Knop-Gericke, R. Schlögl, Combined in Situ XPS and PTRMS Study of Ethylene Epoxidation over Silver, Journal of Catalysis 238 (2) (2006) 260–269.

[95] D. Torres, F. Illas, R. M. Lambert, Towards an Understanding of Promoter Action in Heterogeneously Catalyzed Ethene Epoxidation: Why Chlorine is the Best Halogen, Journal of Catalysis 260 (2) (2008) 380–383.

[96] M. Bowker, K. C. Waugh, The Adsorption of Chlorine and Chloridation of Ag(111), Surface Science 134 (3) (1983) 639–664.

[97] J. R. Lockemeyer, T. L. Lohr, Ethylene Oxide Catalysis Under Commercial Conditions – A Guide for Researchers, ChemCatChem 15 (2023) e202201511.

[98] J. W. Harris, A. Bhan, Moderation of Chlorine Coverage and Ethylene Epoxidation Kinetics via Ethane Oxychlorination over Promoted Ag/α-Al_2O_3, Journal of Catalysis 367 (2018) 62–71.

[99] J. W. Harris, J. A. Herron, J. F. DeWilde, A. Bhan, Molecular Characteristics Governing Chlorine Deposition and Removal on Promoted Ag Catalysts during Ethylene Epoxidation, Journal of Catalysis 377 (2019) 378–388.

[100] P. D. Klugherz, P. Harriott, Kinetics of Ethylene Oxidation on a Supported Silver Catalyst, AIChE Journal 17 (4) (1971) 856–866.

[101] P. L. Metcalf, P. Harriott, Kinetics of Silver-Catalyzed Ethylene Oxidation, Industrial & Engineering Chemistry Process Design and Development 11 (4) (1972) 478–484.

[102] L. Petrov, A. Eliyas, D. Shopov, A Kinetic Model of Steady State Ethylene Epoxidation over a Supported Silver Catalyst, Applied Catalysis 18 (1) (1985) 87–103.

[103] S. Ghazali, D. Park, G. Gau, Kinetics of Ethylene Epoxidation on a Silver Catalyst, Applied Catalysis 6 (2) (1983) 195–208.

[104] D. Park, Ethylene Epoxidation on a Silver Catalyst: Unsteady and Steady State Kinetics, Journal of Catalysis 105 (1) (1987) 81–94.

[105] M. Stoukides, S. Pavlou, Ethylene Oxidation on Silver Catalysts: Effect of Ethylene Oxide and of External Transfer Limitations, Chemical Engineering Communications 44 (1-6) (1986) 53–74.

[106] M. Al-Saleh, M. Al-Ahmadi, M. Shalabi, Kinetic Study of Ethylene Oxidation in a Berty Reactor, Chemical Engineering Journal 37 (1) (1988) 35–41.

[107] P. C. Borman, K. R. Westerterp, An Experimental Study of the Kinetics of the Selective Oxidation of Ethene over a Silver on α-Alumina Catalyst, Industrial & Engineering Chemistry Research 34 (1) (1995) 49–58.

[108] D. Lafarga, M. A. Al-Juaied, C. M. Bondy, A. Varma, Ethylene Epoxidation on Ag-Cs/α-Al_2O_3 Catalyst: Experimental Results and Strategy for Kinetic Parameter Determination, Industrial & Engineering Chemistry Research 39 (7) (2000) 2148–2156.

[109] J. R. H. Carucci, V. Halonen, K. Eränen, J. Wärnå, S. Ojala, M. Huuhtanen, R. Keiski, T. Salmi, Ethylene Oxide Formation in a Microreactor: From Qualitative Kinetics to Detailed Modeling, Industrial & Engineering Chemistry Research 49 (21) (2010) 10897–10907.

[110] S. Linic, Construction of a Reaction Coordinate and a Microkinetic Model for Ethylene Epoxidation on Silver from DFT Calculations and Surface Science Experiments, Journal of Catalysis 214 (2) (2003) 200–212.

[111] C. Stegelmann, N. C. Schiødt, C. T. Campbell, P. Stoltze, Microkinetic Modeling of Ethylene Oxidation over Silver, Journal of Catalysis 221 (2) (2004) 630–649.

[112] C. Stegelmann, Microkinetic Analysis of Transient Ethylene Oxidation Experiments on Silver, Journal of Catalysis 226 (1) (2004) 129–137.

[113] S. Linic, M. A. Barteau, Formation of a Stable Surface Oxametallacycle that Produces Ethylene Oxide, Journal of the American Chemical Society 124 (2) (2002) 310–317.

[114] S. Linic, H. Piao, K. Adib, M. A. Barteau, Ethylene Epoxidation on Ag: Identification of the Crucial Surface Intermediate by Experimental and Theoretical Investigation of its Electronic Structure, Angewandte Chemie 116 (22) (2004) 2978–2981.

[115] S. Linic, M. A. Barteau, Heterogeneous catalysis of alkene epoxidation, in: G. Ertl, H. Knözinger, F. Schüth, J. Weitkamp (Eds.), Handbook of Heterogeneous Catalysis, John Wiley & Sons Ltd., Weinheim, Germany, 2008, Ch. 14.11.6, pp. 3448–3464.

[116] J. W. Harris, A. Bhan, Kinetics of Chlorine Deposition and Removal over Promoted Silver Catalysts during Ethylene Epoxidation, Journal of Catalysis 380 (2019) 318–331.

[117] K. R. Iyer, A. Bhan, Interdependencies Among Ethylene Oxidation and Chlorine Moderation Catalytic Cycles Over Promoted Ag/α-Al_2O_3 Catalysts, ACS Catalysis 11 (24) 14864–14876.

[118] J. M. P. Q. Delgado, A Critical Review of Dispersion in Packed Beds, Heat and Mass Transfer 42 (4) (2006) 279–310.

[119] D. E. Mears, On Criteria for Axial Dispersion in Nonisothermal Packed-Bed Catalytic Reactors, Industrial & Engineering Chemistry Fundamentals 15 (1) (1976) 20–23.

[120] J. J. Carberry, D. White, On the Role of Transport Phenomena in Catalytic Reactor Behavior, Industrial & Engineering Chemistry 61 (7) (1969) 27–35.

[121] VDI e. V, VDI-Wärmeatlas, Imprint: Springer Vieweg, Berlin, Heidelberg, 2013.

[122] A. G. Dixon, An Improved Equation for the Overall Heat Transfer Coefficient in Packed Beds, Chemical Engineering and Processing: Process Intensification 35 (5) (1996) 323–331.

[123] O. Levenspiel, Flow through Packed Beds, in: Engineering Flow and Heat Exchange, Springer US, Boston, MA, 1998, pp. 123–139.

[124] M. Giese, K. Rottschäfer, D. Vortmeyer, Measured and Modeled Superficial Flow Profiles in Packed Beds with Liquid Flow, AIChE Journal 44 (2) (1998) 484–490.

[125] M. Winterberg, E. Tsotsas, A. Krischke, D. Vortmeyer, A Simple and Coherent Set of Coefficients for Modelling of Heat and Mass Transport with and without Chemical Reaction in Tubes Filled with Spheres, Chemical Engineering Science 55 (5) (2000) 967–979.

[126] P. Marín, F. V. Díez, S. Ordóñez, Fixed Bed Membrane Reactors for WGSR-based Hydrogen Production: Optimisation of Modelling Approaches and Reactor Performance, International Journal of Hydrogen Energy 37 (6) (2012) 4997–5010.

[127] C. du Toit, Radial Variation in Porosity in Annular Packed Beds, Nuclear Engineering and Design 238 (11) (2008) 3073–3079.

[128] D. Vortmeyer, J. Schuster, Evaluation of Steady Flow Profiles in Rectangular and Circular Packed Beds by a Variational Method, Chemical Engineering Science 38 (10) (1983) 1691–1699.

[129] C. Y. Wen, Y. H. Yu, A Generalized Method for Predicting the Minimum Fluidization Velocity, AIChE Journal 12 (3) (1966) 610–612.

[130] D. Kunii, O. Levenspiel, Fluidization Engineering, 2nd Edition, Butterworth-Heinemann Series in Chemical Engineering, Butterworth-Heinemann, Boston, 1991.

[131] D. R. Lide (Ed.), CRC Handbook of Chemistry and Physics: A Ready-Reference Book of Chemical and Physical Data, 76th Edition, CRC Press, Boca Raton, 1996.

[132] Diagrams for the chemical and petrochemical industry - Part 1: Specification of diagrams (ISO 10628-1:2014); German version EN ISO 10628-1:2015 (2015).

[133] Chemical apparatus - Documentation in the life cycle of process plants - Part 5: Graphical symbols of apparatus and machines (2015).

[134] Arbeitsgemeinschaft Druckbehälter, AD 2000-Regelwerk, Heymann, Köln, 2002.

[135] DIN EN 1092-1:2018-12, Flansche und ihre Verbindungen - Runde Flansche für Rohre, Armaturen, Formstücke und Zubehörteile, nach PN bezeichnet - Teil 1: Stahlflansche; Deutsche Fassung EN 1092-1:2018 (2018).

[136] C. Bartosch, A. Karpov, M. Kraemer, G. Krennrich, D. O. A. Lange, C. Walsdorff, J. Zuehlke, Catalyst Effective in the Oxidative Conversion of Ethylene to Ethylene Oxide, WO2019154832A1 (Aug 2019).

[137] A. Wassiljewa, Wärmeleitung in Gasgemischen, Physik. Z. 5 (1904) 737–742.

[138] E. A. Mason, S. C. Saxena, Approximate Formula for the Thermal Conductivity of Gas Mixtures, Physics of Fluids 1 (5) (1958) 361.

[139] K. L. Yeung, A. Gavriilidis, A. Varma, M. M. Bhasin, Effects of 1,2 Dichloroethane Addition on the Optimal Silver Catalyst Distribution in Pellets for Epoxidation of Ethylene, Journal of Catalysis 174 (1) (1998) 1–12.

[140] R. E. Kenson, M. Lapkin, Kinetics and Mechanism of Ethylene Oxidation. Reactions of Ethylene and Ethylene Oxide on a Silver Catalyst, The Journal of Physical Chemistry 74 (7) (1970) 1493–1502.

[141] J. Jankowiak, M. Barteau, Ethylene Epoxidation over Silver and Copper–Silver Bimetallic Catalysts: I. Kinetics and Selectivity, Journal of Catalysis 236 (2) (2005) 366–378.

[142] T. E. Jones, T. C. R. Rocha, A. Knop-Gericke, C. Stampfl, R. Schlögl, S. Piccinin, Adsorbate Induced Vacancy Formation on Silver Surfaces, Physical Chemistry Chemical Physics 16 (19) (2014) 9002.

[143] V. I. Bukhtiyarov, M. Hävecker, V. V. Kaichev, A. Knop-Gericke, R. W. Mayer, R. Schlögl, Atomic Oxygen Species on Silver: Photoelectron Spectroscopy and x-Ray Absorption Studies, Physical Review B 67 (23) (2003) 235422.

[144] K. Waugh, M. Hague, The Detailed Kinetics and Mechanism of Ethylene Epoxidation on an Oxidised Ag/α-Al_2O_3 Catalyst, Catalysis Today 157 (1-4) (2010) 44–48.

[145] D. M. Espie, S. Macchietto, Nonlinear transformations for parameter estimation, Industrial Engineering Chemistry Research 27 (11) (1988) 2175–2179.

[146] A. K. Agarwal, M. L. Brisk, Sequential experimental design for precise parameter estimation. 1. Use of reparameterization, Industrial & Engineering Chemistry Process Design and Development 24 (1) (1985) 203–207.

[147] N. Delgado Otalvaro, G. Sogne, K. Herrera Delgado, S. Wild, S. Pitter, J. Sauer, Kinetics of the direct DME synthesis from CO_2 rich syngas under variation of the CZA$-$to$-\gamma-Al_2O_3$ ratio of a mixed catalyst bed, Royal Society of Chemistry Advances 11 (2021) 24556–24569.

[148] J. P. Dever, M. A. Nunley, J. R. Rader, G. Proulx, Ethylene Oxide, in: Kirk-Othmer Encyclopedia of Chemical Technology, John Wiley & Sons, Ltd, 2022, pp. 1–40.

Nomenclature

Abbreviations

AA	Acetaldehyde
CFD	Computational fluid dynamics
CPR	Compact Profile Reactor
DCE	1,2-dichloroethane
DFT	Density Functional Theory
EC	Ethyl chloride
EDX	Energy dispersive X-ray spectroscopy
EO	Ethylene oxide
FID	Flame ionization detector
GC	Gas chromatograph
GHSV	Gas hourly space velocity [h^{-1}]
PLC	Programmable logic controller
PSPR	Pilot Scale Profile Reactor
PTFE	Polytetrafluoroethylene
P&ID	Piping and instruments diagram
TCD	Thermal conductivity detector
VC	Vinyl chloride

Greek letters

α	Reaction order [-]
β_i	Internal Prater number $\frac{(-\Delta H_R)\cdot D_{eff}\cdot c_s}{\lambda_{p,eff}\cdot T_s}$ [-]
β_w	Wall Prater number $\frac{r_{V,obs}\cdot(-\Delta H_R)\cdot d_t^2}{4\cdot\lambda_{bed,eff}\cdot T_w}$ [-]
β_e	External Prater number $\frac{k_f\cdot c_b\cdot(-\Delta H_R)}{h\cdot T_b}$ [-]
ϵ	Characteristic energy [J]
η_f	Dynamic fluid viscosity [Pa·s]
$\eta_i\phi^2$	Weisz-Prater modulus [-]
η_i	Internal effectiveness factor [-]
η_e	External effectiveness factor [-]
Γ	Active site density [$mol\cdot m^{-2}$]
γ_s	Arrhenius number related to the surface temperature $\frac{Ea}{R\cdot T_s}$ [-]
γ_w	Arrhenius number related to the wall temperature $\frac{Ea}{R\cdot T_w}$ [-]
γ_b	Arrhenius number for bulk conditions $\frac{E_A}{RT_b}$ [-]
$\kappa_{i,j}$	Binary correlation parameter [-]
λ_f	Fluid heat conductivity [$W\cdot m^{-1}\cdot K^{-1}$]
λ_{ax}	Axial heat conductivity [$W\cdot m^{-1}\cdot K^{-1}$]
$\lambda_{bed,eff}$	Effective catalyst bed conductivity [$W\cdot m^{-1}\cdot K^{-1}$]
$\lambda_{p,eff}$	Effective thermal conductivity of the particle [$W\cdot m^{-1}\cdot K^{-1}$]
ν_i	Stoichiometry coefficient of species i [-]
ν_{ik}	Stoichiometry coefficient of component i in reaction k [-]
Ω	Collision integral [-]
Φ	Function of the species concentration [-]
ϕ	Thiele modulus $\frac{k}{a'\cdot D_{eff}}\cdot\sqrt{\frac{\alpha+1}{2}c_s^{\alpha-1}}$ [-]

ρ_f Fluid density [kg·m^{-3}]

ρ_{bed} Catalyst bed density [kg$_{cat}$·m^{-3}]

σ Collision diameter [Å]

$\tau(i,j)$ Covariance of parameter i and j [depending on variable]

τ_p Particle tortuosity [-]

θ_i Surface coverage of component i [-]

ξ Extent of reaction [mol]

ε_p Particle porosity [-]

ε_{bed} Bed porosity [-]

Latin letters

$\bar{r}$ Pore radius [m]

$\Delta H_{r,k}(T)$ Enthalpy of kth reaction at reaction temperature T [kJ·mol^{-1}]

ΔH$_r$ Enthalpy of reaction [J·mol^{-1}]

ΔH$_{\text{ads}}$ Enthalpy of adsorption [J·mol^{-1}]

ΔH$_{\text{des}}$ Enthalpy of desorption [J·mol^{-1}]

c-grad$_{ext}$ External mass transfer limitation [-]

c-grad$_{int}$ Internal mass transfer limitation [-]

Ea Activation energy [J·mol^{-1}]

G^0 Gibbs free energy [J·mol^{-1}]

R Universal gas constant [J·mol^{-1}·K^{-1}]

T-grad$_{bed}$ Heat transfer limitation inside the fixed-bed [-]

T-grad$_{ext}$ External heat transfer limitation [-]

T-grad$_{int}$ Internal heat transfer limitation [-]

A Pre-exponantial factor [depending on reaction order]

a' Particle surface to particle volume ratio $\frac{A_p}{V_p}$ [m^{-1}]

a_i Activity coefficient of species i [-]

A_p Particle surface for a diameter equivalent sphere [m^2]

b Volume fraction of inert material from bed dilution [-]

B_w Ratio of radial thermal conductivity to heat transfer at the reactor wall $\frac{1}{8} + \frac{d_p}{Bi_{h,w} \cdot d_t}$ [-]

$Bi_{h,w}$ Biot number $\frac{h_w \cdot d_p}{\lambda_{bed,eff}}$ [-]

c_i Concentration of species i [mol·m^{-3}]

c_b Bulk concentration [mol·m^{-3}]

c_{i0} Initial concentration of species i [mol·m^{-3}]

$c_{p,f}$ Fluid heat capacity at constant pressure [kJ·kg^{-1}·K^{-1}]

$c_{p,f}$ Fluid isobaric heat capacity [J·kg^{-1}·K^{-1}]

c_s Surface concentration [mol·m^{-3}]

Ca Carberry number $= \frac{c_b - c_s}{c_b}$ [-]

d_p Particle diameter [m]

d_t Tube diameter [m]

D_{1f} Diffusion coefficient of species 1 in fluid [m^2·s^{-1}]

D_{av} Average diffusion coefficient for transition region between molecular and Knudsen diffusion [m^2·s^{-1}]

D_{ax} Axial dispersion coefficient [m^2·s^{-1}]

D_{eff} Effective diffusion coefficient [m^2·s^{-1}]

D_{ij} Binary molecular diffusion coefficient of component i in j [m^2·s^{-1}]

D_{iK} Knudsen diffusion coefficient of specie i [m^2·s^{-1}]

d_{pore} Pore diameter [m]

Da_{III} Damköhler III $\frac{(-\Delta H_R) \cdot r_{v,obs} \cdot d_p}{\rho_f \cdot u_0 \cdot T_w \cdot c_{p,f}}$ [-]

Da_I Damköhler I $\frac{r_{v,obs} \cdot d_p}{u_0 \cdot c_{i0}}$ [-]

F_{i0} Molar flow rate of component i at the inlet [mol·s^{-1}]

F_i Molar flow rate of component i at the outlet [mol·s^{-1}]

h Heat transfer coefficient [W·m^{-2}·K^{-1}]

h_w Heat transfer coefficient at the wall [W·m^{-2}·K^{-1}]

J Jacobian matrix [-]

k Reaction rate constant [depending on reaction order]

k' Rate constant with respect to surface coverage [depends on reaction order]

k_B Boltzmann's constant [J·K^{-1}]

k_f Mass transfer coefficient [m·s^{-1}]

K_i Adsorption equilibrium constant for component i [bar^{-1}]

k_{ads} Pseudo rate constant for adsorption [-]

k_{des} Pseudo rate constant for desorption [-]

K_{eq} Equilibrium constant [-]

L Characteristic length [m]

L_{bed} Catalyst bed length [m]

M Molar mass [g·mol^{-1}]

$M_\tau(i,j)$ Covariance matrix [-]

M_f Molar mass of the fluid [g·mol^{-1}]

N Number of CSTR in series [-]

n Exponent in adsorption term in LHHW rate expression [-]

n_i Mole number of component i [mol]

Nu Nusselt number $\frac{h \cdot L}{\lambda_f}$ [-]

P Pressure [bar]

Pe Péclet number $\frac{L_{bed} \cdot u_0}{D_{ax}}$ [-]

Pe_m Molecular Péclet number $\frac{u_0 \cdot d_p}{D_{12}}$ [-]

Pe_p Particle Péclet number $\frac{u_0 \cdot d_p}{D_{ax}}$ [-]

Pe_h Péclet number for heat $\frac{\rho_f \cdot u_0 \cdot d_p \cdot c_{p,f}}{\lambda_{ax}}$ [-]

Pr Prandtl number $\frac{\eta_f \cdot c_{p,f}}{\lambda_f}$ [-]

R_i Inner radius of the reactor annulus [mm]

R_o Outer radius of the reactor annulus [mm]

r_0 Initial reaction rate [mol·kg^{-1}·s^{-1}]

r_{ads} Rate of adsorption [-]

r_{des} Rate of desorption [-]

$r_{v,bulk}$ Reaction rate at bulk conditions [mol·m^{-3}·s^{-1}]

$r_{V,obs}$ Reaction rate with respect bed porosity and volume fraction of inert material [mol·m^{-3}·s^{-1}]

$r_{v,obs}$ Apparent reaction rate [mol·m^{-3}·s^{-1}]

Re_p Particle Reynolds number $\frac{\rho_f \cdot u_0 \cdot d_p}{\eta_f}$ [-]

s^2 Variance [depending on variable]

Sc Schmidt number $\frac{\eta_f}{\rho_f \cdot D_{1f}}$ [-]

Sh Sherwood number $\frac{k_f \cdot L}{D_{1f}}$ [-]

T Reaction temperature [K]

T^* Dimensionless temperature [-]

T_w Wall temperature [K]

T_{av} Average temperature [K]

T_b Bulk temperature [K]

T_s Surface temperature [K]

T_x Reaction temperature in x^{th} experiment [K]

U Overall heat transfer coefficient [W·m^{-2}·K^{-1}]

u_0 Superficial velocity [m·s^{-1}]

V_p Particle volume for a diameter equivalent sphere [m^3]

W	Catalyst mass [kg]
w_i	Mass fraction of component i [-]
X	Conversion [-]
x_i	Molar fraction of component i [-]

Subscript

av	Average [-]
b	Bulk [-]
eff	Effective [-]
i	Species i [-]
j	Species j [-]
p	Particle [-]
s	Surface [-]
w	Wall [-]

List of Figures

2.1 Thermodynamic equilibrium. 4
2.2 Reaction path diagram. 5
2.3 Heterogeneous catalyzed reaction and mass transport. 7
2.4 Schematic illustration of the film layer around the particle with their corresponding temperature and concentration gradients for an exothermic and endothermic reaction, taken from [40]. 8
2.5 Experimental test of external (a) and internal (b) mass transfer limitation. Adapted from [40]. 12
2.6 Illustration of a differential reactor with low consumption of species i. 16
2.7 Sketch of an ethylene oxide molecule. 17
2.8 Triangular reaction scheme of partial ant total oxidation of ethylene and consecutive oxidation of ethylene oxide. 19
2.9 Influence of subsurface oxygen. 20
2.10 Influence of subsurface chlorine. 21
2.11 Sketch of oxametallacycle. 22

3.1 Flow diagram of the kinetic test setup. 29
3.2 Sketch of the differentially operated isothermal fixed-bed reactor inside a heated fluidized sand bath. 30
3.3 Sketch of the gas module designed for the gas supply. 31
3.4 Sketch of the water module supply design to supply liquid water to the evaporator. 32
3.5 Sketch of the water evaporator design to supply vapor feed to the reactor. 32
3.6 Sketch of the kinetic test setup with the fluidized sand-bath, gas feed modules, GC and electronics housing. 33
3.7 Flow diagram of the Pilot Scale Profile Reactor (PSPR) setup. 35
3.8 Sketch of the gas feed supply module design. 36
3.9 Sketch of the PSPR with arranged capillaries to measure spatial species profiles. 38
3.10 Schematic drawing of the combustion unit. 39
3.11 Pilot Scale Profile Reactor setup designed (top) and build (bottom). . 40

4.1 Compact Profile Reactor (CPR) used to investigate the reaction network of ethylene oxide synthesis on a Ag-catalyst and the mechanism of chlorine inhibition. a) Working principle. b) Annotated photograph of the open reactor. 44

4.2 GC switching valves and columns arrangement to analyze the gas sample composition for the profile measurements. 46

4.3 Pilot Scale Profile Reactor (PSPR) for spatially resolved temperature measurements and species sampling. Temperature measurement points (16) are indicated in red, the species sampling points (10) in black. . . 48

5.1 Reaction rate for selective (r_{EO}) and unselective oxidation (r_{CO_2}) vs. C_2H_4 partial pressure at 225 °C and 17 bara with 1.25 ppm DCE. . . 52

5.2 Reaction rate for selective (r_{EO}) and unselective oxidation (r_{CO_2}) vs. O_2 partial pressure at 225 °C and 17 bara with 1.25 ppm DCE. 52

5.3 Reaction rate for selective (r_{EO}) and unselective oxidation (r_{CO_2}) vs. CO_2 partial pressure at 225 °C and 17 bara with 1.25 ppm DCE. . . . 53

5.4 Reaction rate for selective (r_{EO}) and unselective oxidation (r_{CO_2}) vs. H_2O partial pressure at 225 °C and 17 bara with 1.25 ppm DCE. . . . 53

5.5 Reaction rate for selective (r_{EO}) and unselective oxidation (r_{CO_2}) vs. $C_2H_4Cl_2$ partial pressure at 225 °C and 17 bara. 54

5.6 Arrhenius plot for initial reaction rates measured at GHSV = 66,000 h^{-1}, 17 bara pressure, and DCE concentration of 1.25 ppm under differential conditions. 55

5.7 Arrhenius plot for initial reaction rates measured at GHSV = 66,000 h^{-1}, 17 bara pressure, and DCE concentration of 2.5 ppm under differential conditions. 55

5.8 Molar flow rate and temperature profiles measured in the CPR at GHSV = 4750 h^{-1}, 225 °C heating block temperature, 17 bara pressure, and 1.25 ppm DCE concentration in the feed. (a) educt profiles and temperature, (b) product profiles, (c) conversion of oxygen and ethylene and selectivities to EO and CO_2. 63

5.9 a) SEM picture of the Ag/Al_2O_3 catalyst. b) EDX spectrum of main components. c) EDX spectrum at the noise level. d) Species profiles and chlorine signal heights. 65

5.10 CPR profiles at GHSV = 9500 h^{-1}, 225 °C heating block temperature, 17 bara pressure, and 1.25 ppm DCE concentration in the feed. (a) educt profiles and temperature, (b) product profiles, (c) conversion of oxygen and ethylene and selectivities to EO and CO_2. 67

5.11 CPR profiles at GHSV = 9500 h^{-1}, 225 °C heating block temperature, 17 bara pressure, and 2.50 ppm DCE concentration in the feed. (a) educt profiles and temperature, (b) product profiles, (c) conversion of oxygen and ethylene and selectivities to EO and CO_2. 70

5.12 CPR profiles at GHSV = 4750 h^{-1}, 225 °C heating block temperature, and 17 bara pressure without DCE cofeeding. Profile measurement from outlet to inlet. (a) educt profiles and temperature, (b) product profiles, (c) conversion of oxygen and ethylene and selectivities to EO and CO_2. 72

5.13 CPR profiles at GHSV = 4750 h^{-1}, 225 °C heating block temperature, and 17 bara pressure without DCE cofeeding. Profile measurement from inlet to outlet. (a) educt profiles and temperature, (b) product profiles, (c) conversion of oxygen and ethylene and selectivities to EO and CO_2. 75

5.14 CPR profiles fitted at GHSV = 4750 h^{-1}, 200 °C heating block temperature, 17 bara pressure and 1.25 ppm DCE concentration in the feed. (a) educt profiles, (b) product profiles. The lines represent the resulting fitting, the discrete points represent measurements. 78
5.15 CPR profiles fitted at GHSV = 4750 h^{-1}, 210 °C heating block temperature, 17 bara pressure and 1.25 ppm DCE concentration in the feed. (a) educt profiles, (b) product profiles. The lines represent the resulting fitting, the discrete points represent measurements. 79
5.16 CPR profiles fitted at GHSV = 4750 h^{-1}, 225 °C heating block temperature, 17 bara pressure and 1.25 ppm DCE concentration in the feed. (a) educt profiles, (b) product profiles. The lines represent the resulting fitting, the discrete points represent measurements. 80
5.17 Pilot reactor profiles at GHSV = 4750 h^{-1}, 194 °C temperature of the heat-transfer fluid, 17 bara pressure, and 1.53 ppm DCE concentration in the feed. Discrete points were measured; the compact lines show simulation results by applying the measured kinetic parameters. Reactants and temperature (a), products (b) and conversion and selectivity (c). . 84
5.18 Pilot reactor profiles at GHSV = 4750 h^{-1}, 194 °C temperature of the heat-transfer fluid, 17 bara pressure, and 3.18 ppm DCE concentration in the feed. Discrete points were measured; the compact lines show simulation results by applying the measured kinetic parameters. Reactants and temperature (a), products (b) and conversion and selectivity (c). . 86

A.1 GC Calibration for molar flow of C_2H_4 to N_2 adjusted to measured area ratio $A_{C_2H_4}/A_{N_2}$. 90
A.2 GC Calibration for molar flow of O_2 to N_2 adjusted to measured area ratio A_{O_2}/A_{N_2}. 91
A.3 GC Calibration for molar flow of CO_2 to N_2 adjusted to measured area ratio A_{CO_2}/A_{N_2}. 91
A.4 GC Calibration for molar flow of H_2O to N_2 adjusted to measured area ratio A_{H_2O}/A_{N_2}. 92
A.5 GC Calibration for molar flow of EO to N_2 adjusted to measured area ratio A_{EO}/A_{N_2}. 92
A.6 GC Calibration for molar flow of 1,2-dichloroethane to N_2 adjusted to measured area ratio A_{DCE}/A_{N_2}. 93
A.7 GC Calibration for molar flow of vinyl chloride to N_2 adjusted to measured area ratio A_{VC}/A_{N_2}. 93
A.8 GC Calibration for molar flow of ethyl chloride to N_2 adjusted to measured area ratio A_{EC}/A_{N_2}. 94
A.9 Profiles measured in the Pilot Scale Profile Reactor at 180 °C, 17 bara at GHSV = 4750 h^{-1} and 1.5 ppm DCE. 100
A.10 Profiles measured in the Pilot Scale Profile Reactor at 180 °C, 17 bara at GHSV = 4750 h^{-1} and 0 ppm DCE. 101
A.11 Profiles measured in the Pilot Scale Profile Reactor at 180 °C, 17 bara at GHSV = 4750 h^{-1} and 0.75 ppm DCE. 103
A.12 Profiles measured in the Pilot Scale Profile Reactor at 190 °C, 17 bara at GHSV = 4750 h^{-1} and 1.5 ppm DCE. 105
A.13 Profiles measured in the Pilot Scale Profile Reactor at 190 °C, 17 bara at GHSV = 4750 h^{-1} and 1.5 ppm DCE without CO_2 cofeeding. . . . 106

A.14 Profiles measured in the Pilot Scale Profile Reactor at 200 °C, 17 bara at GHSV = 4750 h^{-1} and 3.18 ppm DCE. 108

List of Tables

2.1 Appropriate Dimensionless Numbers for Gases in Laboratory Reactors. Adapted from [40]. 10
2.2 Operating Parameters Used in the Air and Oxygen Based Ethylene Oxide Production [10]. 18
2.3 Boundary Conditions Applied to the Two Dimensional Reactor Model. 27

4.1 Operating Parameters Used for the Kinetic Measurements. 42
4.2 Standard Species Concentrations for the investigation of the epoxidation reaction. 43
4.3 Operating Parameters Used for the Profile Measurements with the CPR. 45
4.4 Conditions for Spatial Profile Measurements. 47

5.1 Parameter for External Limitation Criteria. 50
5.2 Parameter for Internal Limitation Criteria. 50
5.3 Parameter for the Catalyst Bed Limitation Criteria. 51
5.4 Experimentally Determined Apparent Activation Energies for the Epoxidation and Total Combustion Reaction. 56
5.5 Parameter for External Limitation Criteria Applied for the CPR Measurements. 60
5.6 Parameter for the Catalyst Bed Limitation Criteria Applied for the CPR Measurements. 61
5.7 Parameters for Diagnostic Evaluation of the Presence of Axial Dispersion. 76
5.8 Kinetic Parameter Determined by Regression of Profiles Measured in the CPR Using the Levenberg-Marquardt Solver Algorithm in ComSol 5.5^{TM}. 81
5.9 Parameters for Diagnostic Evaluation of the Presence of Radial Dispersion. 82

A.1 Correlation of the Kinetic Parameters Determined by Regression of Profiles Measured in the CPR Using the Levenberg-Marquardt Solver Algorithm in ComSol 5.5^{TM} (Part 1). 95
A.2 Correlation of the Kinetic Parameters Determined by Regression of Profiles Measured in the CPR Using the Levenberg-Marquardt Solver Algorithm in ComSol 5.5^{TM} (Part 2). 96
A.3 Correlation of the Kinetic Parameters Determined by Regression of Profiles Measured in the CPR Using the Levenberg-Marquardt Solver Algorithm in ComSol 5.5^{TM} (Part 3). 97